



Development and Application of Laser Methods for Electronic Spectroscopy of Radicals

INAUGURALDISSERTATION

zur

Erlangung der Würde eines Doktors der Philosophie

vorgelegt der

Philosophisch-Naturwissenschaftlichen Fakultät

der Universität Basel

von

Richa Chauhan

aus Indien

Basel, March 2010

Original document stored on the publication server of the University of Basel: edoc.unibas.ch This work is licenced under the agreement "Attribution Non-Commercial No



Derivatives 2.5 Switzerland". The complete text may be viewed here: creativecommons.org/licenses/by-nc-nd/2.5/ch/deed.en

Genehmigt von der Philosophisch-Naturwissenschaftlichen Fakultät auf
Antrag von:

Prof. Dr. John. P. Maier (Faculty responsible)

Prof. Dr. Stefan Willitsch (Co-referee)

Basel, den February 17, 2009

Prof. Dr. Eberhard Parlow
Dekan



Attribution-Noncommercial-No Derivative Works 2.5 Switzerland

You are free:



to Share — to copy, distribute and transmit the work

Under the following conditions:



Attribution. You must attribute the work in the manner specified by the author or licensor (but not in any way that suggests that they endorse you or your use of the work).



Noncommercial. You may not use this work for commercial purposes.



No Derivative Works. You may not alter, transform, or build upon this work.

- For any reuse or distribution, you must make clear to others the license terms of this work. The best way to do this is with a link to this web page.
- Any of the above conditions can be waived if you get permission from the copyright holder.
- Nothing in this license impairs or restricts the author's moral rights.

Your fair dealing and other rights are in no way affected by the above.

This is a human-readable summary of the Legal Code (the full license) available in German:
<http://creativecommons.org/licenses/by-nc-nd/2.5/ch/legalcode.de>

Disclaimer:

The Commons Deed is not a license. It is simply a handy reference for understanding the Legal Code (the full license) — it is a human-readable expression of some of its key terms. Think of it as the user-friendly interface to the Legal Code beneath. This Deed itself has no legal value, and its contents do not appear in the actual license. Creative Commons is not a law firm and does not provide legal services. Distributing of, displaying of, or linking to this Commons Deed does not create an attorney-client relationship.

Dedicated to my parents

Acknowledgements

In the course of reaching the completion of this thesis, I have been accompanied and supported by many people. I acknowledge debt to those who have helped along the way.

First of all, I would like to express my sincere gratitude to Prof. John P. Maier, who gave me the opportunity to work in his group. He provided me with helpful suggestions, important advices and constant motivation in the course of my PhD. I am thankful to Prof. Stefan Willitsch, also, who kindly agreed to be co-referee of my thesis. My cordial thanks to Prof. Martin Jungen, who generously accepted to act as the chairman of my defence.

I am grateful to Prof. F. Merkt and his group member Dr. Thomas A. Paul from ETH Zurich, who shared valuable tricks to build the Pulsed Amplification System in our lab. I also wish to express my sincere thanks to Dr. Mitsunori Araki, who gave many fruitful suggestions and directions, in the first two years of my PhD. Special thanks are due to Dr. Petre Birza and Dr. Dmitriy Khoroshev who guided me in the first year. They had been very cooperating all through.

My cordial appreciation to Dr. Eunsook Kim for her valuable instructions and suggestions. The analyses of the results had not been possible without her help. In addition, it was a great experience, working with her.

Special gratitude goes to Dr. Fabio Mazzotti, who has been always there, ready to help

with all his patience, guide and motivate in the research. I learnt a lot while working with him over the last two years. Sincere thanks are extended to Dr. Marek Tulej, who devoted his precious time and guided us to improve the functioning of the setup. Discussing with him rejuvenates a person and brings the enthusiasm at work.

My keen appreciation goes to Dr. Tomasz Motylewski, for his contribution to the software part of the system. He helped, from time to time, improving the softwares and fix all the related problems. I am thankful to Dr. David Pfluger, also, for his occasional help in the alignment of the laser.

I am grateful to all of the members of my group, for their cooperation and inducing a friendly environment. I wish new members, specially Ranjini Raghunandan from CRD-lab, all the best in their endeavours.

My sincere appreciation to Mr. Dieter Wild and Mr. Grischa Martin from the mechanical workshop for their specialised skills in the construction of topnotch devices; to Mr. Georg Holderied for his help on all the electronic and electrical units. I am indebted to Mr. Jacques Lecoultre for synthesizing important chemical samples, used in the experiments. I also thank our secretaries Ms. Esther Stalder and Ms. Daniela Tischauser for taking care of all the bureaucratic matters. The Swiss National Foundation and the University of Basel are thanked for the financial support.

I would like to express my heartiest thanks to Dr. Corey Rice, Dr. Divya Vats, Dr. Mayank P. Agnihotri, Dr. Navratna Vajpai, Dr. Ratnesh Thapliyal and specially, to Dr. Fabio Mazzotti, for correcting my thesis, grammatically and scientifically.

I am grateful to some more people, whom I met here, in Basel, who gradually became my close friends and are now dearest to me. To name a few, Anurag-Divya, Arundhati, Ashwini-Joshiji, Jenish-Jhanvi, Kola, Murali-Reshmidi, Nidhi-Vivek, Rejina-Sudip and Vajpai. Their company has been very relaxing, entertaining and motivating.

In last but not the least, I would like to express special thanks to my husband, Ratnesh Thapliyal, who supported me during all phases of my PhD. He has been a constant source of encouragement and inspiration to me.

Contents

1	Introduction	1
1.1	Spectroscopy	1
1.1.1	The intrusion of spectroscopy in other fields	1
1.1.2	Types of spectroscopy	3
1.1.3	Advantages	6
1.1.4	Electronic spectroscopy and the resolution	7
1.1.5	Goal of the thesis	8
	Bibliography	9
2	Electronic spectrum of the hydrocarbon cation $CCCCH_3^+$	13
2.1	Cavity ring down spectroscopy	13
2.1.1	Overview	13
2.1.2	Principle	18
2.1.3	Cavity modes	19
2.2	Experimental scheme	21
2.2.1	Frequency doubler	24
2.2.2	Source of radicals	26
2.2.3	Advantages	27

2.2.4	Shortcomings	29
2.3	Abstract	30
2.4	Results and discussion	30
2.5	Conclusion	35
	Bibliography	36
3	Pulsed amplification system	41
3.1	Principle	41
3.1.1	Gain medium and the energy levels structure	42
3.1.2	Amplification	48
3.1.3	Overview of the setup	50
3.1.4	Advantages	51
3.1.5	Limitations	51
3.2	Setup description	54
3.2.1	Measurements	61
3.2.2	Measures to remove ASE	62
3.3	Results	62
3.4	The Frequency doubling	63
3.4.1	Frequency upconversion	63
3.4.2	Doubling crystals	64
3.4.3	Setup	66
3.4.4	The bandwidth	67
3.5	Cavity ring down	67
3.5.1	Result	73
3.5.2	Calculation of the bandwidth of the laser beam.	74
3.5.3	Outlook	75
	Bibliography	77
4	Molecules studied by four wave mixing spectroscopy	81
4.1	Theory of degenerate and two-color variants of the method	81
4.1.1	Overview	81

Contents

4.1.2	Degenerate four wave mixing	84
4.1.3	Two-color resonant four-wave mixing	86
4.2	Observation of N_2^+ and C_2	89
4.2.1	Introduction	89
4.2.2	Experimental	94
4.2.3	Results and discusson	95
4.2.4	Conclusion	98
4.3	Detection of HC_2S	99
4.3.1	Introduction	99
4.3.2	Experimental setup	100
4.3.3	Results and discussion	102
4.3.4	Conclusion	105
	Bibliography	107
5	Laser Ablation	111
5.1	Introduction	111
5.2	Experimental set up	115
5.2.1	Ablation source	115
5.2.2	Probe	116
5.3	Results and discussion	117
	Bibliography	121
6	Appendix	123
6.1	Electronic spectrum of the hydrocarbon cation $CCCCH_3^+$	123
6.1.1	Parallel and perpendicular structures in electronic transition of poly- atomic molecules	123
6.1.2	General features of molecular rotation	125
6.1.3	Rotational energy levels	128
6.1.4	Transition types	131
6.1.5	Sub-bands of parallel bands: prolate top molecule	132
6.1.6	Conclusion	133

6.2 Pulsed amplification system	134
7 Curriculum vitae	135
7.1 Personal information	135
7.2 Education	135

1.1 Spectroscopy

Spectroscopy is the measure of the interaction of photons with matter as a function of their energy. Figure 1.1 gives an example to show one of the many ways the photon can interact. The phenomenon is called the photoelectric effect, where a beam of light shines on a metal surface and causes the ejection of electrons from the metal. The kinetic energy, E , of the electrons (photoelectrons) can be measured by the equation,

$$E = h\nu - \phi \quad (1.1)$$

where $h\nu$ is the energy of the photon of frequency ν and ϕ is the work function of the metal. In conditions where the probe particle is not a photon, spectroscopy refers to the measurement of the interaction of particles or material as a function of the probe particle energy. Molecular spectra are observed, when a molecule undergoes absorption or emission of the electromagnetic radiation with a resulting increase or decrease in energy of the molecule, respectively. Figure 1.2 gives an example of two types of (line) spectra.

1.1.1 The intrusion of spectroscopy in other fields

The significance of a process is judged on the basis of its versatility and applicability in different fields. The spectroscopic analysis has been crucial in the development of the most fundamental theories in physics, including quantum mechanics, the special and general

Photoelectric Effect

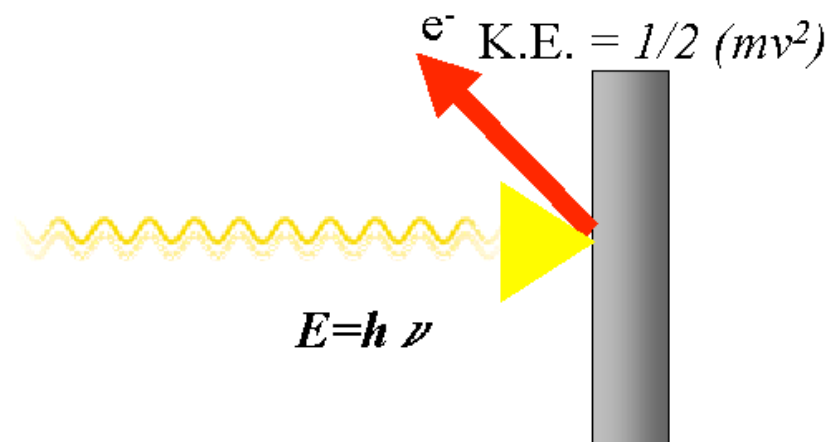


Figure 1.1: The photoelectric effect.

theories of relativity, and quantum electrodynamics [1]. Spectroscopy, as applied to high-energy collisions, has been a key tool in developing scientific understanding not only of the electromagnetic force but also of the strong and weak nuclear forces [2]. Spectroscopic techniques have been applied in virtually all technical fields of science and technology. Millimeter and sub-millimeter-wave spectroscopy of nuclei in a magnetic field has been employed in a medical technique called magnetic resonance imaging to visualize the internal soft tissue of the body with unprecedented resolution. Microwave spectroscopy was used to discover the so-called three-degree blackbody radiation, the remnant of the big bang (i.e., the primeval explosion) from which the universe is thought to have originated. The internal structure of the proton, neutron and the state of the early universe up to the first thousandth of a second of its existence is being unraveled with spectroscopic techniques utilizing high-energy particle accelerators. The constituents of distant stars, intergalactic molecules, and even the primordial abundance of the elements before the

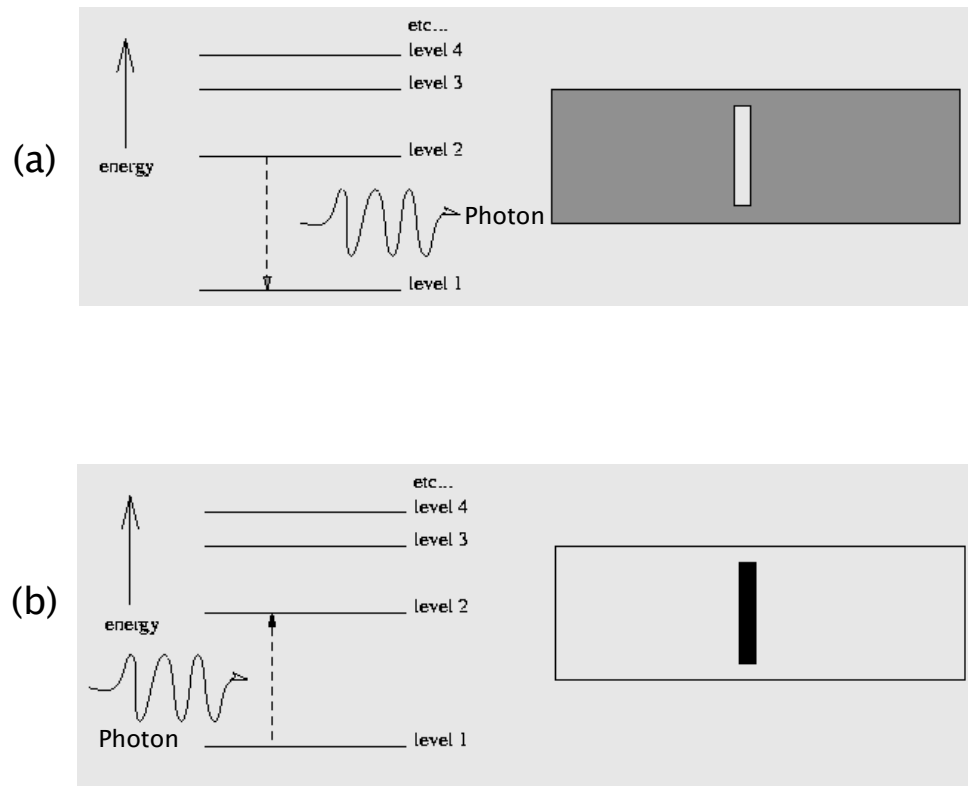


Figure 1.2: (a) An excited hydrogen atom relaxes from level 2 to level 1, yielding a photon. This results in a bright emission line. (b) A hydrogen atom in the ground state is excited by a photon of exactly the 'right' energy needed to send it to level 2, absorbing the photon in the process. This results in a dark absorption line.

formation of the first stars can be determined by optical, radio, and X-ray spectroscopy [3]. Figure 1.3 shows spectra of some stars. Optical spectroscopy is used routinely to identify the chemical composition of matter and to determine its physical structure. Figure 1.4 shows spectra of some commonly used light sources.

1.1.2 Types of spectroscopy

In a broader sense, the spectroscopy can be categorized on the basis of the physical quantity measured, which is normally intensity either of the energy absorbed or produced.

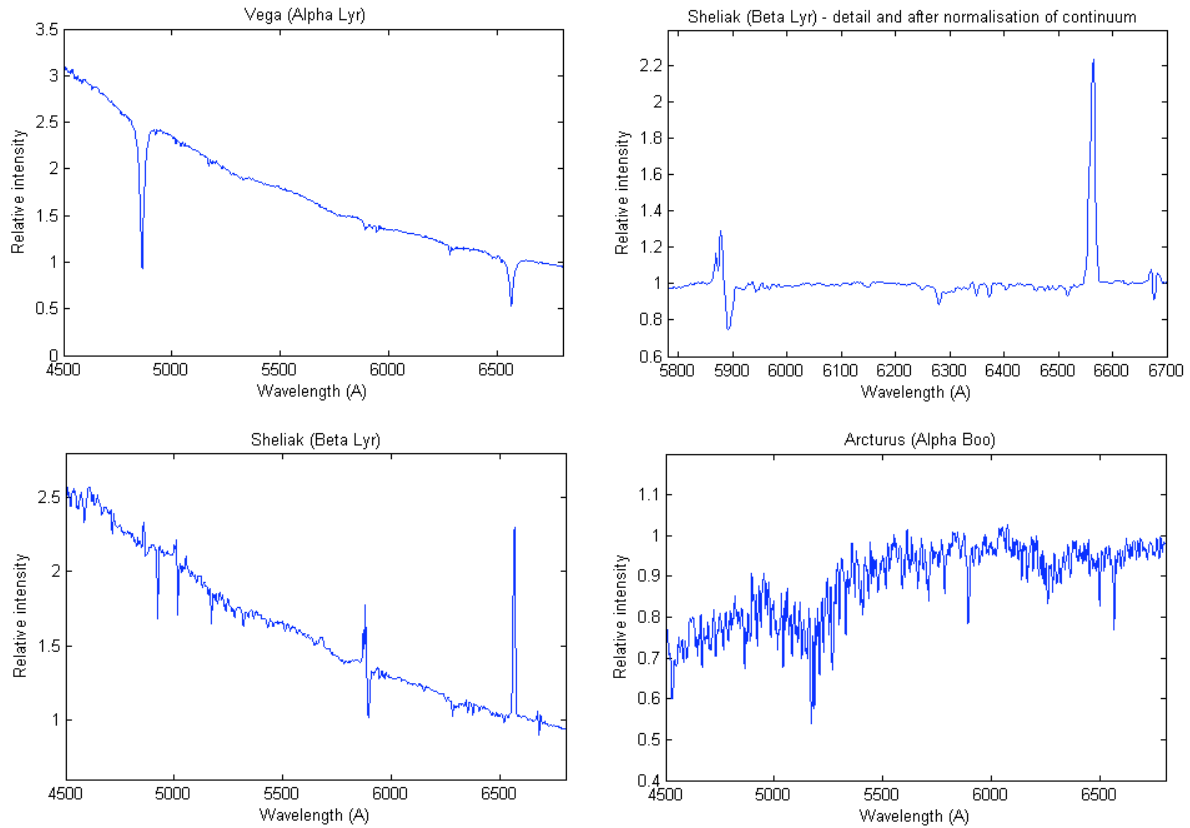


Figure 1.3: *Some stellar spectra observed.*

One example is called as optical spectroscopy. There are different kinds of optical spectroscopy depending on the type of transition induced by the absorption of the photon(s) and therefore, on the specific region of the electromagnetic (EM) spectrum (Figure 1.5). Table 1.1 and Figure 1.6 gives a summary of the classification. The optical spectroscopy can be divided into

- Rotational Spectroscopy

One studies the absorption and emission of the EM radiation (typically in the microwave region of the electromagnetic spectrum) by molecules associated with a corresponding change in the rotational quantum number of the molecule [4, 5].

- Vibrational Spectroscopy

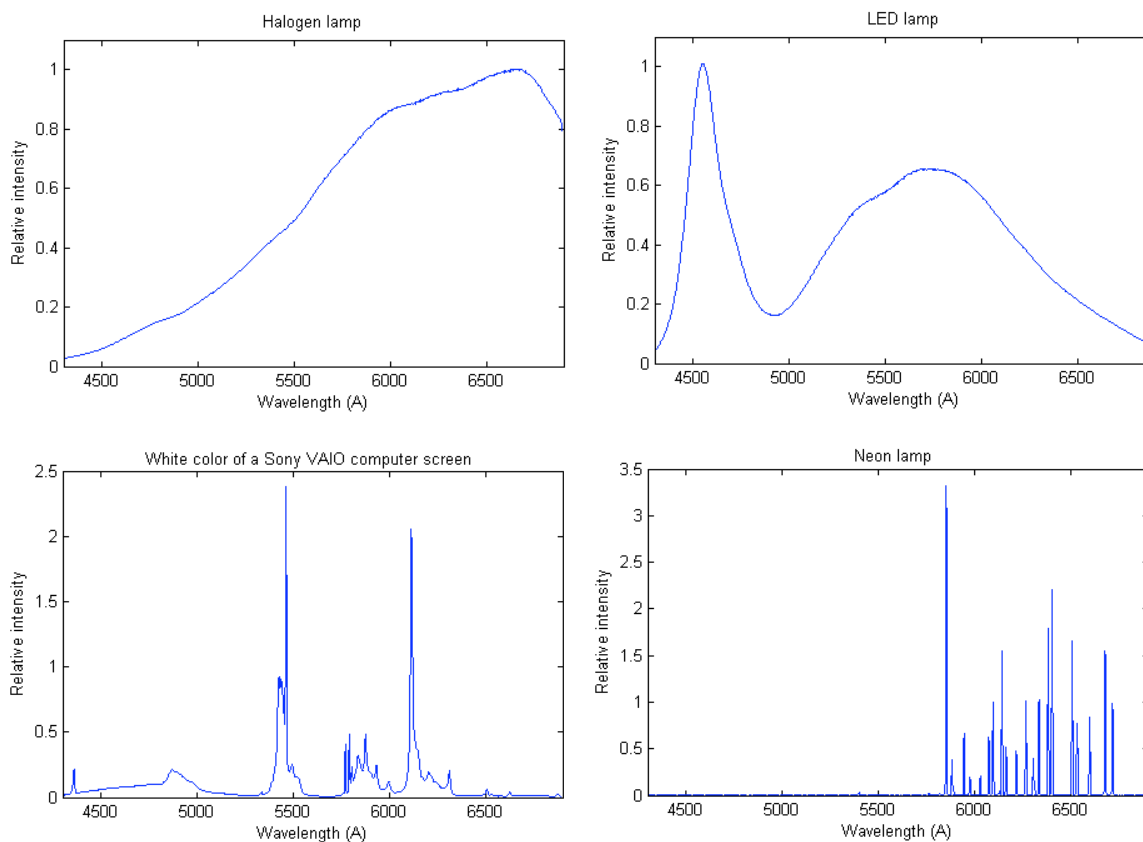


Figure 1.4: *Some spectra of artificial sources.*

The infrared radiation absorption leaves the molecule in a vibrationally excited state. It can, then, dissipate its energy to a vibrational mode non-radiatively, or emit a photon.

- **Electronic Spectroscopy**

Electronic spectroscopy probes directly the quantization of the electronic energy. The transitions, in absorption or emission, between different electronic states of an atom or molecule are studied. In other words, the charge distribution of electrons around a molecule is changed by the light absorption. The light in this region has a

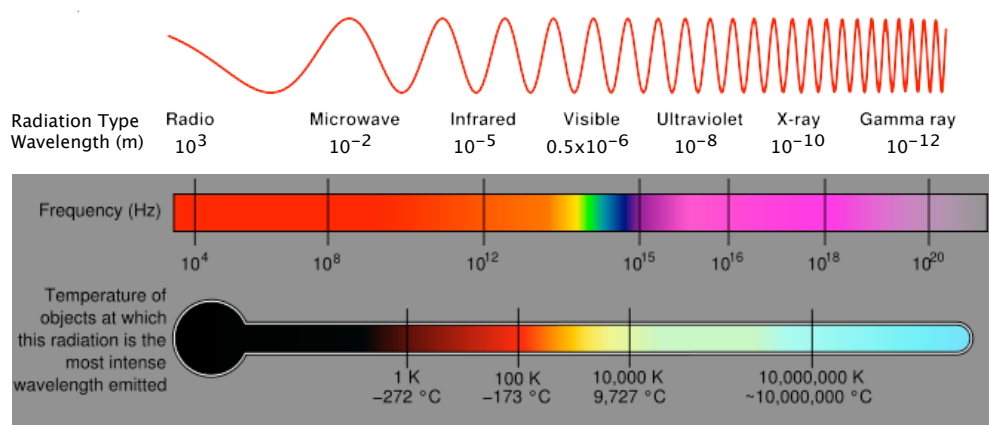


Figure 1.5: *Electromagnetic spectrum*

Table 1.1: *Types of Spectroscopy: in terms of energy levels.*

Spectroscopy	Radiation	Wavenumbers	Transition
Electronic	UV/Vis	10^4 - 10^5 cm^{-1}	Electronic (+ vibration + rotation)
Rotational-Vibrational	Infrared	10^2 - 10^3 cm^{-1}	Vibration (+ rotation)
Pure Rotational	Far Infrared/Microwave	10^{-1} - 10^1 cm^{-1}	Rotation

lot of energy and often can break bonds.

1.1.3 Advantages

Spectroscopic techniques are extremely sensitive. Single atoms and even different ¹isotopes of the same atom can be detected among 10^{20} or more atoms of a different species. Trace amounts of pollutants or contaminants are often detected most effectively by spectroscopic techniques. Certain types of microwave, optical, and gamma-ray spectroscopy are capable of measuring infinitesimal frequency shifts in narrow spectroscopic lines. Fre-

¹Isotopes are all atoms of an element that have unequal mass but the same atomic number. Isotopes of the same element are virtually identical chemically.

quency shifts as small as one part in 10^{15} of the frequency being measured can be observed with ultrahigh resolution laser techniques, eventually frequency measurements are the most accurate physical measurements.

Spectroscopy is used as a tool for studying the structures of atoms and molecules. The large number of wavelengths emitted by these systems makes it possible to investigate their structures in detail, including the electron configurations of ground and various excited states. Spectroscopy also provides a precise analytical method for finding the constituents in material having unknown chemical composition. A concentration of a few parts per million of a trace element in a material can be detected through its emission spectrum. Therefore, spectral analysis of the lines obtained from extraterrestrial environment allows the identification of the species present and the characterization of the conditions prevailing there.

1.1.4 Electronic spectroscopy and the resolution

Figure 1.6: *Schematic depiction of the superposition of electronic, vibrational and rotational energy levels. The absorption spectrum of a molecule is determined by all non forbidden transitions between pairs of levels in the right hand column.*

A spectrum obtained can be termed as low or high resolution, depending on how well the spectral features are resolved. One refers usually to the performance of the system used to obtain the spectra, when speaking of low or high resolution spectroscopy. Generally, the former is used for analytical purposes. On the other hand, the latter provides more and more accurate structural information of the molecules under study, which in turn gives impetus for theory to account for it. The general appearance of the two systems is usually different. The design of a low resolution instrument is oriented towards compactness, convenience and ease of use, whereas the other type in many cases are bulky, of limited wavelength range, inconvenient and slow to use. High-resolution spectroscopy is nowadays capable of providing detailed information on the properties of electronically excited states than merely vertical transition energies. The analysis of high resolution

spectra involves fine, hyperfine, spin-rotation and parity-violation interactions.

1.1.5 Goal of the thesis

In the past few decades, progress has been made in the electronic spectroscopy of unsaturated carbon-chain radicals both in neon matrices and gas phase [6]. Highly-unsaturated carbon chains have been of interest as reactive intermediates in interstellar hydrocarbon chemistry [7], combustion [8], and discharge processes [9]. High-resolution experimental techniques such as cavity ring-down (CRD) spectroscopy [10, 11] allow the detection of rotationally resolved electronic absorption spectra of hydrocarbon radicals. By using a single-mode cw laser combined with a pulsed slit nozzle discharge, such high resolution electronic transitions of linear and nonlinear carbon chains have been measured [12]. This method led to the finding of a hydrocarbon cation CCCCH_3^+ , accidentally. The second chapter reports on the rotationally resolved spectrum of the cation thus obtained and its analysis.

There are the two essential elements of gas phase electronic spectroscopy,

- A probe beam.

Continuous wave (cw) lasers or Fourier-Transform (FT)-limited pulsed lasers provide narrow bandwidth laser beam. The cw lasers operating in single mode have the narrowest possible bandwidths (as low as 500 kHz) by virtue of the energy-time uncertainty. Laser sources in the infrared to vacuum ultraviolet range have found many applications in atomic and molecular physics and physical chemistry. The near and far UV region is of special interest for the detection of electronic transitions of various radicals. Moreover, it is always desirable to have a single laser spanning a long wavelength range than switching to different lasers for different wavelength regions. A cw laser in Ti:Sapphire configuration has a limited operating range from mid visible to IR region of the spectrum. This demands the application of non-linear optical processes such as sum- and difference- frequency mixing and second-harmonic generation for frequency extension. Such processes need higher peak power than provided by cw lasers. In addition, high resolution spectroscopy

is only possible with narrow-bandwidth lasers. The best bet, which meets the opposing requirements is a ²FT-limited pulse with high peak power. This motivated to build a near FT-limited pulsed amplification system with a cw ring laser. The third chapter gives a description of this work.

- Source of the radicals/molecules to be studied

Discharge plasmas and laser ablation are commonly used to produce transient species. These are then probed by the laser to obtain the spectrum. The fourth chapter illustrates the building and demonstration of a laser ablation source which was accomplished with the aim of producing clusters.

There are different methods employed to carry out the gas phase electronic spectroscopy, each with their own specific advantages and disadvantages. Four wave mixing (FWM) and CRD are two such methods. The fifth chapter presents the observation of a cation, first time in the history by FWM. It, then, describes the versatility of the technique proved by the study of ground state vibrations of HC₂S radical.

²The coherence time of FT-limited pulses is not shorter than its duration.

Bibliography

- [1] R. Rompe and H. J. Treder, *Found. of Phys.*, 1983, **13**, 347.
- [2] C. Degen, Q. Lin, and B. H. Meier, *Phys. Rev. Lett.*, 2006, **96**, 137604.
- [3] F. Salama, *J. Mol. Struct.*, 2001, **28**, 19.
- [4] H. Kroto, *Molecular Rotation Spectra*, Dover Phoenix, 2003.
- [5] Townes and Schawlow, *Microwave Spectroscopy*, Dover Publications, 1975.
- [6] J. P. Maier, *J. Phys. Chem. A*, 1998, **102**, 3462.
- [7] T. Henning and F. Salama, *Science*, 1998, **282**, 2204.
- [8] H. Richter and J. B. Howard, *Prog. Energy Comb. Sci.*, 2000, **26**, 565.
- [9] T. Fujii and M. Kareev, *J. Apl. Phys.*, 2001, **89**, 2543.
- [10] A. O'Keefe and D. A. G. Deacon, *Rev. Sci. Instrum.*, 1988, **59**, 2544.
- [11] G. Berden, R. Peeters, and G. Meijer, *Int. Rev. Phys. Chem.*, 2000, **19**, 567.
- [12] P. Birza, T. Motylewski., D. Khoroshev, A. Chirokolava, H. Linnartz, and J. P. Maier, *Chem. Phys.*, 2002, **283**, 119.

Chapter 2

Electronic spectrum of the hydrocarbon cation $CCCCH_3^+$

2.1 Cavity ring down spectroscopy

2.1.1 Overview

Direct absorption spectroscopy of atoms/molecules/radicals in the gas phase is a very powerful tool in analytical chemistry, physical chemistry and in more general research fields. It yields both quantitative absolute concentrations as well as absolute frequency-dependent cross-sections. In a 'conventional' absorption experiment, the amount of light which is transmitted through a sample is measured (Figure 2.1). This kind of direct ab-

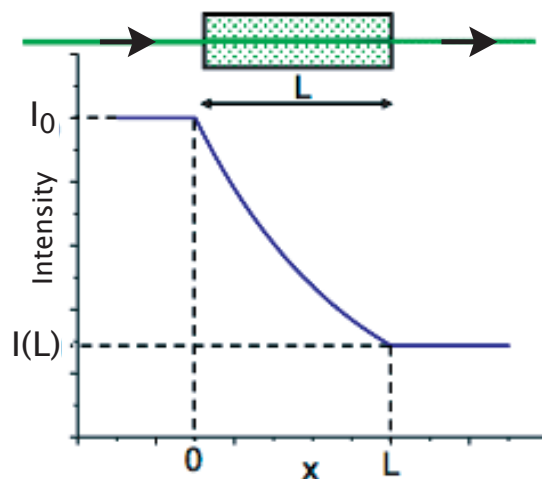


Figure 2.1: Conventional direct absorption measurement.

sorption has a limited sensitivity as a small attenuation is measured on top of a large background. High sensitivity can be obtained by modulation schemes and/or by increasing the absorption path length. Figure 2.2 illustrates the principles of some of these schemes. Alternatively, the detection of phenomena which are induced by the absorption of light can be used as the parameter to study the molecules. Some examples are pressure changes in photoacoustic spectroscopy, fluorescence in laser-induced fluorescence (LIF, Figure 2.3), and ions in resonance enhanced multiphoton ionization (REMPI). The great advantage of these techniques is that they are background free. The disadvantage of these techniques is that these are not self-calibrating. Cavity ring down spectroscopy (CRDS) is among others a sensitive absorption technique. The work reported in [1], [2] and [?] pioneered the technique. Herbelin et al. first proposed the use of an optical cavity for measuring the reflectance of mirror coatings (Figure 2.4). Anderson et al. demonstrated a better way to measure the reflectance by a different approach of sending the continuous wave (cw) light beam to the optical cavity. In both techniques, coupling of light into the cavity was accomplished by accidental coincidences of the frequency of a narrow bandwidth laser with one of the cavity modes. In 1988, O'Keefe and Deacon showed that

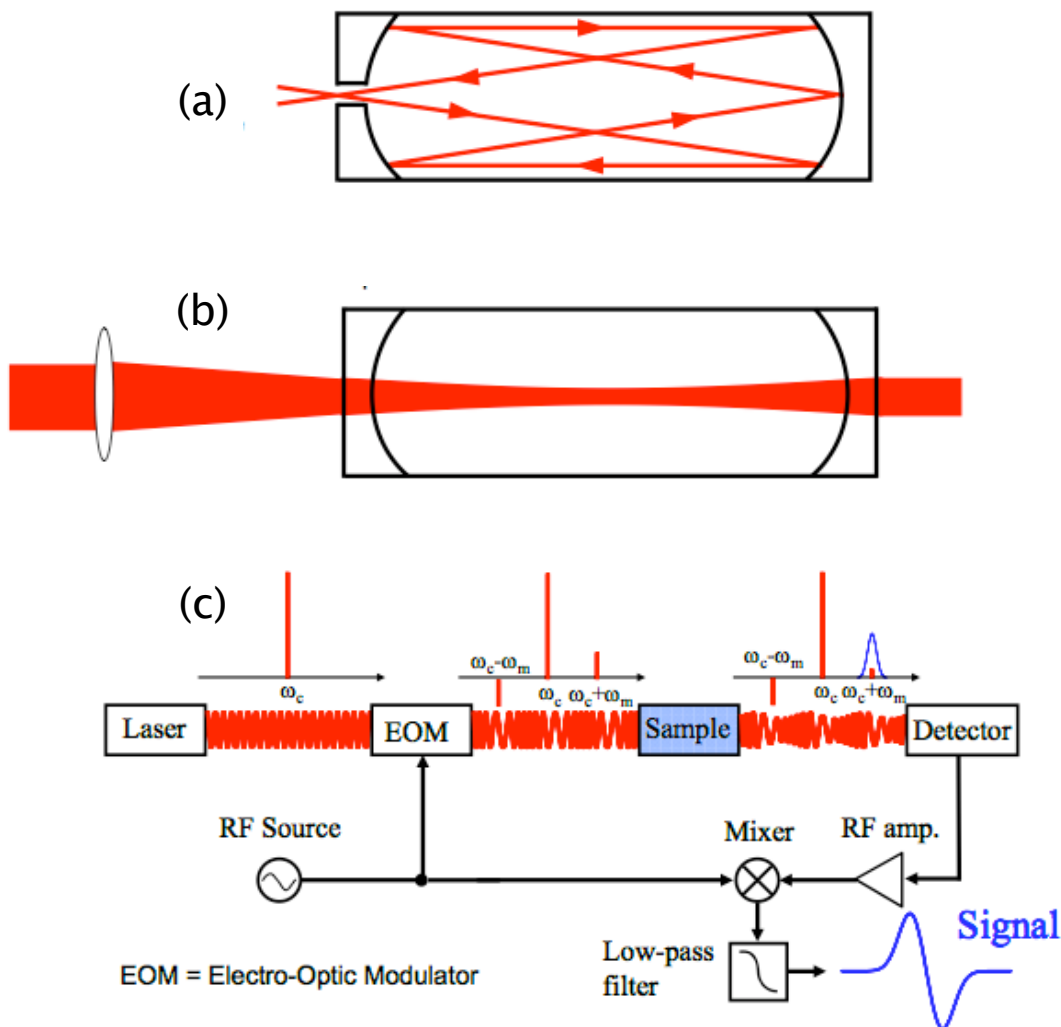
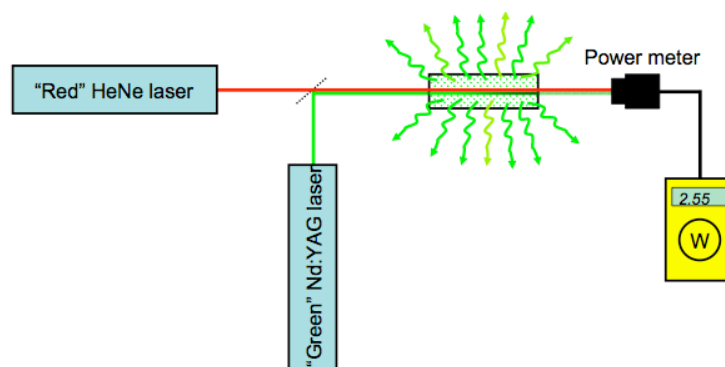


Figure 2.2: Higher sensitivity schemes: (a) Multi-pass cell : large optical length; (b) Cavity-enhancement : larger optical length, high intracavity power, laser frequency stabilization; (c) Typical setup for frequency-modulation spectroscopy.

problems associated with mode matching could be circumvented by using a pulsed laser. Additionally, owing to the pulsed character, no extra units were required for switching off the laser, before observing the decay transient. They demonstrated the sensitivity by recording the CRD absorption spectrum of the weak $b^1\Sigma_g^+(\nu = 1, 2) \leftarrow X^3\Sigma_g^-(\nu = 0)$ bands of molecular oxygen (Figure 2.5). Since then, there has been lot of contributions from various groups proving that this technique is powerful in gas-phase spectroscopy. The factor which makes it useful is that it measures either strong absorptions of species



The green light that is absorbed leads to spontaneous emission of green-yellow light, i.e. fluorescence

Figure 2.3: A demonstration experiment with induced emission detection.

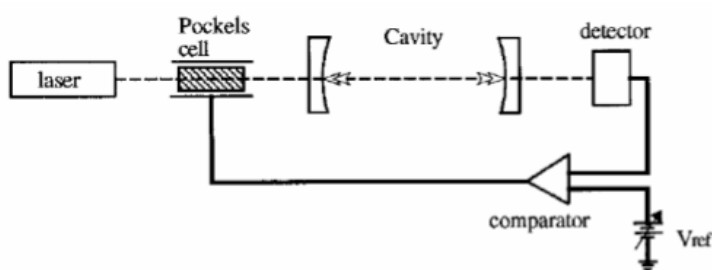


Figure 2.4: Mirror reflectometer. Instead of measuring the phase shift, the intensity decay of the cavity is measured after the light is quickly shut off with a Pockels cell. Ideally, the modes established in the cavity then undergo a first-order exponential decay [3].

present in trace amounts or weak absorptions of abundant species. Although most of the CRD experiments are performed with pulsed lasers, several schemes have been developed and used to perform CRDS with cw lasers. Romanini et al. are one of the pioneers in cw-CRDS [5]. The resonant cavity mode is swept over the cw laser line by varying the cavity length. The light couples and increases in intensity inside the cavity over a certain time. The laser is switched off when the intensity reaches threshold. Subsequently, the CRD transient is recorded.

There are several review papers on CRDS. An historical overview of the development of CRDS can be found in the book edited by Busch and Busch [6], Scherer et al. [3, 7]

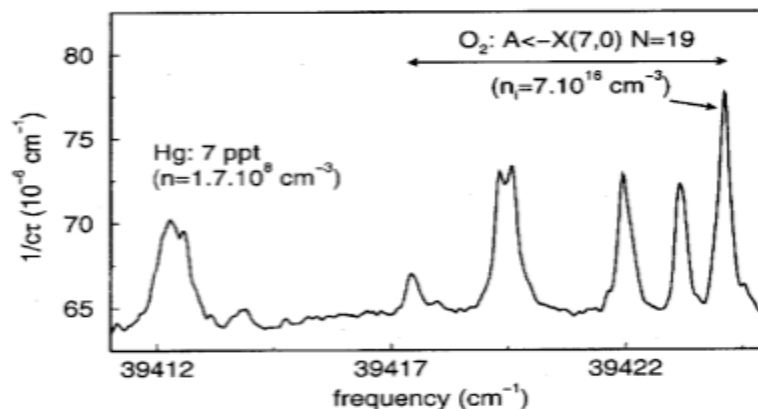


Figure 2.5: CRD absorption spectrum of ambient air around $253 \pm 7 \text{ nm}$ measured in a cavity 45 cm long, using mirrors with a reflection coefficient of only $99 \pm 7\%$. It demonstrates the use of CRDS for trace gas detection (atomic mercury; with the known cross-section for this transition the density of these atoms can be determined) and for measuring absolute cross-sections (molecular oxygen; with the known density the cross-section can be determined). Figure reproduced from [4].

and Paul and Saykally [8] have reviewed the early literature and the application of CRDS to pulsed molecular beams. CRDS can be used for the study of fast (subnanosecond) predissociation of electronically excited states of small molecules and radicals [9], applied to the measurements of radicals in flames [10] and in analytical atomic spectroscopy [11]. The CRD spectra directly provide the absorption strengths of the molecules under study, which contain information on the number density, cross-section and temperature. As long as mirrors with high reflectivity, detectors with a sufficiently fast time response, and tunable light sources are available, there is not any intrinsic limitation to the spectral region where CRD can not be applied. By now, successful application of CRDS has been demonstrated from the ultraviolet (UV) part of the spectrum to the infrared (IR) spectral region. Besides, this is a technique which does not need a vacuum. Attenuated total internal reflection-type experiments can also be done.

2.1.2 Principle

The rate of absorption rather than the magnitude of the absorption of a light pulse confined in an optical cavity is measured. The sample is placed in a high-finesse non-confocal optical cavity made up of two highly reflective mirrors. A pulse or fraction (for cw) of the laser beam is coupled into the cavity, and is reflected back and forth inside cavity by the mirrors. Every time the light strikes mirror, a small fraction leaks out of the cavity. The intensity of the light inside the cavity, therefore, decays as a function of time. The parameter to be determined is the decay time. This is calculated by measuring the time dependence of the light leaking out through the rear mirror of the cavity. Figure 2.6 describes the principle. In an empty cavity, this ring-down transient is a single-exponentially decaying

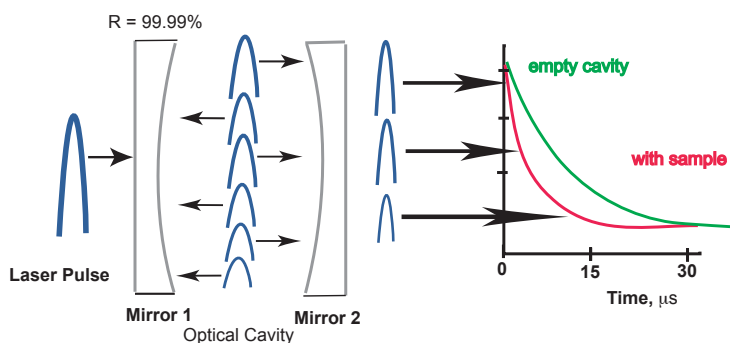


Figure 2.6: Basic principle of cavity ring down spectroscopy.

function of time. The CRD time, $\tau(\nu)$, is defined as the time where the intensity of light at the output of the cavity falls to $1/e$ of the maximum at a particular frequency, ν . $\tau(\nu)$ is solely determined by the reflectivity, $R(\nu)$, of the two mirrors ($R > 99.99\%$), and the optical path length, d , between the mirrors. The light intensity exiting the cavity is given by

$$I(t) = I_0 \exp\left(\frac{-t}{\tau(\nu)}\right) \quad (2.1)$$

where

$$\tau(\nu) = \frac{d}{c(1 - R(\nu))}$$

c is the speed of light. I_0 is the intensity of light incident on the cavity. $R(\nu)$ denotes the effective reflectivity which includes the non-resonant losses by scattering and diffraction (e.g. the Rayleigh cross-section $\sigma_{Ray}(\nu)$ and the Mie cross-section $\sigma_{Mie}(\nu)$), the broadband absorption, and the loss by the mirror reflectivity. The frequency dependence can be neglected over shorter frequency intervals. (2.1) is valid for monochromatic light.

The presence of absorbing species in the cavity gives an additional loss channel for the light inside the cavity. If the absorption of gas-phase species follows Lambert-Beer's law, the light intensity inside the cavity will still decay exponentially. This leads to a decrease in the CRD time,

$$\tau(\nu) = \frac{d}{c[(1 - R(\nu)) + \kappa(\nu)l]} \quad (2.2)$$

where $\kappa(\nu)$ is the absorption coefficient (also frequently denoted as $\alpha(\nu)$) and l is the sample length. During one trip through the cavity, the monochromatic light intensity is diminished by the fraction $\exp[-(\kappa l)]$. The ring-down time $\tau(\nu)$, which is obtained by a single-exponential fit, does not depend on I_0 and is thus not affected by the laser power fluctuations. R determines the baseline of the measured spectrum. The absorption coefficient may be converted to the absorption cross-section $\sigma(\nu) = \alpha(\nu) / C$, if the concentration C of the absorbing species is known.

2.1.3 Cavity modes

For the coupling of light into the optical cavity over a certain frequency range, it is important to consider the mode structure of the cavity. Figure 2.7 shows the behaviour of cavity modes and the light pulse when the cavity length is varied. This mode structure can cause several problems. If narrow molecular absorption features fall between the cavity modes, these will not appear in the spectrum. Furthermore, mode beating, resulting from multimode excitation, can generate oscillations in the ring-down transient. The calculation of the decay times can therefore be not accurate. These effects can be easily circumvented by using a stable optical cavity with a near-continuum mode structure [12, 13]. Such cavity has closely spaced longitudinal and transverse modes. There are a few disadvantages of the continuum-mode approach. The continuum-mode approach

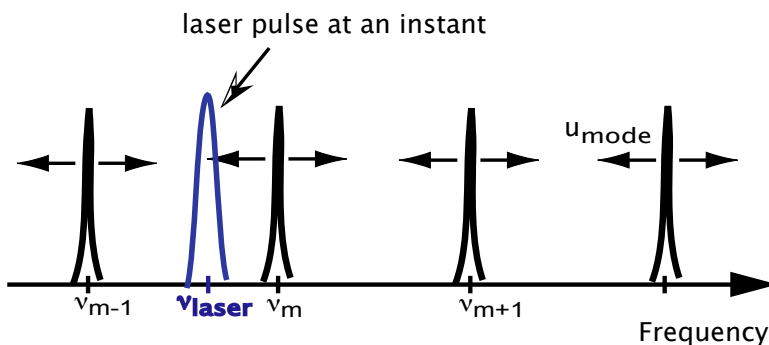


Figure 2.7: Principle of light injection in a cavity passing through the successive moving cavity resonances (TEM_{00} modes). u_{mode} is the tuning speed of the cavity frequencies ν_i .

has certain limitations on the sensitivity which can be achieved [14]. The accuracy in the determination of the decay time is limited by the very small quasirandom variations in the residual transverse mode beating. The spatial resolution is not optimal due to multi-mode excitation of the cavity. Figure 2.8 shows the dependence of mode spectrum on the cavity length. Exciting only longitudinal modes (TEM_{00} mode matching) improves the spatial resolution. This can be implemented by using mode-matching optics to couple the light into the cavity, or by using small-diameter mirrors [15], or by placing apertures in the cavity [16, 14]. The best sensitivity is obtained in such a case giving rise to a truly single-exponential decay [17]. For pulsed CRDS, this can be achieved by combining a Fourier-Transform (FT)-limited pulsed laser with a short cavity. An alternative is the use of cw lasers which have to be switched off in order to observe a ring-down transient. The bandwidth of cw lasers is very small (typically less than a few Megahertz: 500 kHz r.m.s. of Coherent's Autoscan II 899-21 ring laser). This can support longer cavities, resulting in longer ring-down times. A build-up of the intracavity field though will take place if the laser frequency and a cavity mode are in resonance. In the literature, CRDS performed with a cw laser is called cw-CRDS. However, this technique is not a cw technique.

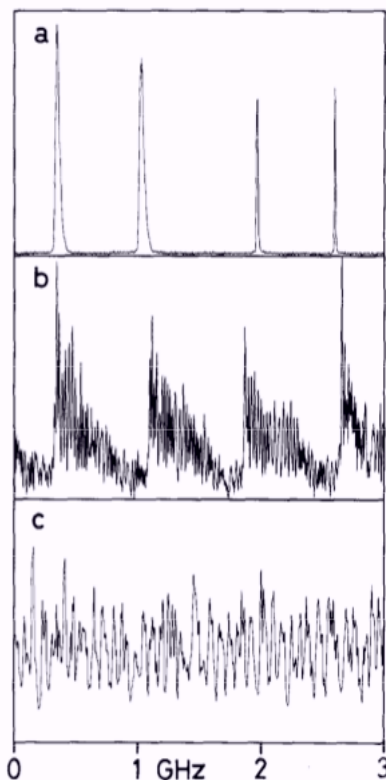


Figure 2.8: Mode-spectrum of the ring down cavity for three different mirror separations d : (a) $d = 10.0$ cm; (b) $d = 10.2$ cm; (c) $d = 11.5$ cm. A rapid congestion of the spectrum is seen when the cavity is detuned from confocal. The spectra are measured by monitoring the transmission of the cavity while a narrowband (≤ 5 MHz) cw UV laser is scanned over 3 GHz (6 GHz/min scan-rate) around 318 nm, reproduced from [12].

2.2 Experimental scheme

In cw-CRDS, there are two methods to measure the photon lifetime in the cavity,

1. the decay of light intensity in the cavity is observed after the laser beam has been switched off [5, 18, 19],
2. the phase shift of an amplitude modulated cw laser beam is measured, which is caused by absorption in the cavity [13].

The narrow bandwidths of cw lasers can be utilized to excite only one cavity mode TEM_{00} but this requires matching the cavity length to the laser frequency. For this reason

several active tracking schemes have been developed [5, 20, 21]. In a pulsed jet experiment, as in the work reported here, such schemes do not work: the gas pulse changes the refraction index, effectively changing the optical length of the cavity, pushing it out of resonance. This effect is further enhanced when plasma fluctuations cause additional instabilities. In this case a passive scheme for mode locking must be used, developed recently [22, 23]. This approach has been implemented in our laboratory [24]. An acousto-

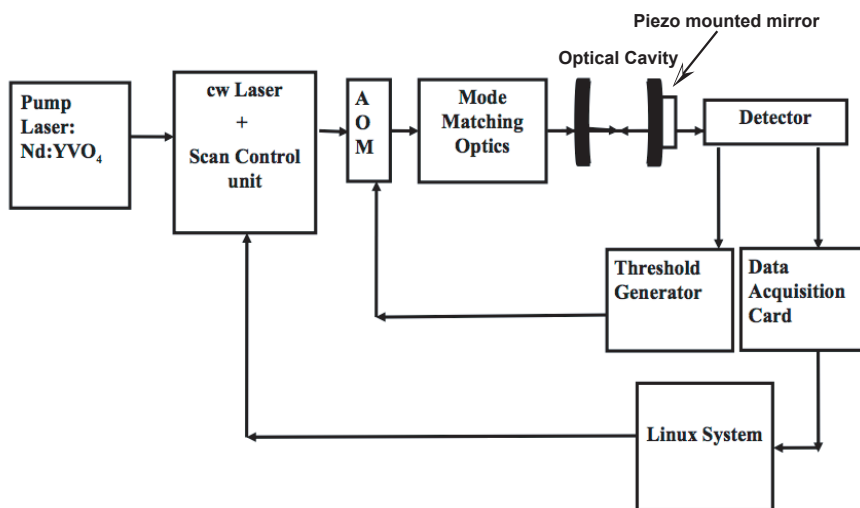


Figure 2.9: Overview of the cw CRDS setup.

optical modulator is used to switch off a cw ring laser, and the cavity is matched to the laser frequency by periodically varying its length. Figure 2.9 gives an overview of the setup. The set-up of the cw-CRD spectrometer has been described in connection with the previously studied species HC_6H^+ , C_3H_2 , etc. in the 600-800 nm region [24, 25, 26].

In the work reported here, the system has been modified to record in the 397-423 nm region. A resonant frequency doubling system is employed for this purpose. A single-mode Ti:Sapphire ring laser pumped by an 8 W solid state laser is used, which is configured for the 790-930 nm range. Its output is channelled through the doubling system and an acousto-optical modulator. The first-order deflection is focused into the ring-down

cavity via a lens to match the geometry of the laser beam to the cavity TEM₀₀ mode. By applying a digital signal to the modulator driver, the deflected beam is switched off within <60 ns. The ring-down cavity is configured as a stable resonator with two plano-concave high-reflectivity mirrors with 1 m curvature separated by 32 cm (Research Electro-Optics Inc $\geq 99.99\%$). A 30 Hz triangular shaped voltage is applied to the piezo mounted on one of the cavity mirrors [22] which makes the cavity tunable to the laser frequency. During each wobble period, the cavity is four times in resonance with the laser frequency. A resonance results in a transmitted light intensity after the cavity which triggers the acousto-optical switch and the data acquisition. In the present experiment, a typical repetition rate of 60 Hz is chosen. Figure 2.10 shows the schematic of the setup. The ring-down cavity is placed in a stainless-steel chamber which is evacuated, with a pulsed slit nozzle to create a discharge plasma in the centre. High-precision gauges with temperature stabilisation are used for measuring the sample pressure. The exiting light is monitored via a fast broad band (UV-VIS-NIR) silicon photodiode (combined with an amplifier, 10 MHz bandwidth) using a data acquisition system. Frequency scanning, data acquisition and analysis are computer controlled. The scanning range encompassed is around 1 cm^{-1} , which arises from the limitation imposed by the frequency doubler. Several decay functions are accumulated, averaged and transferred to a computer. The home made program then determines the ring-down constant B by fitting a single-exponential function to a 3 parameter function.

$$f(t) = A \exp(-Bt) + C \quad (2.3)$$

where: A is amplitude, B: decay rate, C: offset. The final decay time constant is sent, together with the corresponding wavenumber of the laser, to a “scan” program. The program then plots the decay time *vs* wavenumber, which is the CRD spectrum. A 1/e decay time of $8 \mu\text{s}$ of the empty cavity has been obtained. Within this time the laser light makes about 3750 round trips in the cavity and travels 2.4 km, which is a measure for the effective absorption length.

The absorption coefficient is a function of the ring-down time. Spectrum is calibrated using a wavemeter with an accuracy of 0.02 cm^{-1} . The resolution of the recorded spec-

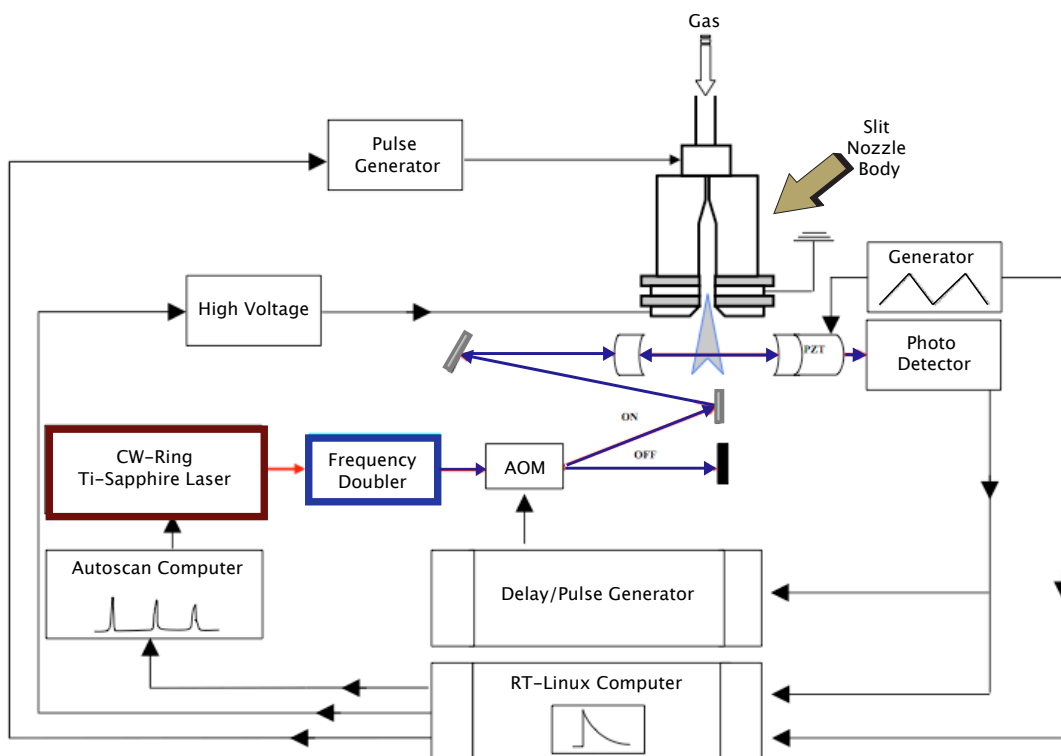


Figure 2.10: Schematic diagram of the cw CRDS experimental setup.

trum is 0.01 cm^{-1} (FWHM) according to the narrowest spectral feature observed. Particular resolution is obtained due to Doppler and lifetime broadening of the gas-phase molecules under study. The contribution of narrow-linewidth, i.e. 500 kHz, of the cw laser is negligible. The cw ring laser with the doubler emits 20–30 mW at 8 W of pump power. The 397–423 nm wavelength range is covered with a sensitivity of 10^{-7} – 10^{-8} cm^{-1} .

2.2.1 Frequency doubler

To utilize the properties of the cw-CRDS setup to the fullest and make it more versatile, a frequency doubler has been added to the set up. The tunability of the setup is extended to the region of 396–423 nm. This made the high resolution study of the radicals in 400 nm region, possible. The doubler is an external unit with a stable cavity, so, independent

of the internal alignment of the fundamental laser source. Resonant frequency doubling

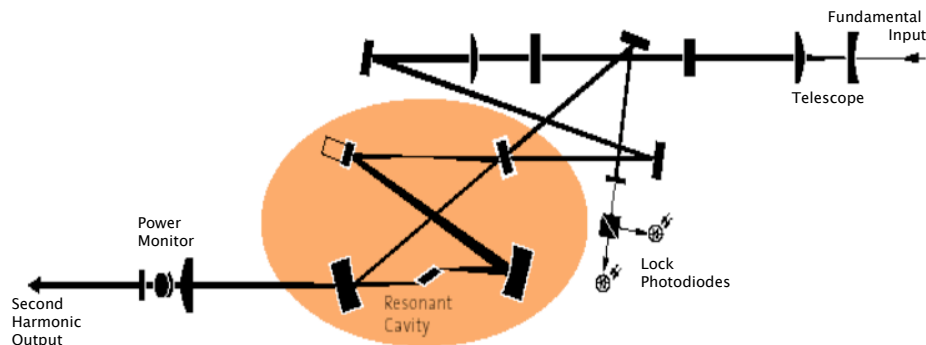


Figure 2.11: Schematic diagram of the frequency doubler [provided by Coherent].

is most frequently applied for continuous wave laser beams from single frequency lasers. Such a monolithic resonant frequency doubler is most stable, compact and efficient. In any case, one usually has to stabilize the resonance condition with an automatic feedback system. A Monolithic Block Doubler (MBD)-200 from Coherent has been used in the work presented here. Singly-resonant frequency doubling is usually based on the resonant enhancement of the pump wave only, while the second-harmonic wave is coupled out of the resonator. Figure 2.11 illustrates the implementation of the frequency doubling. A selected frequency-doubling crystal (Lithium Triborate, in present case) is positioned at the intracavity focus. The power of the fundamental laser beam is enhanced in a highly stable external cavity. The enhancement increases the conversion efficiency in each pass as high resonant power is essential for *efficient* nonlinear processes. Also note that a very high effective conversion efficiency requires only a conversion efficiency of a few percent per pass, because the remaining pump power is recycled in the cavity. This also means that the pump intensity can be kept at a lower level than would be required to achieve the same efficiency in single pass doubling. An efficiency of 10% has been observed. Figure 2.12 shows the performance of the doubler over the wavelength range of the fundamental laser.

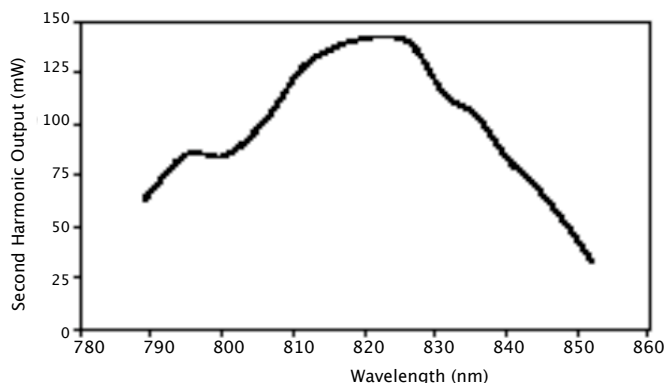


Figure 2.12: Typical response of the frequency doubling system, MBD-200 [provided by Coherent].

2.2.2 Source of radicals

The hydrocarbon molecules are generated in a plasma. The plasma is produced by applying a high voltage through a gas pulse passing through the throat of a 3 cm x 200 μ m multilayer slit nozzle [27, 24]. The dynamics of a planar flow generated by the pulsed discharge slit nozzle have been numerically investigated [28]. The gas used, in general, is acetylene in excess of helium (He) or argon (Ar). The optimized experimental conditions vary with the target molecules though.

Plasmas are ionized gases. Hence, they consist of positive and negative ions and electrons as well as neutral species. Much of the visible matter in the universe is in the plasma state. The astropasmas are omnipresent in the universe. Besides, we can also distinguish two main groups of laboratory plasmas, i.e. the high-temperature or fusion plasmas, and the so-called low-temperature plasmas or gas discharges. In general, a subdivision can be made between plasmas which are in thermal equilibrium and those which are not in thermal equilibrium. Often, the term 'local thermal equilibrium' (LTE) is used, which implies that the temperatures of all plasma species are the same in localized areas in the plasma. 'Non-LTE' is used for the case where the temperatures of the different plasma species are not the same. The gas discharge plasmas can also be classified into LTE and non-LTE plasmas related to the pressure in the plasma.

Direct current (d.c.) glow discharges When a sufficiently high voltage is applied between the two electrodes placed in a gas, the gas breaks down into positive ions and electrons which gives rise to a gas discharge. The mechanism of the gas breakdown is explained as follows [29]: a few electrons are emitted from the electrodes due to the omnipresent cosmic radiation. Without applying a potential difference, the electrons emitted from the cathode are not able to sustain the discharge. However, when a potential difference is applied, the electrons are accelerated by the electric field in front of the cathode and collide with the gas atoms (Figure 2.13). The most important collisions are the inelastic collisions, leading to excitation and ionization. The excitation collisions, followed by de-excitations with the emission of radiation, are responsible for the characteristic name of the 'glow' discharge. The ionization collisions create new electrons and ions. The ions are accelerated by the electric field toward the cathode, where they release new electrons by ion-induced secondary electron emission. The electrons give rise to new ionization collisions, creating new ions and electrons. These processes of electron emission at the cathode and ionization in the plasma make the glow discharge a self-sustaining plasma. When a constant potential difference is applied between the cathode and anode, a continuous current will flow through the discharge; giving rise to a direct current (d.c.) glow discharge. It should be mentioned that in a d.c. glow discharge the electrodes play an essential role for sustaining the plasma by secondary electron emission.

A detailed description/compilation on the production and characteristics of slit discharges is given in [30]. In the present case the CCCCH_3^+ radical is produced by discharging a gas mixture of 0.3% acetylene in Ar at a voltage pulse of -700 V with a backing pressure of 9 bar. The laser beam crosses the supersonic jet 8 mm downstream. A typical rotational temperature of 15-40 K is obtained.

2.2.3 Advantages

The cavity ring-down (CRD) technique, in general, has proven to be a valuable invention since it combines a good sensitivity with a simple and straightforward experimental setup. High sensitivity is achieved as

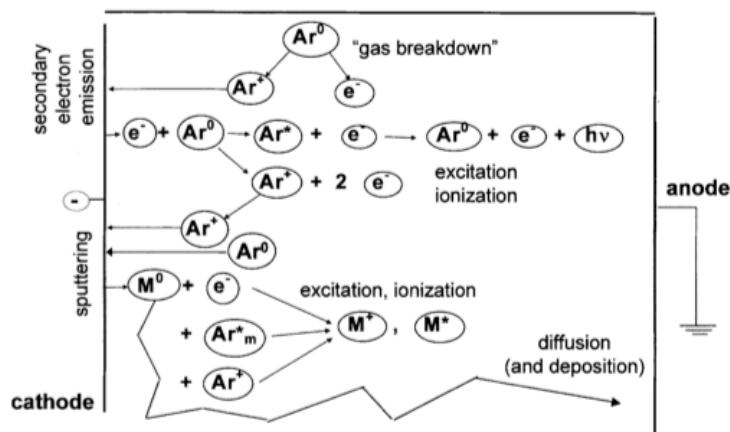


Figure 2.13: Schematic overview of the basic plasma processes in a glow discharge. When a potential difference is applied between two electrodes, the gas (e.g. argon) will break down into electrons and positive ions. The latter can cause secondary electron emission at the cathode. The emitted electrons give rise to collisions in the plasma, e.g. excitation (which is often followed by de-excitation with emission of radiation; hence explaining the name of the 'glow' discharge) and ionization (which creates new electrons and ions, and therefore makes the glow discharge a self-sustaining plasma) [29].

- the absorption is determined from the time behaviour of the signal and is independent of pulse-to-pulse fluctuations of the laser.
- the effective absorption path length can be very long due to the reflective mirrors (up to several kilometres) while the sample volume is kept small.
- the absorption is measured on an absolute scale.

The CRD technique can be applied even when the molecule's excited state does not fluoresce (a requirement for LIF) or cannot be ionized (a prerequisite for REMPI). In high-pressure samples, such as flames and plasmas, CRD can be successfully used to extract quantitative information. This is nearly impossible by either LIF (the collisional quenching of the fluorescing state) or by REMPI (difficulties in extracting the charged particles). Figure 2.14 compares the results. cw-CRD provides a better spectral resolution and duty cycle. Furthermore, the sensitivity of cw-CRD can in principle be improved by specific coupling (TEM_{00}) of the laser modes to the cavity modes. In addition, there is an increased

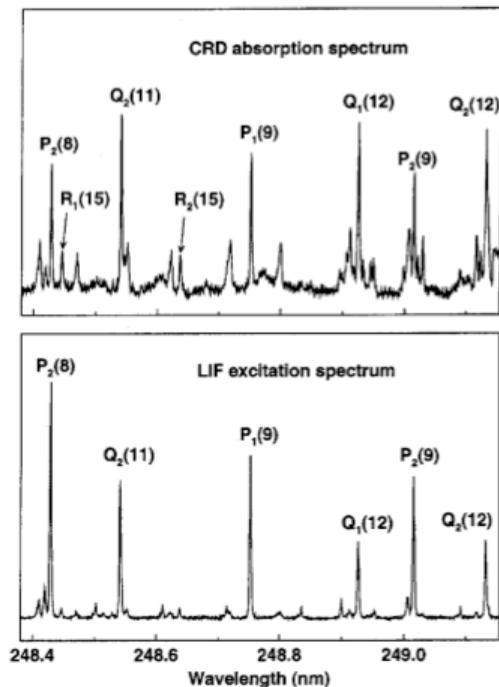


Figure 2.14: Part of the $A^2\Sigma^+(\nu' = 3) \leftarrow X^2\Pi(\nu'' = 0)$ spectrum of OH, measured simultaneously by CRD and LIF spectroscopy in a laminar methane-air flame at atmospheric pressure. Figure reproduced from [31].

energy build-up inside the cavity as the linewidth of the cw laser decreases. Higher intra-cavity energy results in higher light intensity on the detector, which improves the signal-to-noise ratios on the ring-down transients, leading to higher sensitivity.

2.2.4 Shortcomings

- In general CRDS, though more sensitive, cannot match with the background-free detection techniques like LIF or REMPI.
- cw lasers can be scanned over only small wavelength regions and are not (yet) available in all wavelength regions unlike pulsed lasers.

2.3 Abstract

In the past few decades progress has been made in the electronic spectroscopy of unsaturated carbon-chain radicals both in neon matrices and gas phase [32]. Once spectroscopic information becomes available a systematic comparison between laboratory and astronomical data can be made [33]. A high-resolution gas-phase electronic spectrum has been detected in the 408 nm region using a cw cavity ring-down spectrometer. The absorption band system is observed in a plasma which was produced in a pulsed slit nozzle discharge with a mixture of acetylene in argon. The rotationally resolved spectrum obtained is that of a symmetric top molecule. Considerations of the constants and *ab-initio* calculations leads to the assignment ${}^3E \leftarrow X^3E$ transition of the linear carbon chain species $CCCCH_3^+$ in the triplet ground electronic state with C_{3v} symmetry.

2.4 Results and discussion

A rotationally resolved molecular absorption band has been detected in the 408 nm region. The initial aim was to record the previously observed $\tilde{A}^2B_1 - \tilde{X}^2A_2$ band of the allyl radical at higher resolution [34]. However, the rotational lines obtained have been found to constitute a different pattern from the previous one, especially the presence of many doublets of comparable intensity. This observation is made possible by the use of a cw laser with narrow bandwidths, which helped to achieve 0.01 cm^{-1} (FWHM) resolution in the recorded spectrum. This can be compared with the $0.05\text{-}0.06 \text{ cm}^{-1}$ linewidth of the pulsed dye laser used in the previous experiment (Figure 2.15). The difference indicates that some other molecule is the absorber. The doublets are produced by parallel transitions of a prolate molecule with a large rotational constant A . The $K = 0$ and 1 levels produce doublets for each J , and the $K \geq 2$ levels are less populated at low temperature. This leads to the speculation that molecular structure must be a symmetric-top and therefore could not be assigned to the allyl radical. The rotational lines are assigned as shown in Figure 2.16 by simulating parallel transition of a molecule. The rotational temperature was found to be 20 K.

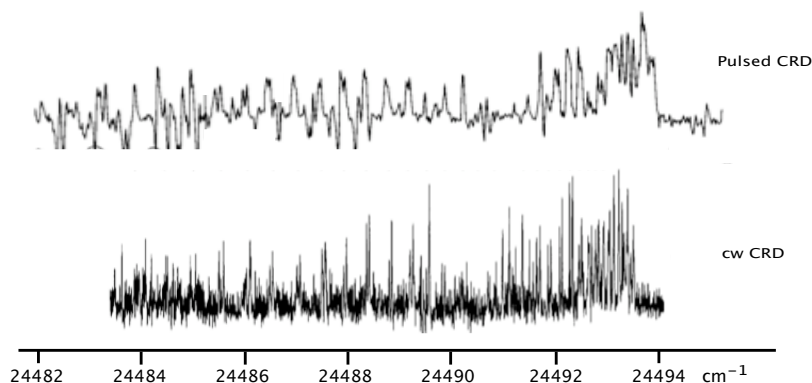


Figure 2.15: Difference in the observations by pulsed and cw cavity ring down spectroscopy.

The analysis was carried out with a conventional rotational Hamiltonian using the program 'WANG' [35]. The WANG program was designed to allow, in principle, inclusion of all types of rovibrational interactions in the analysis without the need for fundamental changes in the program. Even though the experimental conditions were inferred by the strong spectral lines, the intensity of peaks is rather qualitative because of fluctuations in the laser output (the power is weak around 24490 cm^{-1} , and fluctuates in the 24491 cm^{-1} region). Therefore lines in these two regions were taken out of the analysis. Moreover, lines of high- J levels were also excluded in the final fit because of their poor S/N ratio. In total 25 lines were used to obtain the molecular constants given in table 2.1. The standard deviation of the fit was 0.0115 cm^{-1} . The upper limit value of the root mean square deviation was set to be lower than 0.02 cm^{-1} , the estimated experimental accuracy. The analysis yields the constants $B'' = 0.14165(44)\text{ cm}^{-1}$, $B' = 0.13304(55)\text{ cm}^{-1}$, and $\delta A = 0.0478(105)\text{ cm}^{-1}$ with the electronic transition at $\nu = 24491.05(108)\text{ cm}^{-1}$. The carrier of the new band must be either a symmetric top hydrocarbon molecule produced in the discharge, or a hydrocarbon complexed with Ar. Observation of some of the same strong bands when using He as the buffer gas excludes the latter.

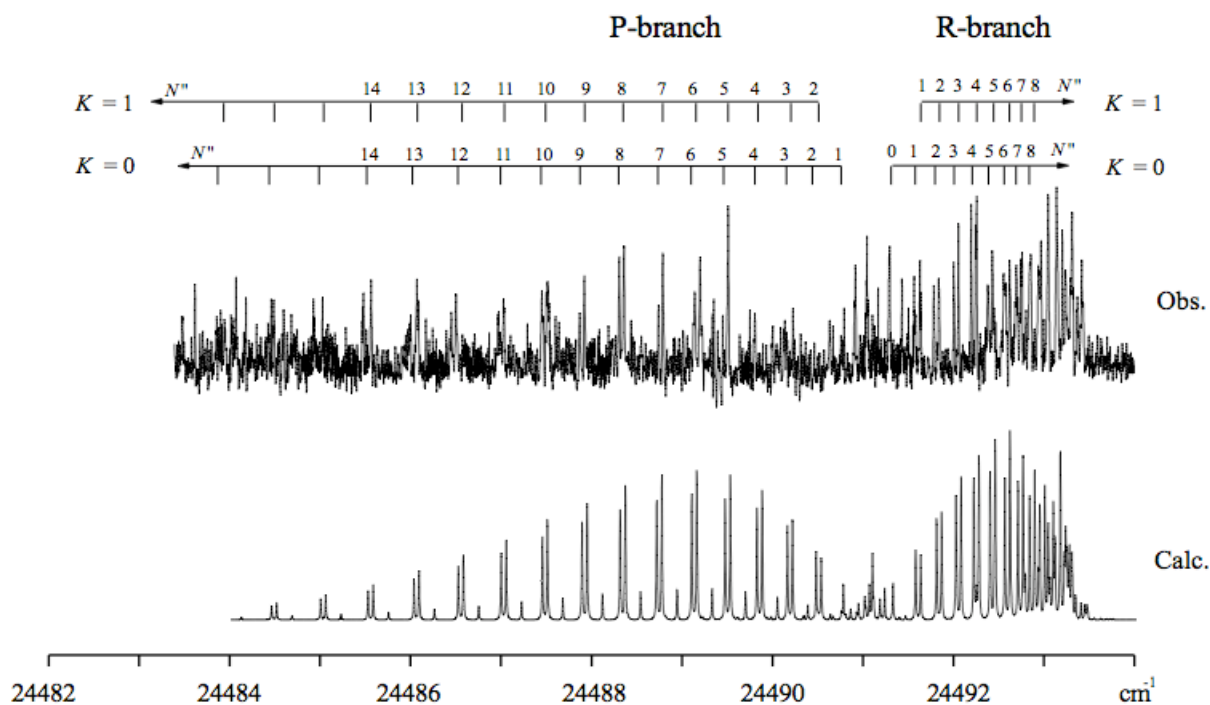


Figure 2.16: Rotationally-resolved ${}^3E \leftarrow X^3E$ electronic absorption spectrum of $CCCCH_3^+$. The lower trace is a simulation with the rotational constants determined (table 2.1). The $K = 2$ lines are hardly observable with the S/N attained.

Table 2.1: Molecular constants of $CCCCH_3^+$ (cm^{-1})^a

B''	0.14165(44)
ΔA	0.0478(105)
ΔB	-0.00861(55)
ν	24491.0500(108)
<i>rms</i>	0.0115 ^b

^aValue in parentheses is the standard 2σ deviation.

^bUncertainty of the calibration is 0.02 cm^{-1} .

In view of the determined rotational constant, hydrocarbon molecules containing only four carbons, such as C_4H_4 , C_4H_3 , C_4H_2 , and their ions are possible carriers. Among these, H_2CCCCH_2 , $HCCCCH_3$, $HCCCCH_2$, $CCCCH_3$, and $CCCCH_2$ are symmetric or near-symmetric top molecules. On the basis of the information from previous theoretical

studies on these species [36, 37, 38], as well as the optimized structure calculated by DFT theory, only HCCCCH₂ and CCCCH₃ are compatible with the obtained rotational constants. Although the rotational constants of HCCCCH₂ and HCCCCH₂⁺ calculated from the predicted geometry are reasonable ($B \sim 0.137 \text{ cm}^{-1}$ and $C \sim 0.135 \text{ cm}^{-1}$ for neutral, $B \sim 0.139 \text{ cm}^{-1}$ and $C \sim 0.137 \text{ cm}^{-1}$ for cation), the slight difference between them ($B - C = 0.002 \text{ cm}^{-1}$) would result in non-negligible $K_a = 1$ asymmetric splittings. This is not seen in the spectrum (Figure 2.16). On the other hand, CCCCH₃ is a symmetric-top molecule, suggesting this molecule to be a good candidate for the observed absorption spectrum.

In order to help the assignment, *ab initio* calculations for neutral CCCCH₃ and its cation have been carried out with Density Functional Theory (DFT) and time dependent (TD)-DFT theory using the Gaussian program [39]. Geometry optimization for the neutral CCCCH₃ doublet state [36] and the cation singlet [37] have been reported. DFT gives $B \sim 0.136 \text{ cm}^{-1}$ in the ground state for the CCCCH₃ structure, which is outside the error limit of the rotational constant inferred from the analysis of the spectrum (table constants). In the case of CCCCH₃⁺, the rotational constant in the ground state is predicted to be 0.140 cm^{-1} in agreement with the experimental result.

To obtain the symmetry of the electronic transition, TD-DFT calculations for CCCCH₃⁺ in both singlet and triplet ground states have been carried out. For the singlet states vertical transitions to the first four excited electronic states have no parallel electric dipole moment and have excessive transition energies. On the other hand, the triplet state of CCCCH₃⁺ gives rise to a parallel electronic transition from the ground to the fourth excited state at around 414 nm, the region where the molecular band is observed. Table 2.2 and table 2.3 list the optimized geometries, rotational constants, vertical transition energy, and the oscillator strength of CCCCH₃⁺ calculated at the B3LYP/cc-pVTZ level.

Thus, the observed absorption system can be assigned to CCCCH₃⁺ in the triplet ground state. The rotational analysis indicates CCCCH₃⁺ is prolate symmetric and its symmetry is considered as C_{3v} . This ion possesses three identical atoms of nuclear spin- $\frac{1}{2}$ off the main axis, so that the total eigenfunction is either A or E symmetry. Because most of the lines originate from $K < 2$ at the low experimental temperature of 20 K, and the K doubling

Table 2.2: Optimized geometries (in Å and degrees) for the $CCCCH_3^+$ for the 3E ground electronic state using DFT theory at B3LYP / cc-pVTZ level.

	cc-pVTZ
$r_{C_1C_2}$	1.410
$r_{C_2C_3}$	1.267
$r_{C_3C_4}$	1.261
$r_{C_1H_{1,2,3}}$	1.099
$\angle C_2C_1H_{1,2,3}$	110.3
$\angle H_1C_1H_{2,3}$	108.7
$\angle H_2C_1H_3$	108.7

Table 2.3: Rotational constants in the 3E ground state, vertical transition energy and oscillator strength for the observed parallel electronic transition of $CCCCH_3^+$ using DFT and TD-DFT theories at B3LYP/cc-pVTZ level.

	cc-pVTZ
A/cm^{-1}	5.245
B/cm^{-1}	0.140
$^3E \leftarrow X^3E/\text{eV}$	2.989
$f_4 \leftarrow x$	$f \approx 3 \times 10^{-4}$

is not resolved as is usually the case, the expected intensity distribution of the spectrum was calculated by taking into account the statistical weight for C_{3v} symmetry described in the table 3.11 of [40] (i.e. $K = 0$ and $K = 1$ each having a statistical weight of 4, $4A_1$ (J even) or $4A_2$ (J odd) in the $K=0$ level and $2A_1+2A_2$ in the $K=1$ level), which agrees well with the observed result (Figure 2.16).

The lines in the 408 nm region detected in both the pulsed- and cw-CRD spectra match within the frequency accuracy ($\sim 0.07\text{cm}^{-1}$) common to both experimental set-ups. Ten P-branch lines ($N = 5-6$ to $9-10$) observed with the cw CRD spectrometer clearly match the five lines observed previously as listed in [34]. Each of these peaks appears to split into two when scanned with higher resolution. The doublets clearly indicate that these lines observed at lower resolution cannot be due to the allyl radical as previously assigned; the unresolved lines are actually due to $CCCCH_3^+$. However, one can be sure some of the other absorptions also observed in [34] are due to the allyl radical because of the vibrational assignments and the shifts observed upon deuteration.

2.5 Conclusion

The electronic spectrum of the hydrocarbon cation CCCCH_3^+ has been detected in the 408 nm region for the first time. The assignment is based on the inferred rotational constants, *ab initio* calculation of the geometry, and the excitation energy calculated with DFT and TD-DFT theories. It is not clear whether the observed electronic band is the origin because of the limited scanning range of the cw CRD set-up.

The present results show that the P-branch lines which were previously assigned to the allyl radical (C_3H_5) [34], are actually rotational transitions from CCCCH_3^+ . The new assignment for deuterated allyl radical leads to the rotational constants $\Delta A = -0.04187(4) \text{ cm}^{-1}$, $\Delta 1/2(B + C) = -0.029366(12) \text{ cm}^{-1}$, and the transition frequency $T_{00} = 24550.3238(6) \text{ cm}^{-1}$. Although both CCCCH_3^+ and the allyl radical are produced in the pulsed CRD set-up, only CCCCH_3^+ is observed using the cw CRD spectrometer. This may be because the discharge source used in the two instruments runs under different experimental conditions, particularly with respect to density, leading to production of species with different rotational temperatures. The obtained rotational constants may be useful for the measurement of a pure-rotational spectrum of this cation in the radio frequency region in the laboratory and by radio astronomy.

Bibliography

- [1] Herbelin, J. Mckay, M. Kwok, R. Ueunten, and D. Urev, *Appl. Opt.*, 1980, **19**, 144.
- [2] D. Z. Anderson, J. C. Frisch, and C. S., *Appl. Opt.*, 1984, **23**, 1238.
- [3] J. J. Scherer, J. B. Paul, A. O' Keefe, and R. J. Saykally, *Chem. Rev.*, 1997, **97**, 25.
- [4] R. T. Jongma, M. G. H. Boogaarts, I. Holleman, and G. Meijer, *Rev. Sci. Instrum.*, 1995, **66**, 2821.
- [5] D. Romanini, A. A. Kachanov, N. Sadeghi, and F. Stoeckel, *Chem. Phys. Lett.*, 1997, **264**, 316.
- [6] *Cavity-Ringdown Spectroscopy, An Ultratrace-Absorption Measurement Technique*, ed. K. W. Busch and M. A. Busch, American Chemical Society, 1999.
- [7] J. J. Scherer, J. B. Paul, A. O' Keefe, and R. J. Saykally, *Advances in Metal and Semiconductor Clusters*, Vol. 3, JAI Press, 1995.
- [8] J. B. Paul and R. J. Saykally, *Anal. Chem.*, 1997, **69**, 287.
- [9] M. D. Wheeler, S. M. Newman, A. J. Orr-Ewing, and M. N. R. Ashfold, *J. Chem. Soc., Faraday Trans.*, 1998, **94**, 337.
- [10] S. Cheskis, *Prog. Energy Combust. Sci.*, 1999, **25**, 233.
- [11] G. P. Miller and C. B. Winstead, *J. Anal. Atom. Spect.*, 1997, **12**, 907.
- [12] G. Meijer, M. G. H. Boogaarts, R. T. Jongma, D. H. Parker, and A. M. Wodtke, *Chem. Phys. Lett.*, 1994, **217**, 112.
- [13] R. Engeln, G. von Helden, G. Berden, and G. Meijer, *Chem. Phys. Lett.*, 1996, **262**, 105.
- [14] J. T. Hodges, J. P. Looney, and R. D. van Zee, *J. Chem. Phys.*, 1996, **105**, 10278.
- [15] D. Romanini and K. K. Lehmann, *J. Chem. Phys.*, 1993, **99**, 6287.

- [16] P. Zalicki, Y. Ma, R. N. Zare, E. H. Wahl, J. R. Dadamio, T. G. Owano, and C. H. Kruger, *Chem. Phys. Lett.*, 1995, **234**, 269.
- [17] R. D. van Zee, J. T. Hodges, and J. P. Looney, *Appl. Opt.*, 1999, **38**.
- [18] B. Paldus, J. Harris, J. Martin, J. Xie, and R. Zare, *J. Appl. Phys.*, 1997, **82**, 3199.
- [19] D. Romanini, A. Kachanov, and F. Stoeckel, *Chem. Phys. Lett*, 1997, **270**, 538.
- [20] B. Paldus, C. Harb, T. Spence, B. Wilke, J. Xie, J. Harris, and R. Zare, *J. Appl. Phys.*, 1998, **83**, 3991.
- [21] M. Murtz, B. Frech, and W. Urban, *Appl. Phys. B.*, 1999, **68**, 243.
- [22] M. Hipper and M. Quack, *Chem. Phys. Lett*, 1999, **314**, 273.
- [23] Y. He, M. Hippler, and M. Quack, *Chem. Phys. Lett.*, 1998, **289**, 527.
- [24] P. Birza, T. Motylewski, D. Khoroshev, A. Chirokolava, H. Linnartz, and J. Maier, *Chem. Phys.*, 2002, **283**, 119.
- [25] D. Khoroshev, M. Araki, P. Kolek, P. Birza, A. Chirokolava., and J. P. Maier, *J. Mol. Spectros*, 2004, **227**, 81.
- [26] P. Birza, A. Chirokolava., M. Araki, P. Kolek., and J. P. Maier, *J. Mol. Spectros*, 2005, **229**, 276.
- [27] T. Motylewski and H. Linnartz, *Rev. Sci. Instrum.*, 1999, **70**, 1305.
- [28] L. Biennier, A. Benidar, and F. Salama, *Chem. Phys.*, 2006, **326**, 445.
- [29] A. Bogaerts, E. Neyts, R. Gijbels, and J. van der Mullen, *Spectrochim. Acta B*, 2002, **57**, 609.
- [30] D. Khoroshev *Electronic spectroscopy of carbon chain radicals using cw cavity ring down in conjunction with mass detection* PhD thesis, Universität Basel, Philosophisch-Naturwissenschaftlichen Fakultät, 2005.
- [31] J. J. L. Spaanjaars, J. J. ter Meulen, and G. Meijer, *J. Chem. Phys.*, 1997, **107**, 2242.
- [32] J. P. Maier, *J. Phys. Chem. A*, 1998, **102**, 3462.
- [33] T. Motylewski, H. Linnartz, O. Vaizert, J. P. Maier, G. A. Galazutdinov, F. A. Musaev, J. Krelowski, G. A. H. Walker, and D. A. Bohlender, *Astrophys. J.*, 2000, **531**, 312.
- [34] E. Achkasova, M. Araki, A. Denisov, and J. P. Maier, *Mol. Phys.*, 2005, **103**, 1555.
- [35] D. Luckhaus and M. Quack, *Mol. Phys.*, 1989, **63**, 745.
- [36] T. N. Le, A. M. Mebel, and R. I. Kaiser, *J. Comp. Chem.*, 2001, **22**, 1522.

- [37] D. Schroder, H. S. J. Loos, R. Thissen, J. Roithova, and Z. Herman, *Int. J. Mass Spectrom.*, 2003, **230**, 113.
- [38] R. L. Kaser, A. M. Mebel, Y. T. Lee, and A. H. H. Chang, *J. Chem. Phys.*, 2001, **115**, 5117.
- [39] M. J. Frisch, Gaussian.
- [40] H. W. Kroto, *Molecular Rotation Spectra*, Dover Publications Inc., New York, 1992.

Electronic spectrum of the hydrocarbon cation CCCCH_3^+

E. KIM*, M. ARAKI†, R. CHAUHAN, P. BIRZA‡ and J. P. MAIER

University of Basel, Basel, Switzerland

(Received 15 February 2006; in final form 22 March 2006)

A high-resolution gas-phase electronic spectrum has been detected in the 408 nm region using a cw cavity ring-down spectrometer. The absorption band system is observed using a pulsed slit nozzle discharge with a mixture of acetylene in argon. The rotationally resolved spectrum obtained is that of a symmetric top molecule. The determined constants are $\nu = 24491.0500$ (108) and $B' = 0.14165$ (44) cm^{-1} . Consideration of the latter value and *ab initio* calculations leads to the assignment ${}^3E \leftarrow X^3E$ transition of the linear carbon chain species CCCCH_3^+ in the triplet ground electronic state with C_{3v} symmetry.

1. Introduction

Highly-unsaturated carbon chains have been of interest as reactive intermediates in interstellar hydrocarbon chemistry [1], combustion [2], and discharge processes [3]. Spectral analysis allows their identification in extraterrestrial environments and to infer the condition prevailing there. In the past few decades progress has been made in the electronic spectroscopy of unsaturated carbon-chain radicals both in neon matrices and gas phase [4]. Once spectroscopic information becomes available a systematic comparison between laboratory and astronomical data can be made [5].

High-resolution experimental techniques such as cavity ring-down (CRD) spectroscopy [6, 7] allow the detection of rotationally resolved electronic absorption spectra of hydrocarbon radicals. By using a single-mode cw laser combined with a pulsed slit nozzle discharge, rotationally resolved electronic transitions of linear and nonlinear carbon chains have been measured [8, 9]. In this investigation the gas-phase electronic spectrum of a new hydrocarbon cation, CCCCH_3^+ , has been detected and the well resolved rotational structure analyzed.

2. Experimental

The set-up of the cw cavity ring-down spectrometer has been described in connection with previously studied species HC_6H^+ , C_6H_4^+ , C_3H_2 in the 600–800 nm region [8–10]. The hydrocarbon molecules are generated in a plasma by applying a high voltage through a gas pulse of acetylene in excess of He or Ar in the throat of a $3 \text{ cm} \times 200 \mu\text{m}$ multilayer slit nozzle. Optimized experimental conditions vary with the target molecules. Typically 15–40 K rotational temperatures are obtained. In the present case the CCCCH_3^+ radical is produced by discharging a gas mixture of 0.3% acetylene in Ar at a voltage pulse of -700 V with a backing pressure of 9 bar. The laser beam crosses the supersonic jet 8 mm downstream.

The instrument has been modified to record in the 397–423 nm region. A resonant frequency doubling system is employed. A single-mode Ti:Sapphire ring laser pumped by an 8 W solid state laser is used in the 790–930 nm range. Its output is channelled through the doubling system and an acousto-optical modulator. The first-order deflection is focused into the ring-down cavity via a lens (1 m plano-concave, $R > 99.99\%$) that matches the TEM_{00} cavity mode. A 30 Hz triangular shaped voltage is applied to the piezo mounted on one of the cavity mirrors [11]. A resonance results in a transmitted light intensity after the cavity and is monitored via a Si photodiode using a data acquisition system. The absorption coefficient is obtained as a function of ring-down time, and the spectrum is calibrated using a wavemeter with an accuracy of 0.02 cm^{-1} . The resolution of the recorded spectrum

*Corresponding author. Email: Eunsook.Kim@unibas.ch

†Present address: Department of Basic Science, Graduate School of Arts and Sciences, The University of Tokyo, Komaba, Meguro-ku, Tokyo 153-8902, Japan.

‡Present address: PALMS-UMR 6627 du CNRS, Université de RENNES 1, Campus de Beaulieu, 35042 RENNES Cedex, France.

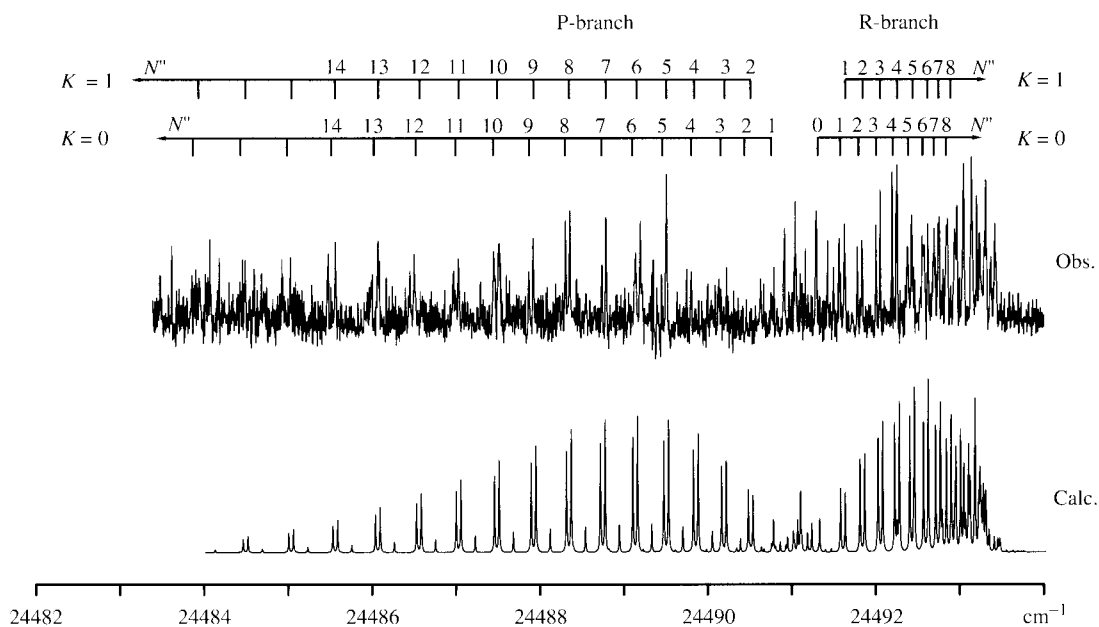


Figure 1. Rotationally-resolved ${}^3E \leftarrow X^3E$ electronic absorption spectrum of CCCCH_3^+ . The lower trace is a simulation with the rotational constants determined (table 2). The $K=2$ lines are hardly observable with the S/N attained.

is 0.01 cm^{-1} (FWHM) according to the narrowest spectral features. The linewidth is due to Doppler and lifetime broadening while the 500 kHz contribution of the laser is negligible. The 397–423 nm wavelength range is covered with a sensitivity of 10^{-7} – 10^{-8} cm^{-1} .

The experiment (discussed in section 3.2) consisted of a pulsed CRD set-up sampling a plasma generated in a pulsed supersonic jet with a $3 \text{ cm} \times 300 \mu\text{m}$ multilayer slit nozzle [12]. The C_3D_5 radicals were synthesized in the discharge of a gas pulse (30 Hz repetition rate, 10 bar backing pressure, 100 mA at -600 V applied voltage) of 0.3% C_2D_2 in an Ar mixture. At 2 mm downstream from the slit nozzle the radicals are cooled in the expansion to about 20–40 K. The excimer pumped dye laser system combined with an etalon used had 0.05 – 0.06 cm^{-1} linewidth. The light leaking out of the ring-down cavity was detected by a photodiode. The spectra were calibrated using a wavemeter with an accuracy of 0.05 cm^{-1} .

3. Results and observations

3.1. Electronic transition of CCCCH_3^+

A rotationally resolved molecular absorption band has been detected in the 408 nm region. The initial aim was to record the previously observed $\tilde{A}^2B_1 \cdot \tilde{X}^2A_2$ band of the allyl radical at higher resolution [12]. However, the observed pattern of rotational lines, especially the presence of many doublets of comparable intensity

(figure 1), indicates that another molecule is the absorber. The doublets are produced by parallel transitions of a prolate molecule with a large rotational constant A . The $K=0$ and 1 levels produce doublets for each J , and the $K \geq 2$ levels are less populated at low temperature. Thus the molecular structure must be a symmetric-top and therefore can not be assigned to the allyl radical.

The rotational lines are assigned as shown in figure 1 by simulating parallel transition of a molecule. The rotational temperature was found to be 20 K. The frequencies of the observed lines are listed in table 1.

The analysis was carried out with a conventional rotational Hamiltonian using the program ‘WANG’ [13]. Even though the experimental conditions were monitored by the strong spectral lines, the intensity of peaks is rather qualitative because of various fluctuation in the laser output (the power is weak around 24490 cm^{-1} , and fluctuates in the 24491 cm^{-1} region). Therefore lines in these two regions were taken out of the analysis. Moreover, lines of high- J levels were also excluded in the final fit because of their poor S/N. In total 25 lines were used to obtain the molecular constants given in table 2. The standard deviation of the fit was 0.0115 cm^{-1} . The upper limit value of root mean square was set to be lower than 0.02 cm^{-1} , the estimated experimental accuracy. The analysis yields the constants $B'' = 0.14165$ (44) cm^{-1} , $B' = 0.13304$ (55) cm^{-1} , and $\Delta A = 0.0478$ (105) cm^{-1} with the electronic transition at $\nu = 24491.0500$ (108) cm^{-1} .

Table 1. Assignment and frequencies for the observed rotational lines of CCCCH_3^+ .

N'_K		N''_K	ν_{obs} (cm^{-1})	$o-c$ (cm^{-1})
1 ₀	–	0 ₀	24491.2928	–0.0233
2 ₀	–	1 ₀	24491.5795	0.0146
2 ₁	–	1 ₁	24491.6408	0.0195
3 ₀	–	2 ₀	24491.7984	0.0018
3 ₁	–	2 ₁	24491.8468	–0.0062
4 ₀	–	3 ₀	24492.0073	–0.0037
4 ₁	–	3 ₁	24492.0574	–0.0100
5 ₀	–	4 ₀	24492.2064	–0.0017
5 ₁	–	4 ₁	24492.2562	–0.0083
6 ₀	–	5 ₀	24492.3871	–0.0010
6 ₁	–	5 ₁	24492.4433	–0.0012
7 ₀	–	6 ₀	24492.5593	0.0085
7 ₁	–	6 ₁	24492.6199	0.0127
8 ₀	–	7 ₀	24492.6937	–0.0026
8 ₁	–	7 ₁	24492.7505	–0.0022
0 ₀	–	1 ₀	24490.7585	–0.0082
4 ₁	–	5 ₁	24489.5104	–0.0073
6 ₀	–	7 ₀	24488.7326	0.0274
6 ₁	–	7 ₁	24488.7853	0.0237
7 ₀	–	8 ₀	24488.2994	–0.0019
7 ₁	–	8 ₁	24488.3504	–0.0073
8 ₀	–	9 ₀	24487.8711	–0.0091
8 ₁	–	9 ₁	24487.9269	–0.0097
9 ₀	–	10 ₀	24487.4411	–0.0008
9 ₁	–	10 ₁	24487.4944	–0.0039

Table 2. Molecular constants of CCCCH_3^+ (cm^{-1}).^a

B''	0.14165(44)
ΔA	0.0478(105)
ΔB	–0.00861(55)
ν	24491.0500(108)
rms	0.0115

^aValue in parentheses is the standard 2σ deviation. Uncertainty of the calibration is 0.02 cm^{-1} .

The carrier of the new band must be either a symmetric top hydrocarbon molecule produced in the discharge, or a hydrocarbon complexed with Ar. Observation of some of the same strong bands when using He as the buffer gas excludes the latter.

In view of the determined rotational constant, hydrocarbon molecules containing only four carbons, such as C_4H_4 , C_4H_3 , C_4H_2 , and their ions are possible carriers. Among these, H_2CCCCH_2 , HCCCCH_3 , HCCCCH_2 , CCCCH_3 , and CCCCH_2 are symmetric or near-symmetric top molecules. On the basis of the information from previous theoretical studies on these species [14–16], as well as the optimized structure

Table 3. Optimized geometries (in Å and degrees) for the CCCCH_3^+ for the ^3E ground electronic state using DFT theory at B3LYP/cc-pVTZ level.

	cc-pVTZ
$r_{\text{C}_1\text{C}_2}$	1.410
$r_{\text{C}_2\text{C}_3}$	1.267
$r_{\text{C}_3\text{C}_4}$	1.261
$r_{\text{C}_1\text{H}_{1,2,3}}$	1.099
$\angle \text{C}_2\text{C}_1\text{H}_{1,2,3}$	110.3
$\angle \text{H}_1\text{C}_1\text{H}_{2,3}$	108.7
$\angle \text{H}_2\text{C}_1\text{H}_3$	108.7

calculated by DFT theory, only HCCCCH_2 and CCCCH_3 are compatible with the obtained rotational constants. Although the rotational constants of HCCCCH_2 and HCCCCH_2^+ calculated from the predicted geometry are reasonable ($B \sim 0.137 \text{ cm}^{-1}$ and $C \sim 0.135 \text{ cm}^{-1}$ for neutral, $B \sim 0.139 \text{ cm}^{-1}$ and $C \sim 0.137 \text{ cm}^{-1}$ for cation), the slight difference between them ($B-C = 0.002 \text{ cm}^{-1}$) would result in non-negligible $K_a = 1$ asymmetric splittings. This is not seen in the spectrum (figure 1). On the other hand, CCCCH_3 is a symmetric-top molecule, suggesting this molecule to be a good candidate for the observed absorption spectrum.

In order to help the assignment, *ab initio* calculations for neutral CCCCH_3 and its cation have been carried out with DFT and TD-DFT theory using the Gaussian program [17]. Geometry optimization for the neutral CCCCH_3 doublet state [14] and the cation singlet [15] have been reported. DFT gives $B \sim 0.136 \text{ cm}^{-1}$ in the ground state for the CCCCH_3 structure, which is outside the error limit of the rotational constant inferred from the analysis of the spectrum (table 2). In the case of CCCCH_3^+ , the rotational constant in the ground state is predicted to be 0.140 cm^{-1} , in agreement with the experimental result.

To obtain the symmetry of the electronic transition, TD-DFT calculations for CCCCH_3^+ in both singlet and triplet ground states have been carried out. For the singlet states vertical transitions to the first four excited electronic states have no parallel electric dipole moment and have excessive transition energies. On the other hand, the triplet state of CCCCH_3^+ gives rise to a parallel electronic transition from the ground to the fourth excited state at around 414 nm, the region where the molecular band is observed. Tables 3 and 4 list the optimized geometries, rotational constants, vertical transition energy, and the oscillator strength of CCCCH_3^+ calculated at the B3LYP/cc-pVTZ level.

Thus, the observed absorption system can be assigned to CCCCH_3^+ in the triplet ground state. The rotational

Table 4. Rotational constants in the 3E ground state, vertical transition energy and oscillator strength for the observed parallel electronic transition of $CCCCH_3^+$ using DFT and TD-DFT theories at B3LYP/cc-pVTZ level.

	cc-pVTZ
A/cm^{-1}	5.245
B/cm^{-1}	0.140
${}^3E \leftarrow X^3E/eV$	2.989
$f_4 \leftarrow x$	$f \approx 3 \times 10^{-4}$

analysis indicates $CCCCH_3^+$ is prolate symmetric and its symmetry is considered as C_{3v} . This ion possesses three identical atoms of nuclear spin- $1/2$ off the main axis, so that the total eigenfunction is either A or E symmetry. Because most of the lines originate from $K < 2$ at the low experimental temperature of 20 K, and the K doubling is not resolved as is usually the case, the expected intensity distribution of the spectrum was calculated by taking into account the statistical weight for C_{3v} symmetry described in the table 3.11 of [18] (i.e. $K=0$ and $K=1$ each having a statistical weight of 4, $4A_1$ (J even) or $4A_2$ (J odd) in the $K=0$ level and $2A_1 + 2A_2$ in the $K=1$ level), which agrees well with the observed result (figure 1).

The lines in the 408 nm region detected in both the pulsed- and cw-CRD spectra match within the frequency accuracy ($\sim 0.07 \text{ cm}^{-1}$) common to both experimental set-ups. Ten P-branch lines ($N=5-6$ to $9-10$) observed with the cw CRD spectrometer clearly match the five lines observed previously as listed in [12]. Each of these peaks appears to split into two when scanned with higher resolution. The doublets clearly indicate that these lines observed at lower resolution cannot be due to the allyl radical as previously assigned; the unresolved lines are actually due to $CCCCH_3^+$. However, one can be sure some of the other absorptions also observed in [12] are due to the allyl radical because of the vibrational assignments and the shifts observed upon deuteration.

3.2. Re-analysis of the rotational structure of allyl radical

The previously presented assignment and derived molecular structure for allyl radical are incorrect [12]. A re-analysis is difficult due to the overlap with the rotational lines from $CCCCH_3^+$. An R-branch of the spectrum of C_3D_5 in the $\tilde{A}^2B_1 \cdot \tilde{X}^2A_2$ electronic transition can be analysed more easily because in the 24552 cm^{-1} region there is no significant overlap with lines from other species. However, because the rotational structure of the R-branch is not well resolved, a least-square fitting procedure called ‘total spectrum

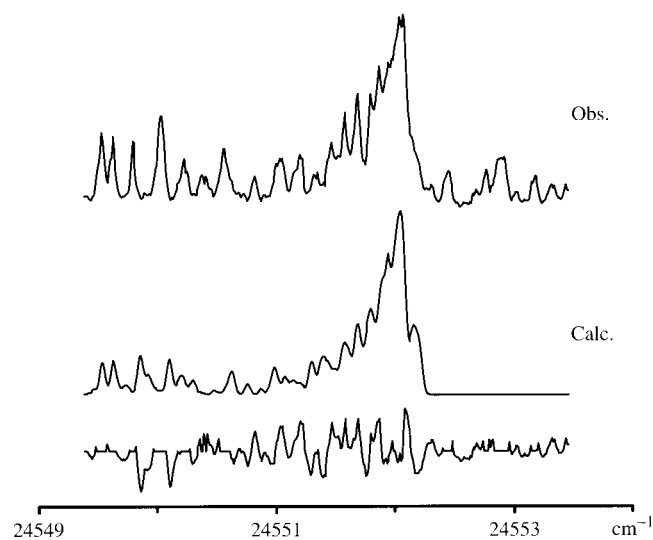


Figure 2. Electronic absorption spectrum, $\tilde{A}^2B_1 \cdot \tilde{X}^2A_2$, of the origin band of C_3D_5 (upper trace) measured by pulsed CRD spectroscopy through a pulsed slit nozzle discharge reported in [12]. The simulated spectrum by the total spectrum fitting (TSF) method is shown in the middle. The lower plot represents the difference between the upper and middle traces.

fitting’ (TSF) was used to obtain the molecular constants [19]. The TSF method compares the observed and simulated rotational profiles. In this procedure it is assumed that a spectrum of an asymmetric top molecule is characterized only by the following parameters: rotational constants A, B, C in both states, transition frequency, temperature, spin statistical weights, a FWHM of Gaussian line shape, an amplitude and base line bias (the slope was corrected before the analysis).

Lines through $J=50$ were included in the simulations, which is sufficient for the jet cooled spectrum of C_3D_5 . Absorption lines apparent in the recording (upper trace in figure 2), except for the R-branch ones, were treated with zero-weight. The FWHM of Gaussian line shape was assumed to be 0.05 cm^{-1} due to Doppler broadening.

The ground state rotational constants of C_3D_5 were fixed using the molecular structure of C_3H_5 determined by infrared spectroscopy [20]. The ratio of B and C in the excited state was also held constant. A temperature of 25 K was used for C_3D_5 , which gave a minimal rms. The rotational profile was well reproduced (middle trace in figure 2), and the molecular constants determined in the excited state are listed in table 5. Based on the reproduced spectrum of C_3D_5 and the band head position of C_3H_5 in figure 1 and 2 in [12], the band origin of C_3H_5 is evaluated to be $T_{00} = 24492.1 \text{ cm}^{-1}$.

Table 5. Molecular constants of C_3D_5 obtained by the TSF method (cm^{-1}).

	This work	Infrared ^a	<i>Ab initio</i> ^b	
			C_{2v}	C_2
A''	1.1012 ^c	1.1012	1.1182	
$\frac{1}{2}(B''+C'')$	0.2473 ^c	0.2473	0.2475	
ΔA	-0.04187(4) ^d		-0.0558	-0.1504 ^f
$\Delta \frac{1}{2}(B+C)$	-0.029366(12) ^{d,e}		-0.0193	-0.0108 ^f
T_{00}	24550.3238(6) ^{d,g}			

^aValues estimated from the molecular structure of C_3H_5 [20].

^bCASSCF/TZV(d,p) in [21].

^cFixed.

^dValues in parentheses denote the standard 2σ deviation.

^eTo calculate molecular structure of C_3D_5 , separate values of B' and C' (0.241965 and 0.193843 cm^{-1}) were used.

^fDifferences between the ground C_{2v} and excited C_2 states.

^gThe error is from the least-squares fitting. Uncertainty of the calibration is 0.05 cm^{-1} .

The rotational constants obtained still support the conclusion that the allyl radical has a planar C_{2v} structure in the zero-point level of the excited state because the determined ΔA and $\Delta \frac{1}{2}(B+C)$ constants are closer to those predicted by *ab initio* calculations for C_{2v} rather than C_2 symmetry (table 5). The obtained values were used to re-evaluate the C–C distance and CCC angle in the excited state of the allyl radical. Five structural parameters involving hydrogens were fixed to the *ab initio* values [21] in C_{2v} symmetry, $r(\text{C}_1\text{D}_1) = 1.072 \text{ \AA}$, $r(\text{C}_2\text{D}_2) = 1.073 \text{ \AA}$, $r(\text{C}_2\text{D}_3) = 1.071 \text{ \AA}$, $\theta(\text{D}_2\text{C}_2\text{C}_1) = 120.4^\circ$, and $\theta(\text{D}_3\text{C}_2\text{C}_1) = 120.8^\circ$. This leads to $r(\text{C}_1\text{C}_2) = 1.4985 \pm 0.0064 \text{ \AA}$ and $\theta(\text{C}_2\text{C}_1\text{C}_3) = 124.51 \pm 0.31^\circ$. Errors are derived from an inertial defect.

4. Conclusions

The electronic spectrum of the hydrocarbon cation CCCCCH_3^+ has been detected in the 408 nm region for the first time. The assignment is based on the inferred rotational constants, *ab initio* calculation of the geometry, and the excitation energy calculated with DFT and TD-DFT theories. It is not clear whether the observed electronic band is the origin because of the limited scanning range of the cw CRD set-up.

The present results show that the P-branch lines which were previously assigned to the allyl radical (C_3H_5) [12], are actually rotational transitions from CCCCCH_3^+ . The new assignment for deuterated allyl radical leads to the rotational constants $\Delta A = -0.04187(4) \text{ cm}^{-1}$, $\Delta \frac{1}{2}(B+C) = -0.029366(12) \text{ cm}^{-1}$, and the transition frequency $T_{00} = 24550.3238(6) \text{ cm}^{-1}$. Although both

CCCCCH_3^+ and the allyl radical are produced in the pulsed CRD set-up, only CCCCCH_3^+ is observed using the cw CRD spectrometer. This may be because the discharge source used in the two instruments run under different experimental conditions, particularly with respect to density, leading to production of species with different rotational temperatures.

The obtained rotational constants may be useful for the measurement of a pure-rotational spectrum of this cation in the radio frequency region in the laboratory and by radio astronomy.

Acknowledgements

This work has been supported by the Swiss National Science Foundation (project 200020-107386) and is part of the European Union project ‘Molecular Universe’ (MRTN-CT-2004-512302).

References

- [1] T. Henning and F. Salama, *Science* **282**, 2204 (1998).
- [2] H. Richter and J. B. Howard, *Prog. Energy Comb. Sci.* **26**, 565 (2000).
- [3] T. Fujii and M. Kareev, *J. Apl. Phys.* **89**, 2543 (2001).
- [4] J. P. Maier, *J. Phys. Chem. A* **102**, 3462 (1998).
- [5] T. Motylewski, H. Linnartz, O. Vaizert, J. P. Maier, G. A. Galazutdinov, F. A. Musaev, J. Krelowski, G. A. H. Walker, and D. A. Bohlender, *Astrophys. J.* **531**, 312 (2000).
- [6] A. O’Keefe and D. A. G. Deacon, *Rev. Sci. Instrum.* **59**, 2544 (1988).
- [7] G. Berden, R. Peeters, and G. Meijer, *Int. Rev. Phys. Chem.* **19**, 567 (2000).

- [8] P. Birza, T. Motylewski, D. Khoroshev, A. Chirokolava, H. Linnartz, and J. P. Maier, *Chem. Phys.* **283**, 119 (2002).
- [9] D. Khoroshev, M. Araki, P. Kolek, P. Birza, A. Chirokolava, and J. P. Maier, *J. Mol. Spectrosc.* **227**, 81 (2004).
- [10] P. Birza, A. Chirokolava, M. Araki, P. Kolek, and J. P. Maier, *J. Mol. Spectrosc.* **229**, 276 (2005).
- [11] M. Hipper and M. Quack, *Chem. Phys. Lett.* **314**, 273 (1999).
- [12] E. Achkasova, M. Araki, A. Denisov, and J. P. Maier, *Mol. Phys.* **103**, 1555 (2005).
- [13] D. Luckhaus and M. Quack, *Mol. Phys.* **63**, 745 (1989).
- [14] T. N. Le, A. M. Mebel, and R. I. Kaiser, *J. Comput. Chem.* **22**, 1522 (2001).
- [15] D. Schroder, J. Loos, H. Schwarz, R. Thissen, J. Roithova, and Z. Herman, *Int. J. Mass Spectrom.* **230**, 113 (2003).
- [16] R. I. Kaser, A. M. Mebel, Y. T. Lee, and A. H. H. Chang, *J. Chem. Phys.* **115**, 5117 (2001).
- [17] M. J. Frisch *et al.*, 2003, Gaussian, Inc., Pittsburgh, PA: see www.gaussian.com.
- [18] H. W. Kroto, *Molecular Rotation Spectra* (Dover Publications Inc., New York, 1992).
- [19] M. Araki, T. Motylewski, P. Kolek, and J. P. Maier, *Phys. Chem. Chem. Phys.* **7**, 2138 (2005).
- [20] E. Hirota, C. Yamada, and M. Okunishi, *J. Chem. Phys.* **97**, 2963 (1992).
- [21] K. Tonokura and M. Koshi, *J. Phys. Chem. A* **104**, 8456 (2000).

3.1 Principle

In a more general sense, pulsed amplification belongs to the category of optical amplifiers. In principle, any laser active gain medium can be pumped in order to produce a population inversion, resulting in stimulated emission of the incoming seed radiation. This gives rise to the amplification of radiation. By choosing the material of the medium appropriately, it is possible to produce laser radiation on a broad range of frequencies. Such amplifiers are used to build high power laser systems. Some types, such as the regenerative, optical parametric and chirped-pulse amplifiers [1], are used to amplify ultrashort pulses [2, 3]. Amplified pulses, among many other applications, are required for non-linear processes, frequency upconversion being one such example. In addition, a laser with narrow bandwidth has always been the preferred choice to carry out e.g. high resolution experiments. By its very definition, high-resolution laser spectroscopy requires narrow linewidth light sources. The laser linewidth should be limited to at most a few hundred MHz to resolve the typical electronic transition lines of gaseous molecules. The motivation, therefore, behind building a pulsed amplification system is to produce Fourier-Transform (FT)-limited high energetic pulses.

One of the methods of producing near FT-limited pulses is based on the pulsed dye amplification (PDA). A single-mode cw ring laser beam is amplified with the dyes as the gain medium [4, 5]. The fluorescence lifetimes of typical dyes are short, normally, on the order of 100's of picoseconds. This leads to the amplified radiation pulses to have the same temporal profile as the pump laser. Figure 3.1(a) illustrates the process. The band-

width of the pulse, therefore, cannot be controlled and set according to the requirements, which imposes certain limits on its application. There are some other disadvantages as well, such as, scanning the frequency over large range needs frequent changes of dyes; frequency chirps are often observed in the amplified pulses, arising from time-dependent changes of the refractive index of the dye induced by the pump pulses [6, 7].

There is another method based on solid-state laser technology reported by [8] which does not have such disadvantages. The bandwidth and the shape of the pulse can be controlled. The frequency chirps are inherently low and the temporal length of the pulses can be varied in the range from ns to μ s. The system generates intense pulses of narrow-band near-FT-limited radiation. In this method, the optical amplification is achieved inside insulating crystals and glasses doped with active ions. In the current work, Ti:Sapphire (Ti:Sa) has been used as the amplifying medium. Figure 3.1(b) describes the behaviour of the signal before and after the amplification. The lowest row in the figure shows that generating pulses prior to the amplification can lead to the generation of intense pulses of adjustable length and shape if a multipass amplification setup is used. More details can be found in [8].

3.1.1 Gain medium and the energy levels structure

Ti:Sa ($\text{Ti}^{3+}:\text{Al}_2\text{O}_3$) is a well-known material extensively used as a laser gain medium to produce ultrashort laser pulses in addition to generate narrow bandwidth radiation [9, 10, 11]. It emits over a frequency range from 680-1025 nm.

Some of the impurity ions i.e. Ti^{3+} , which are also the laser active ions, substitute the Al^{3+} ions in the sample. The Al^{3+} lattice symmetry is trigonal but the six neighboring O^{2-} ions surrounding the Al site lie at the corners of a slightly distorted octahedron. So, the crystalline field experienced by Ti^{3+} is largely cubic with a small trigonal component. For the substituted d^1 ion, this crystalline field splits the degenerate free-ion energy level of the d electron (from Ti^{3+} ion) into upper level with 2E_g and lower ${}^2A_{1g}$ and 2E_g symmetries (Figure 3.2). The lower 2E_g level is split by the spin-orbit coupling. The upper 2E_g level exhibits a Jahn-Teller effect [12, 13]. The amplification occurs as a result of the

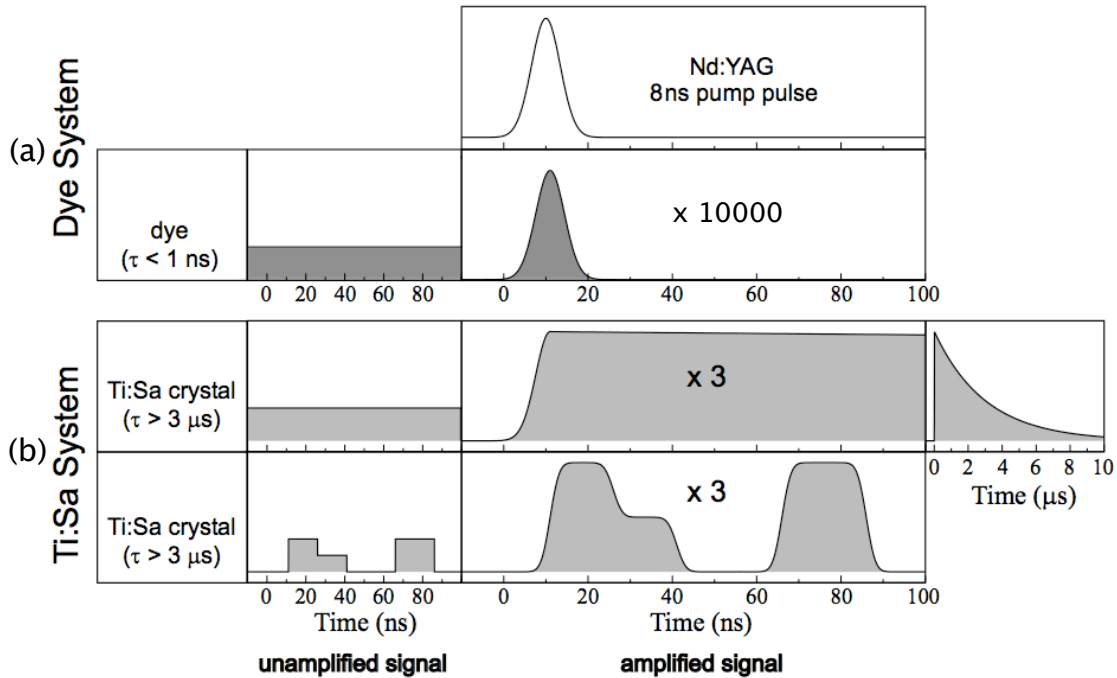


Figure 3.1: Comparison of the pulse generation and pulse amplification by dye cells and Ti:Sapphire crystals. Reproduced from [8].

transitions (by stimulated emission) from the excited 2E_g state to the vibronic manifolds of the ${}^2T_{2g}$ ground state of d electrons [14]. Because the laser active ion is not shielded from the surrounding lattice, strong electron-phonon coupling takes place, giving rise to broadly tunable output. Electron-phonon coupling is schematically shown by using the well-known ‘configuration-coordinate’ diagrams. An example of a single configuration-coordinate diagram of an ion coupled to a vibrating lattice is shown in Figure 3.3. The configuration coordinate Q in this case refers to the distance between the central active ion and the neighboring ion. The equilibrium distance is Q_{01} when the electronic eigenenergy of the static lattice is E_{e1} . Upon excitation to the excited electronic state with static eigenenergy E_{e2} , a new equilibrium position at $Q = Q_{02}$ results.

Next, let us consider an ion in the ground state $|g\rangle$. Upon absorption of a photon at the pump wavelength of λ_p (lower than the seed beam wavelength, λ_L), it can be promoted to one of the excited vibronic states shown in Figure 3.4. In this particular case, the terminal state is designated as $|3\rangle$. Once in the excited state, the ion rapidly decays to the lowest vi-

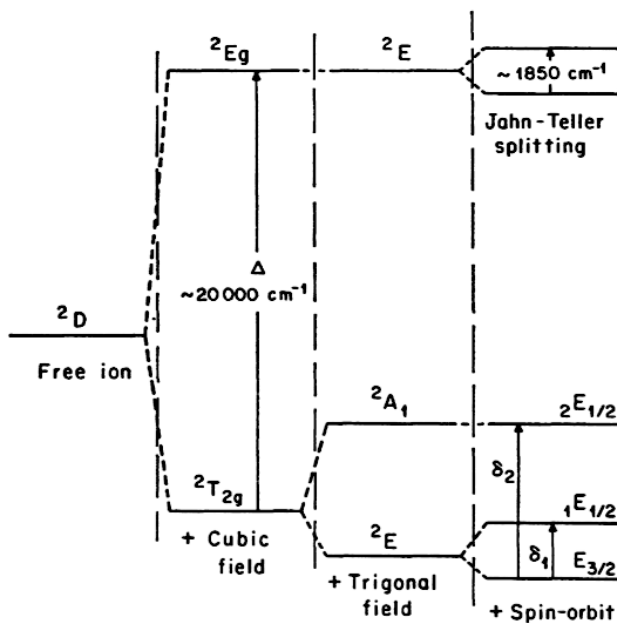


Figure 3.2: The energy level structure of $T^{3+}:Al_2O_3$.

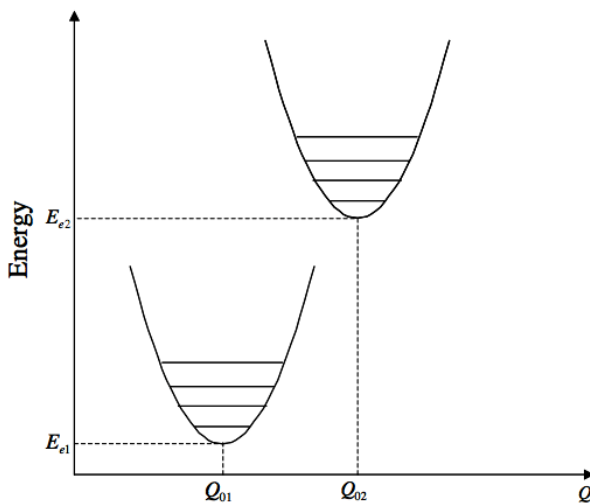


Figure 3.3: Single configuration coordinate diagram of a transition metal ion coupled to a vibrating lattice.

bronic level (shown as $|2\rangle$ in Figure 3.4) of the excited state by emitting phonons. Since no light is produced during such a transition, this is also referred to as a non-radiative decay.

The state $|2\rangle$ is the upper laser level. From here, the ion can decay to lower states either by spontaneous emission (radiative or non-radiative) or stimulated emission. Stimulated emission occurring as the ion makes a transition from $|2\rangle$ to $|1\rangle$ gives rise to the optical gain at λ_L . Once in the lower laser level $|1\rangle$, the ion undergoes another rapid non-radiative decay to the ground state $|g\rangle$. This sequence of transitions is also shown in Figure 3.4 where non-radiative decays are indicated by dotted arrows. Typically, the non-radiative transitions occur at much faster rates. Hence, ions excited to state $|3\rangle$ rapidly populate the upper laser level $|2\rangle$ and the population of the lower laser level $|1\rangle$ is negligible. In other words, the vibronic system behaves to a very good approximation like a 4-level system and lasing can therefore be obtained at reasonably low pumping levels [15]. The spontaneous emission and non-radiative processes interfere with the stimulated emission and reduce the efficiency of light amplification. The single configuration-coordinate diagram that is used above to describe phonon coupling provides a rather simplified picture of the ion-lattice interaction. In reality, the lattice vibrations consist of a large number of modes with different phonon frequencies [16]. As a result, the sharp transitions indicated in Figure 3.4 are due to the presence of a single phonon frequency get smeared out into broad absorption and emission bands. The tunable laser amplification in the crystal is based on the vibronically broadened 2E_g - ${}^2T_{2g}$ transition of the Ti^{3+} ion. Although the electronic transitions of an isolated ion are very well defined, broadening of the energy levels occurs when the ions are incorporated into the sapphire crystal host and thus the amplification window is also broadened. This broadening is both homogeneous (all ions exhibit the same broadened spectrum) and inhomogeneous (different ions in different host locations exhibit different spectra). Homogeneous broadening arises from the interactions with phonons while inhomogeneous broadening is caused by differences in the sapphire sites where different ions are hosted. Different sites expose ions to different local electric fields, which shifts the energy levels via the Stark effect.

These broadband absorption and emission are polarized with respect to the c-axis of the sapphire host, with maximum transition moments occurring for electric field polarizations parallel to the c-axis (π polarization) [17]. Figure 3.5 illustrates the difference in ab-

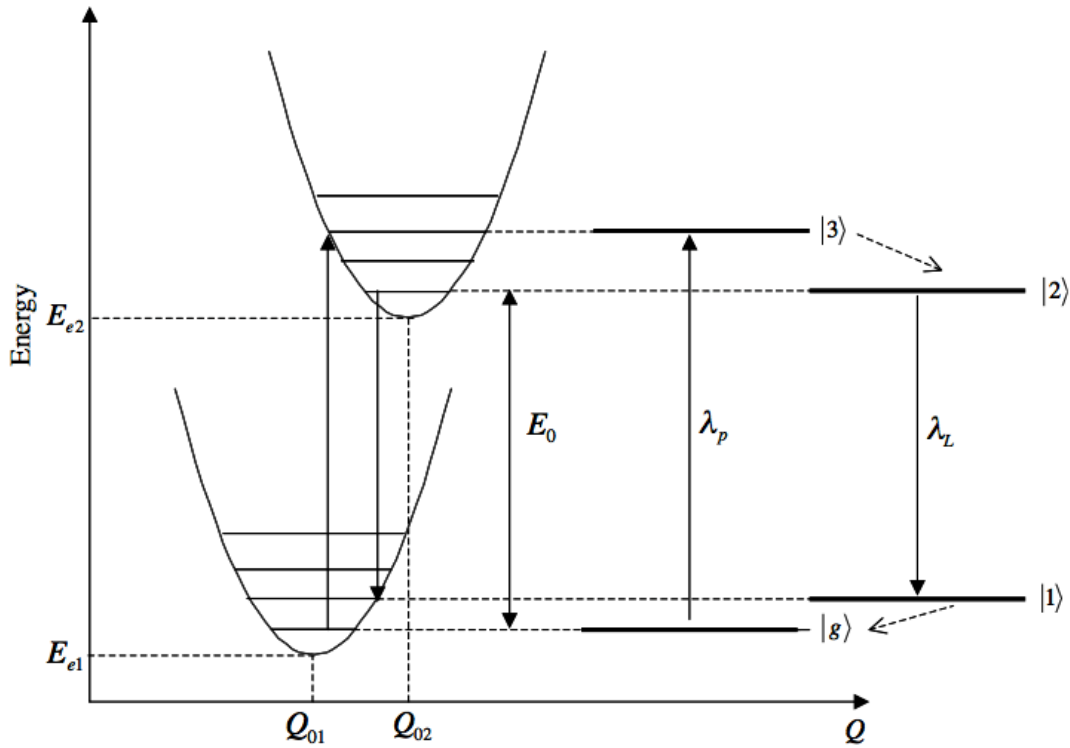


Figure 3.4: Sequence of transitions for an ion coupled to a vibrating lattice, forming a 4-level energy diagram.

sorption for the two polarizations. The fundamental ground state absorption of $\text{Ti}^{3+}:\text{Al}_2\text{O}_3$ extends from 400 to 650 nm. Stokes-shifted emission originating from the ${}^2\text{E}_g$ upper laser level covers the wavelength region from 600 to 1200 nm. The peak emission cross section and upper state fluorescence lifetime at room temperature of Ti:Sa are $\sigma_e = 3 \times 10^{-19} \text{ cm}^2$ [19] and $\tau = 3.15 \mu\text{s}$ [18, 20]. The long fluorescence time induces a slow exponential decay of the population inversion, which is an essential property for the amplification of long pulses. This implies that,

- the pulse amplification can be extended beyond the duration of the pump pulse ($\sim 10 \text{ ns}$).
- the seed pulse shape is preserved during the amplification. Hence, the temporal

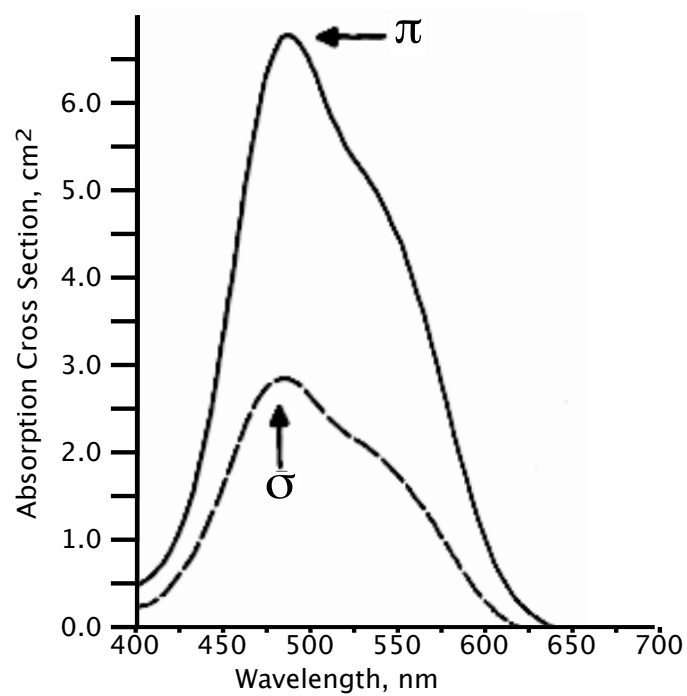


Figure 3.5: The π - and σ -polarized absorption cross section of the ${}^2T_{2g} \rightarrow {}^2E_g$ transition in Ti:Sa. Reproduced from [18].

profile of the pulses needs to be defined before the pulse amplification.

- the pulses generated from a cw source do not have the same shape as the pump pulses.

- the gain coefficient [21] and the amplification factor is reduced by more than two orders of magnitude (in comparison to the PDA cells), which leads to smaller frequency chirps but requires a multipass amplification arrangement through the Ti:Sa crystal. This multipass can be achieved by either having an active cavity (2 or 3 mirrors) or by positioning mirrors in the light-path. The latter method is opted within the setup presented in this work.

3.1.2 Amplification

Efficient lasing/amplification operation requires sufficiently high intensity within the gain medium to maximize the stimulated emission processes [22]. The ratio of the stimulated to spontaneous emission rate from the upper laser level is given by the quantity I/I_{sat} , where I is the intensity of the seed beam inside the gain medium and I_{sat} is the saturation intensity of the corresponding transition. The saturation intensity is given by the expression, $I_{sat} = h\nu/\sigma_e\tau$, where $h\nu$ is the laser photon energy [23]. For the $Ti^{3+}:Al_2O_3$ transition (at the peak emission wavelength of 800 nm), the calculated saturation intensity is $2.63 \times 10^5 \text{ Wcm}^{-2}$. The high I_{sat} value of $Ti^{3+}:Al_2O_3$ necessitates tight focusing within the gain medium, especially at low pump power levels, to effectively saturate the population inversion. Ti:Sa is a relatively low-gain medium, with a low-threshold [11]. It has a lasing threshold of 0.8 W ($= 5.6 \times 10^{-6}$ mJ for 7 ns pulses). Because of steep rise in gain of Nd^{3+} :YAG pumped Ti:Sa, pulse shaping can easily occur when the intensity of the evolving pulse is larger than the saturation level and when the pulse rises steeply from an exponential or hard truncated leading edge. The crystal (Figure 3.6) can be efficiently pumped with a laser at a wavelength of 532 nm and exhibits gain in the same region as the seed beam. The main absorption feature, a broad double hump band peaking near 500 nm [24], corresponds to the fundamental ground state absorption of the Ti^{3+} ion. A few important parameters of the crystal are,

- An absorption figure of merit (FOM), defined as the ratio of the absorption coefficients at the pump and emission wavelengths is referred to assess the quality of $Ti^{3+}:Al_2O_3$ crystalline material [25, 26]. The FOM of the crystal used in the current

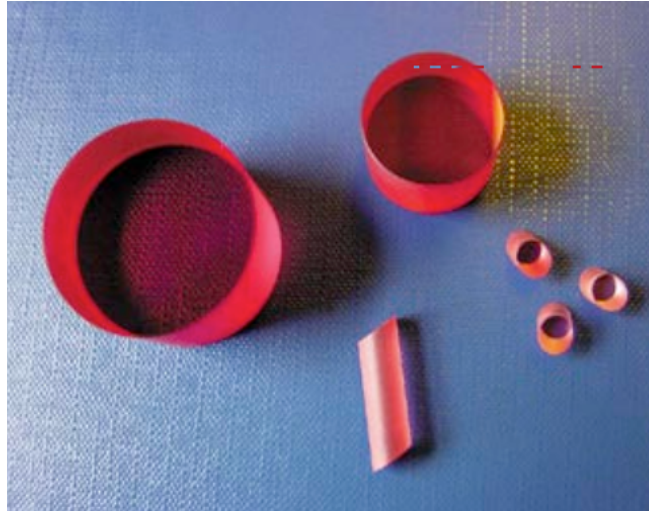


Figure 3.6: *Titanium-doped sapphire crystals has broadest lasing range.*

work is > 150 .

- If pumped at 532 nm, the uncertainty of the Ti:Sa damage threshold, is about a factor of ten [27]. The empirically estimated threshold is 10 Jcm^{-2} but for safety reasons the laser community (especially the companies producing the lasers) uses the conservative value of 1 Jcm^{-2} .
- One should consider the localized heating effects in the crystal because this influences the behaviour of the crystal. The linearity of the output power begins to deviate beyond a certain level of input pump power [28]. An approximate analytical solution of the temperature profile in the crystal is obtained by solving a steady-state heat equation, assuming only radial heat transfer from the optically pumped region [29]. Solutions of this equation predict a logarithmic radial temperature distribution which exponentially decays along the length of the crystal (Figure 3.7). For this calculation, uniform pumping into a circular region of 1mm radius at the center of the crystal is assumed. The temperature rise in the pumped region increases the rate of non-radiative decay from the upper laser level, effectively decreasing the fluorescence lifetime and quantum efficiency by approximately 10%. The thermo-optical aberrations due to temperature gradients in the crystal also limit the output

power [30].

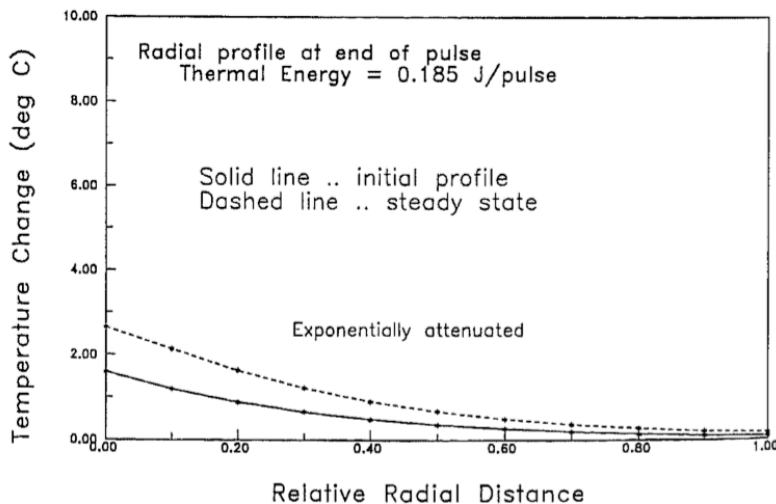


Figure 3.7: Quasi-steady-state temperature along the axis of the Ti:Sa rod. Reproduced from [28].

3.1.3 Overview of the setup

As shown in Figure 3.8, the working of the setup can be described in short as follows. The continuous wave (cw) output of a ring Ti:Sa laser is passed through an acousto-optic modulator (AOM) to generate seed pulses. The seed beam and a pump laser are combined into the Ti:Sa crystal located in the “amplification stages 1 and 2” (refer to Figure 3.8). The beam is then amplified by a factor of 10^6 to 10^7 in a multipass arrangement through the crystals (Amplification stage block in the Figure 3.8). The beam is amplified through interaction with the doping ions (Ti^{3+}). The peak powers attained are high enough for efficient frequency upconversion in nonlinear crystals such as LBO, BBO, KNbO_3 , etc. This is required to extend the spectral range of Ti:Sa lasers to the blue and ultraviolet regions. Therefore, the amplified beam is passed through the frequency doubler. The doubled beam is then sent to the experimental cavity to perform high resolution spectroscopy.

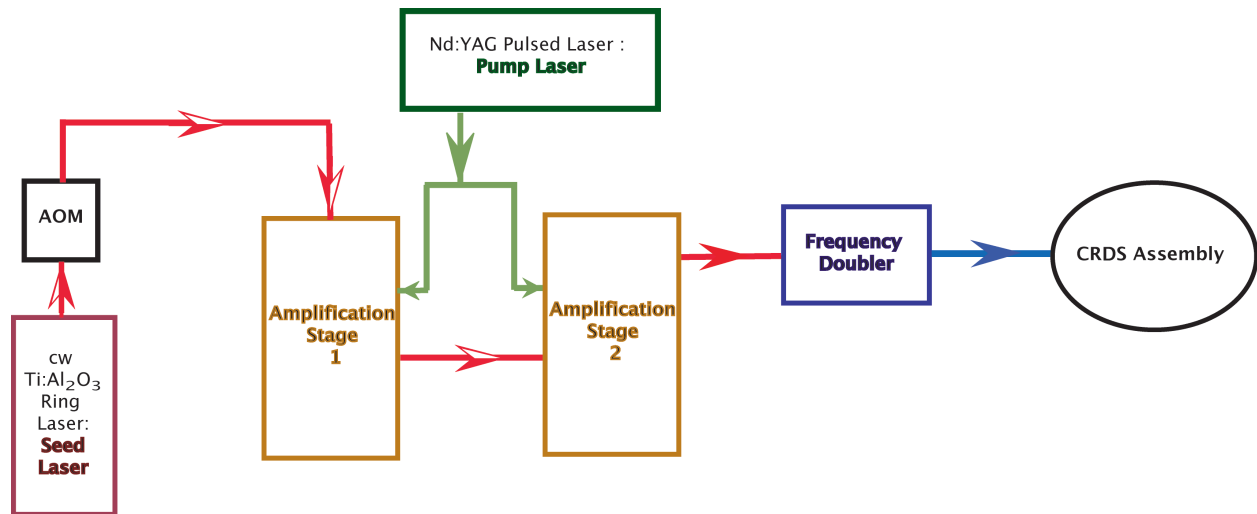


Figure 3.8: The block diagram of the setup used for amplification.

3.1.4 Advantages

The advantage of cw ring laser with pulsed amplifiers over that of pulsed laser is that,

- the pulses are Fourier limited,
- generates intense pulses throughout a broad range of 720 to 1060 nm, where an intense pump source such as Nd³⁺:YAG is also available,
- can also generate pulses of a few micro joules for wavelengths down to the blue region of visible range, near UV, etc. by nonlinear crystals.

3.1.5 Limitations

- The principal source of noise is amplified spontaneous emission (ASE). This has a spectrum approximately the same as the gain spectrum of the amplifier. In addition to the stimulated emission, electrons in the upper energy level can also decay by spontaneous emission. This occurs at random, depending upon the host characteristics and the inversion level. Photons are emitted spontaneously in all directions. Some of these photons are captured and may then interact with other dopant ions. Thus, these are amplified by stimulated emission. The initial spontaneous emission

is therefore amplified in the same manner as the seed beam, hence the term amplified spontaneous emission. Figure 3.9 explains the process. ASE is emitted by the amplifier in both the forward and reverse directions. The forward ASE will co-propagate with the desired beam to the receiving end where it degrades the system performance. Counter-propagating ASE can lead to degradation of the efficiency of the crystal since the ASE can deplete the inversion level and thereby reduce the gain of the amplifier. Backward ASE can be detrimental to the optical unit/laser placed right before, as it can cross the damage threshold of the corresponding unit due to high power. Besides, it can interfere with the incoming beam which will cause fluctuations. Further details on ASE can be found in [31].

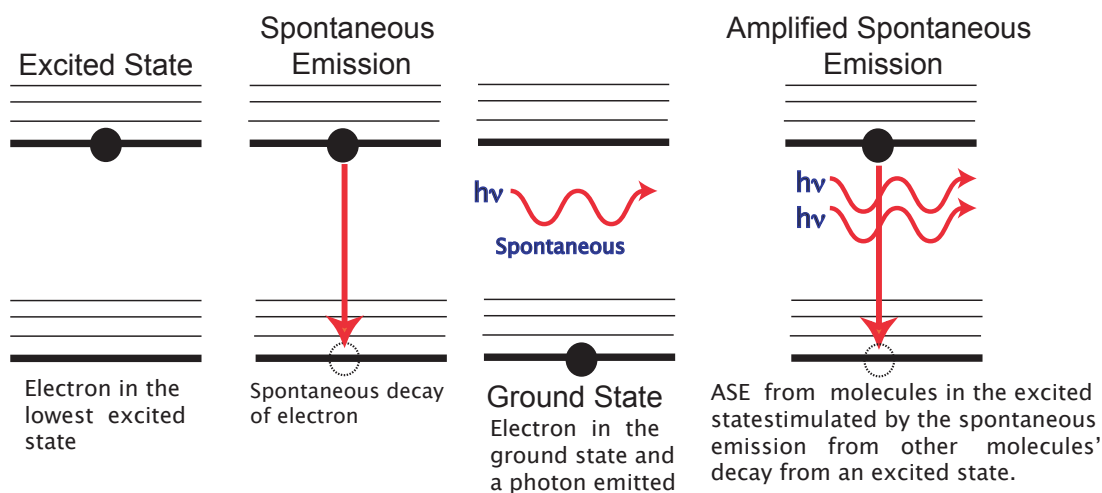


Figure 3.9: The origin of ASE which is broadband and incoherent in nature, as opposed to the desired amplified radiation of the seed beam. Spontaneous emission will create coherent stimulated emission along its direction of propagation which is termed as ASE. The ASE wavelength will be centered around the part of the uorescence with the highest gain.

- Gain is achieved in an amplifier due to the population inversion of the dopant ions. The inversion level of the crystal depends on the power of the pump wavelength and the power at the amplified wavelengths. As the seed beam power increases,

or the pump power decreases, the inversion level will reduce and thereby the gain of the amplifier will be reduced. This effect is known as gain saturation - as the signal level increases, the amplifier saturates and cannot produce any more output power, and therefore the gain reduces. Saturation is also commonly known as gain compression.

To achieve optimum noise performance, the amplifiers are operated under a significant amount of gain compression (10 dB typically), since this reduces the rate of spontaneous emission, thereby reducing ASE. Another advantage of operating in the gain saturation region is that small fluctuations in the input signal power are reduced in the output amplified signal: smaller input signal powers experience larger (less saturated) gain, while larger input powers see less gain.

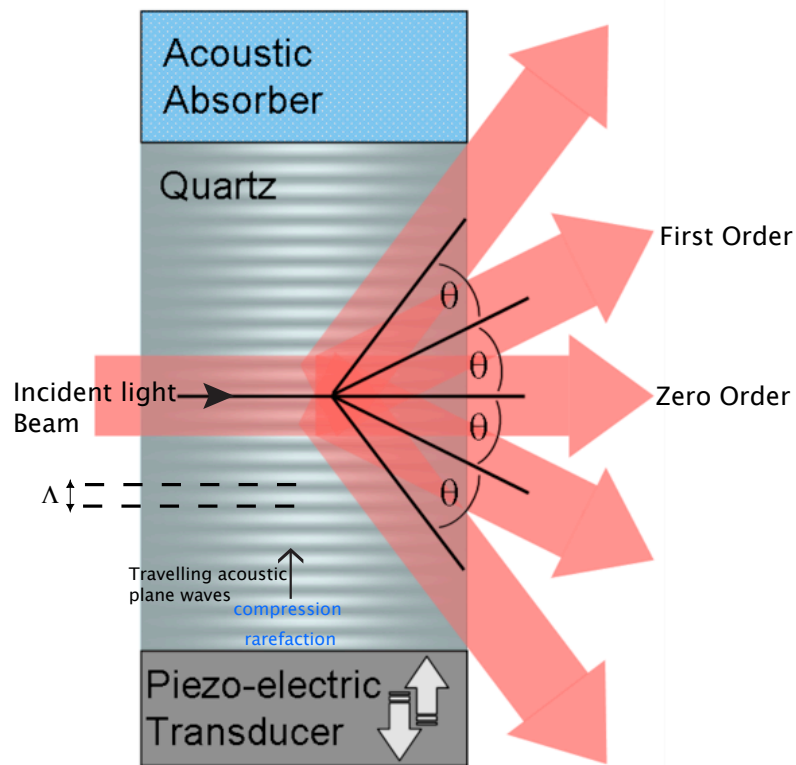
- **Inhomogeneous broadening effects** Due to the inhomogeneous portion of the linewidth broadening of the dopant ions, the gain spectrum has an inhomogeneous component and gain saturation occurs, to a small extent, in an inhomogeneous manner. This effect is known as spectral hole burning because a high power signal at one wavelength can 'burn' a hole in the gain for wavelengths close to that signal by saturation of the inhomogeneously broadened ions. Spectral holes vary in width depending on the characteristics of the crystal in question. The depth of the holes is very small, though, making it difficult to observe in practice.
- **Polarization effects** A small portion of the dopant ions interact preferentially with certain polarizations and a small dependence on the polarization of the input signal may occur (typically < 0.5 dB). This is called polarization dependent gain. The absorption and emission cross sections of the ions can be modeled as ellipsoids with the major axes aligned at random in all directions in different crystal sites. The random distribution of the orientation of the ellipsoids in a crystal produces a macroscopically isotropic medium, but a strong pump laser induces an anisotropic distribution by selectively exciting those ions that are more aligned with the optical field vector of the pump. Also, those excited ions aligned with the signal field produce more stimulated emission. The change in gain is thus dependent on the alignment

of the polarizations of the pump and signal lasers e.g., whether the two lasers are interacting with the same sub-set of dopant ions or not.

3.2 Setup description

The construction of a laser system consisting of a cw ring Ti:Sa laser and two stages of pulsed amplifiers has been reported. The schematic is shown later in Figure 3.14. Each stage consists of a Nd³⁺:YAG pumped Ti:Sa crystal as the gain medium to amplify the chopped cw output. This produces tunable near-FT-limited near-Infrared (NIR) radiation (principle of operation explained in [8] and references therein).

The source of NIR radiation is a single mode cw ring laser in Ti:Sa configuration (Coherent 899-29 Auotscan II). The cw laser, in turn, is pumped by 5 W (max. 10 W) of a cw diode-pumped, frequency-doubled Nd³⁺:YVO₄ laser (Coherent Verdi). 200 mW (max. 800 mW) is obtained from the laser in the visible and NIR regions. The tuning range is 720 to 1000 nm, which is covered with the help of three sets of optics: short, mid and long. The current work has been reported in the short wavelength range, i.e 720-825 nm. The cw laser is frequency stabilized to an inbuilt reference cavity. The output of a single mode cw laser with frequency ν_{cw} is chopped by an acousto-optic modulator (AOM, Isomet 1205C-2), operating at 80 MHz driving frequency. Figure 3.10 explains the function of an AOM. Figure 3.11 shows the components of the driver (Isomet model 222A-1) which work in coordination to control the AOM. The amplitude of the acoustic wave in AOM is set by the driver. A delay generator (BNC model 565 pulse/delay generator) has been used to trigger the driver at 20 Hz repetition rate. The AOM is, thus, operated in a pulsed mode. The first order diffraction beam from the AOM is used to generate seed pulses. The precise timing of the pulses triggering the AOM with respect to the Nd³⁺:YAG pulses is adjusted by this delay generator. Figure 3.12 shows the pulse sequences synchronizing different units. By carefully focussing the cw laser beam into the active volume of the AOM (active aperture diameter of ≥ 1.0 mm), pulses as short as 15 ns (full width at half maximum) can be generated from the cw output [32]. Longer pulses, multiple pulse se-



By tilting the AOM, the light can be efficiently directed into the first diffraction order.

Figure 3.10: First-order diffraction generation by acousto-optic modulation.

quences, and pulses of various shapes can also be generated, the only limitation being the minimum rise time $\sim 8 \mu\text{s}$ required for the acoustic wave to spread and reach the region of the NIR beam focus. The peak power of the pulses generated in the AOM is limited by the conversion efficiency into the first-order diffraction beam which amounts to about $\geq 60\%$ at the maximum amplitude of the acoustic waves. When generating pulses of duration $\geq 2 \mu\text{s}$, the maximum power of the diffracted beam is independent of the pulse length and can be as high as 110 mW at the exit of the AOM (with 150 mW of cw input power), as inferred from measurements made while operating the AOM in the cw mode. The pulse energies depend on the length of the pulses generated by AOM. The first-order diffraction side band of frequency $\nu_{NIR} = \nu_{cw} + 80 \text{ MHz}$ (if ν_{cw} denotes the frequency of the incident cw laser) exits the AOM, making an angle of 1.008° with the '0' order part of the cw laser beam, passes through a 2:1 beam expander. The pulse is then sent to a fiber

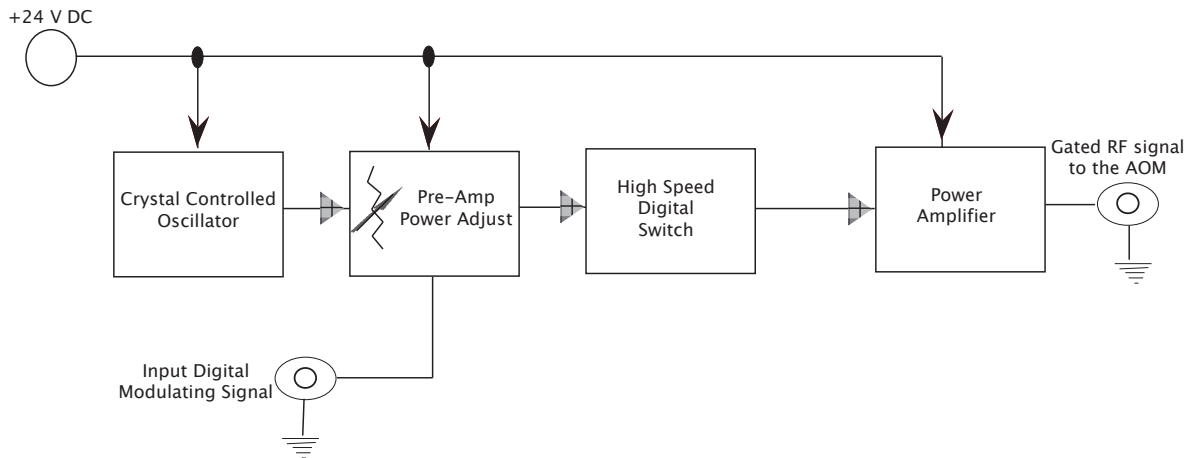


Figure 3.11: The block diagram of an AOM driver.

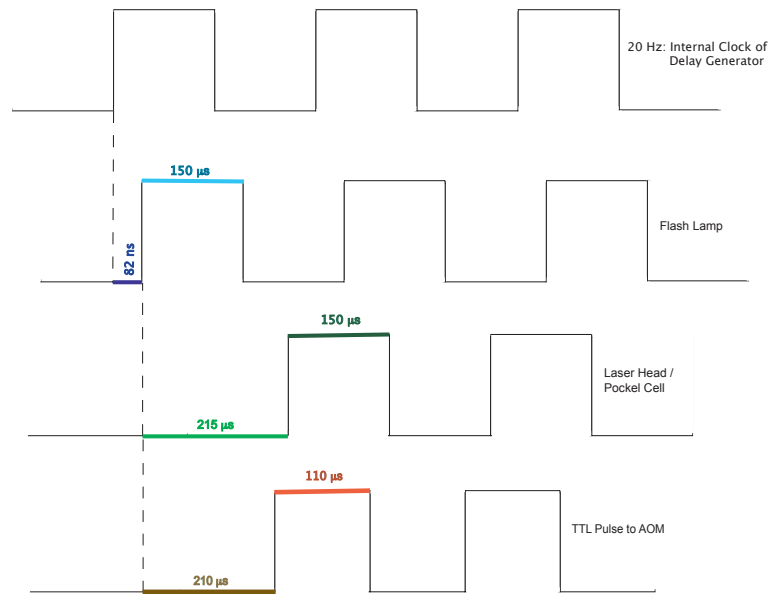


Figure 3.12: Different pulse sequences in the time domain. The flash lamp delay (82 ns in the figure), is arbitrary and the TTL pulse width (110 μs), is nominal.

launching system which consists of a microscope objective (MO) of 10X magnification and 0.25 numerical aperture (NA) on a translation stage. The MO (RMS10X, Thorlabs) couples the beam into a polarization maintaining fiber (HB750, Thorlabs). The units (MO

and the fiber) with the particular specifications have been chosen to meet the criterion of efficient coupling. The criterion is that one should use a MO (or lens) to focus the beam to a diameter (D_f), which approaches the mode field diameter (MFD) of the fiber a . The corresponding values are $\approx 1.2 \mu\text{m}$ and $4.0 \mu\text{m}$ respectively, in the present case. Figure 3.13 explains the various parameters important in considering efficient coupling and collimation of the beam traveling into and out of the fiber. A halfwave plate is used in front of

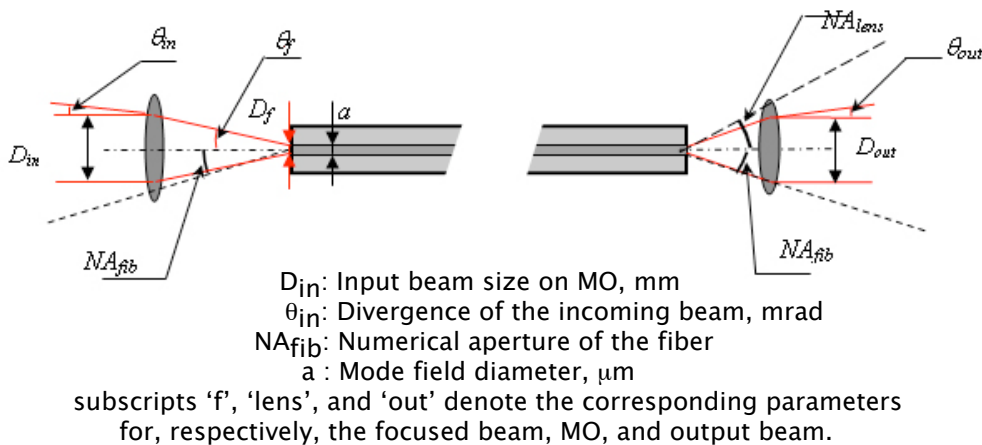


Figure 3.13: Air to fiber light coupling and collimation.

fiber launching system, which is required to match the plane of polarization of the beam with that of the fiber for efficient coupling. The output end of the fiber is placed on a fiber-to-free space launcher with a special tube (to firmly hold the fiber) fixed on a translation stage. The polarization of the outgoing beam is required to be horizontal, which is obtained by rotating the special tube. The beam is then coupled out by another RMS10X MO. As the NA of the MO is greater than that of the fiber (NA_{fib} is 0.14 - 0.18), significant losses in the out-coupling process can be avoided. The distance of the fiber end from the output MO can be varied with the help of the translation stage. To ensure the collimation of the beam, its focus has been set at a distance of $\sim 15 \text{ m}$ an order of magnitude longer than the distance to the crystal. The size of the seed beam at the crystal is 3.5 mm. To elim-

inate amplified pulses propagating back from the amplification stages towards the optical fiber, a broadband Faraday isolator (ISO-05-800-BB-G, Newport) is installed between the fiber and the amplification stages. Figure 3.14 explains the schematic of the setup. The

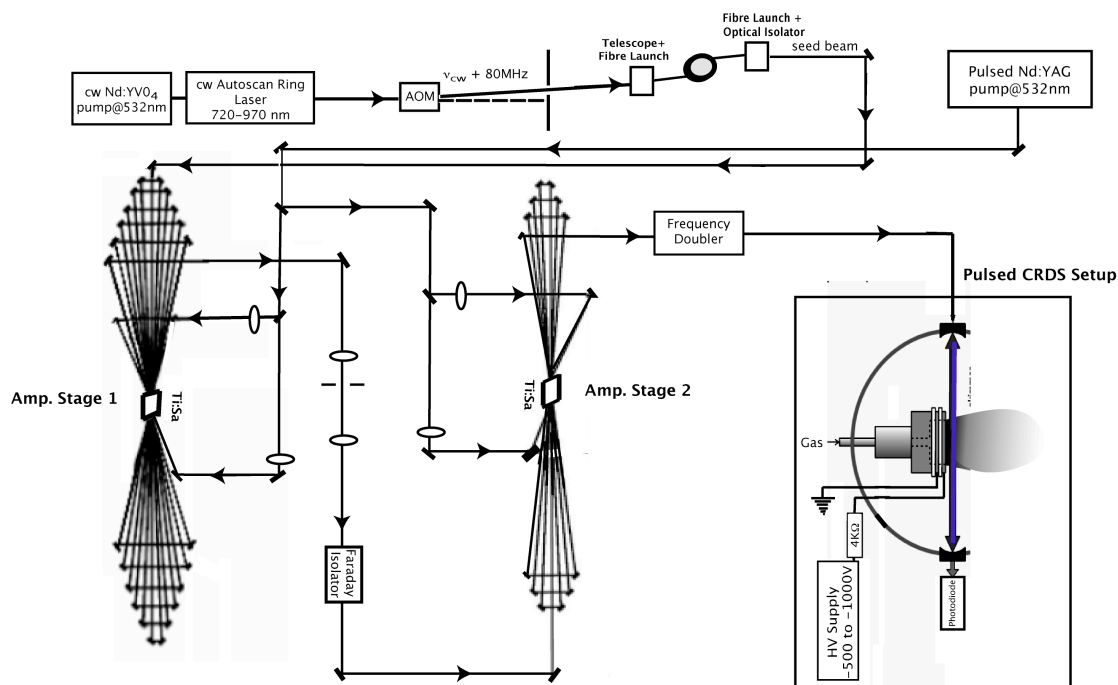
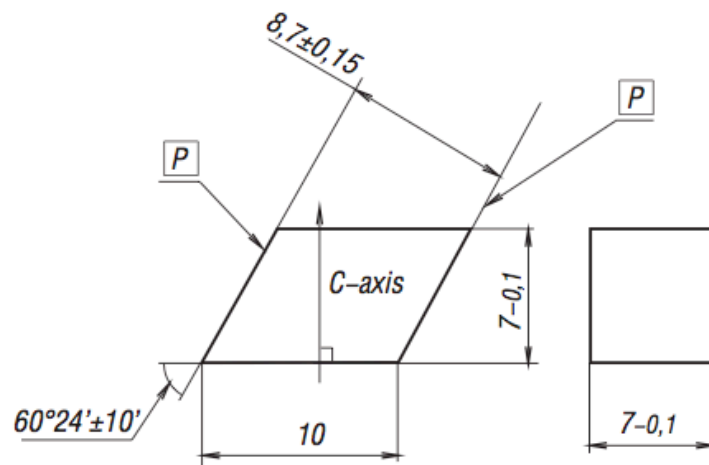


Figure 3.14: The schematic diagram of the experimental setup.

amplification of the NIR seed pulses is achieved in Ti:Sa crystals with Ti³⁺ ion concentration of 0.15 wt.% (weight percentage) and FOM > 150. The size of the crystals used is 7 x 7 x 10 mm. Figure 3.15 shows some of the characteristics of the crystal. This specific length is selected to ensure 95% absorption of the incident pump power within the crystal. The end faces of each crystal have been cut and polished at Brewster angle (60.4°) at the centre of the wavelength range, i.e. 800 nm. This is done to avoid reflection losses. The front surface is tilted by 29.60°. The c-axis is perpendicular to the crystal axis lying in the horizontal plane. Each crystal has been mounted in a water-cooled copper block that



Specifications

Ti^{3+} CONCENTRATION: 0,15%

P - LASER POLISH

SURFACE QUALITY: 20-10 SCRATCH AND DIG

SURFACE FLATNESS: 0,1 WAVE @633NM

PARALLELISM: 20 ARC SECONDS

ALL DIMENSIONS IN MM

Figure 3.15: The parameters of the Ti:Sa crystal.

is maintained at a temperature of 17° C. These are pumped by the frequency-doubled 7 ns pulses @ 20 Hz repetition rate from a Nd³⁺:YAG laser system (Innolas Spitlight-1200) using the multipass configuration displayed at the top of Figure 3.14. The pump beam is horizontally polarized and split into two beams with the help of a 50% beamsplitter. Special 50% reflectivity coating for the region of 532 and 355 nm has been made on the s-polarised beamsplitter (RS-DW-040, Sirah). A pulse energy of 150 mJ has been used to pump each of the amplifying stages. The specific value has been chosen to lie at 50% of the damage threshold of the crystals. A set of half-waveplate (RP-030, Sirah) and thin film polarizing beamsplitter (TP-020, Sirah) has been used externally, to control the pump energy. The pump beam in each of the stages, is further split into two parts by another 50% beamsplitter. The two beams are directed by custom-made mirrors (RM-DW-030,

Sirah) to pump the $\text{Ti}^{3+}:\text{Al}_2\text{O}_3$ crystal through the two opposite faces. These mirrors are made up of fused quartz, 35° - 45° p+s polarized and with high-reflection ($R > 99\%$) coating for the region of 532 and 355 nm. Typical damage threshold, specified, is $2 \text{ MW}/\text{cm}^2$ @ 355 nm / 10 ns. The corresponding value should be higher in the present case. The front (coated) area of the mirrors and beamsplitters is $50 \text{ mm} \times 27 \text{ mm}$. A set of biconvex lenses of 70 cm focal length have been used to reduce the size and intensify the pump beam photon density in the crystal. The lenses have broadband multilayer antireflection coatings for high transmission in the pump wavelength region (430 -700 nm) centered at 530 nm. These lenses establish a pump beam size in the crystal : $2\omega(x) \sim 2.0 \text{ mm}$. The NIR seed beam is passed multiple times through the crystal following a bow-tie shape with the help of a set of special mirrors. A pair, placed at the same distance on each side of the crystal (refer to Figure 3.14), makes 1 pass (except for the first pass which is made by just one mirror). A special high reflectivity ($R > 99\%$) coating for the region of 680-920 nm has been applied to these 45° p-polarised, Bk7 ($20.0 \times 20.0 \times 6.0 \text{ mm}$) mirrors (RM-140, Sirah). The damage threshold of these coatings is around $1 \text{ GW}/\text{cm}^2$. Kinematic mounts with vertical drive (VM1/M, Thorlabs) have been used which allow to place the mirrors closer and make fine tilt adjustments.

Satisfactory amplification is obtained when the pump beam size is reduced to match the size of the NIR beam in the crystal. In this case, optimal power densities and population inversion in the volume traversed by the seed beam are achieved. The pump laser thus boosts the seed laser intensity in the two stage amplifiers. The active diameter of the pump beam in the crystal is adjusted to avoid broadening caused by amplifier gain saturation [4]. This can be crucial as broadening would contribute to a final bandwidth at the output which would be larger than the FT limit of the pulse. This is achieved by defocusing the beams in the crystal to avoid gain saturation as well as any damage and other parasitic effects in the crystal. Pump and seed beams are directed through the Ti:Sa crystals in a near-collinear arrangement with their polarization vectors in the plane of the c-axis of the crystal, which lies in the horizontal plane in the laboratory.

3.2.1 Measurements

The NIR seed beam is passed through the first Ti:Sa crystal up to 12 and through the second 7 times. These are the maximum number of passes compatible with the pumping configuration. The energy of the seed beam evolving from the first stage during amplification (pumped by 150 mJ of 7 ns pulses) is 3.3×10^{-2} mJ. The broadband ASE background is less than 10%. It is collimated and spatially filtered by a telescope with a pin hole (50 μm) at the focus. This efficiently suppresses ASE which does not have a Gaussian profile. The beam is then incident on the second stage of the amplifier pumped by the same level of power (150 mJ of Nd³⁺:YAG). The two amplifier stages are optically decoupled by a polarizer and another broadband Faraday isolator to avoid problems associated with the radiation propagating backward in the amplification setup. The cw ring laser output which makes the seed beam is 30 mW. Single pass gain of 2.4 in each stage has been achieved. The output energy is measured after the second stage when pumped with a total of 300 mJ of the Nd³⁺:YAG laser. The energy of the amplified beam emerged is 15 mJ at a repetition rate of 20 Hz. The output beam size is found to be 1.5 mm.

The laser-pulse shapes and energies are measured using a fast photodiode and monitored via a fast oscilloscope (LeCroy 400 MHz 5 GS/s). At low energy, in the range of 1 nJ - 1 μJ , the pulse energies are determined by monitoring the relative increase of the photodiode signal after each successive pass in the Ti:Sa amplifier starting with the cw power. Beyond 400 μJ , the pulse energies are measured directly with the help of a thermopile detector. Under typical operation conditions, the characteristics of the laser amplification are found to be as follows:

- The peak power of the pulses is typically 30 mW before entering the amplification setup. This corresponds to 0.9 nJ energy for 30 ns pulses.
- The amplification factor dropped rapidly after pass 17. The depletion of population inversion is found to depend on the number of passes and the alignment of the seed beam through the amplification setup.

3.2.2 Measures to remove ASE

Suitable spatial filter is inserted between two stages to remove the undesirable ASE from the amplified beam of the first stage. The complete amplifier system is decoupled from the cw ring laser with an optical isolator consisting of a Faraday rotator and two polarizers.

To improve the beam quality,

- the ASE can be reduced by the use of spectral filters. The ASE is in general broadband and therefore will be cut off from the laser beam which exhibits a much narrower bandwidth.
- the two stages can be optically decoupled by an interference filter and a polarizer.

3.3 Results

For the Ti:Sa crystal used in the presented work, each pass has been found to contribute an amplification factor in the range of 2 to 3 to the overall amplification. Similar amplification has been observed by previous works reported e.g. in [33]. Typically two crystals are used. Overall 19 passes have been made using pump energies of 2×70 mJ per pulse and per crystal. One can obtain intense Fourier-limited coherent 30 ns laser pulses (Full Width at Half Maximum, FWHM) with energies of 15 mJ (\sim peak power of 5.0×10^5 W) from as low as 30 mW of cw power from the ring laser at a repetition rate of 20 Hz. The pulse shape is asymmetric with decay time ~ 5 ns.

Typically, the broadband ASE background is 20-30%. The power of residual ASE relative to that of the amplified seed pulse only becomes significant for short pulses $t \leq 10$ ns, where the maximum peak power is not reached, whereas for longer pulses ASE contributions are negligible. The advantage of the longer pulses does not reside in higher pulse energies but rather in a narrower FT-limited frequency bandwidth [34]. However, the application within this thesis is for frequency upconversion by nonlinear crystals; therefore, short pulses have been opted for.

The bandwidth of the amplified beam is estimated to be 15 MHz. Compared to a cavity, the multipass arrangement offers the advantage of bypassing the need to adjust

the cavity to the laser wavelength. More importantly, there is the possibility of freely adjusting the pulse length and thus achieving the best compromise between the opposing requirements of high resolution and high intensity.

3.4 The Frequency doubling

3.4.1 Frequency upconversion

By frequency doubling the NIR fundamental beam in a non linear crystal [35], the tunable range of the laser system can be extended to the range 360 to 465 nm . With 10% efficient doublers, in general, one can obtain 1.5 mJ/pulse from the 15 mJ of NIR pulses. Figure 3.16 shows the block diagram of the wavelength ranges, which can be covered by the use of additional equipments based on nonlinear processes. The size of the NIR beam in

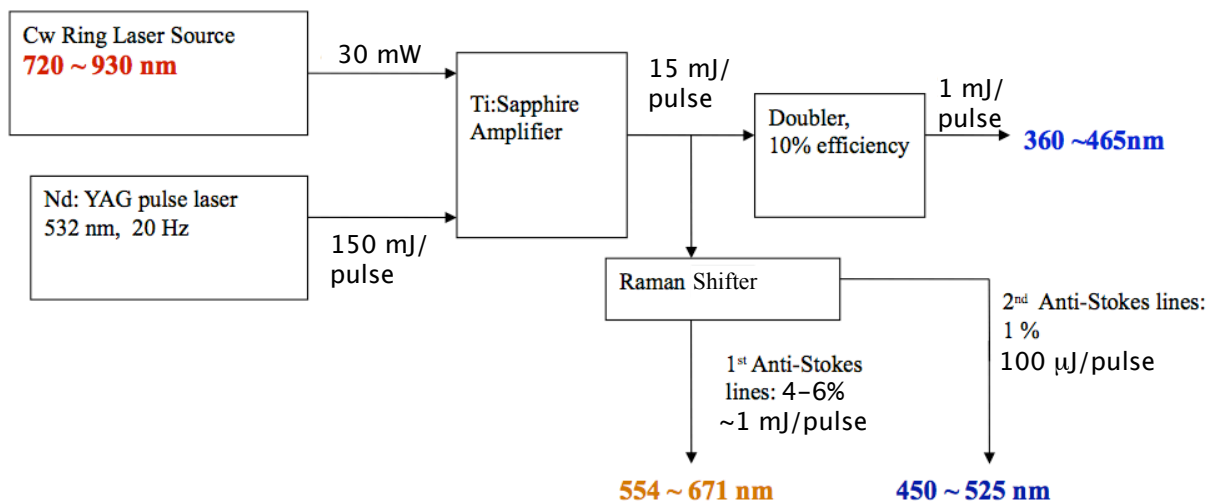


Figure 3.16: Frequency upconversions.

the non-linear crystals as well as the beam divergence (to minimize the phase mismatch) have to be carefully reduced to achieve optimal power densities and conversion factors [36]. Raman shifters also can be used. The first anti-Stokes lines generated can provide 1.5 mJ pulses (10% efficiency) spanning the range of 554-671 nm. The second anti-Stokes lines with 1% efficiency (15 μ J) gives a tunability over the range of 450-525 nm. Figure 3.17 shows a part of the autotracker setup to maintain phase matching during scanning.

3.4.2 Doubling crystals

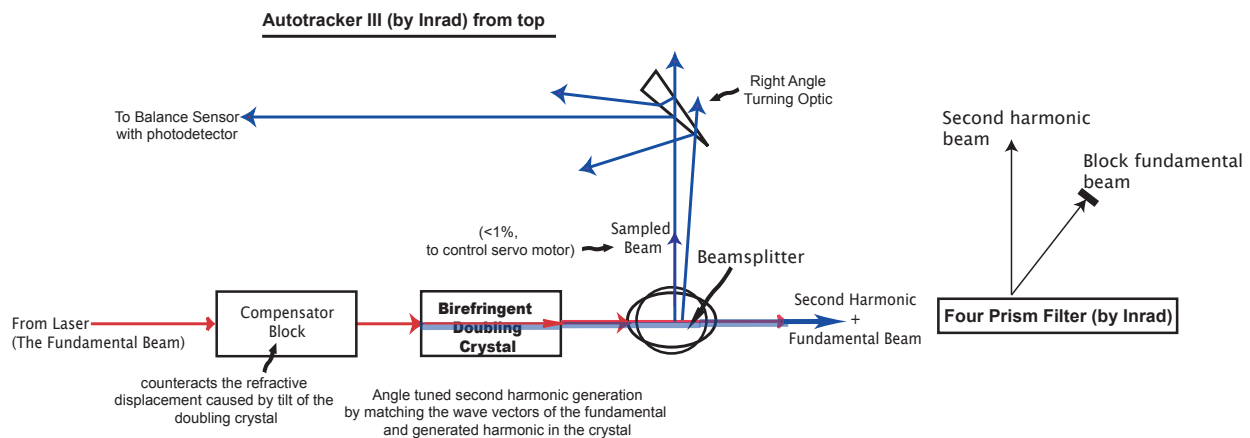


Figure 3.17: Execution of frequency doubling by the use of a nonlinear crystal. The angle of the crystal is tuned for the second harmonic generation by matching the wave vectors of the fundamental and generated harmonic in the crystal.

The beam is sent with a conventional pair of lenses to the doubler for second harmonic generation (SHG). It is a nonlinear optical process in which the output frequencies are

given according to the energy and momentum conservation by [37]

$$\omega_1 + \omega_2 = \omega_3 \quad (3.1)$$

$$k_1 + k_2 = k_3 \quad (3.2)$$

The phase matching (PM) angle of SHG for type-I phase matching is given by,

$$\theta(I) = \arcsin \sqrt{\frac{n_o^{-2}(\omega) - n_o^{-2}(2\omega)}{n_e^{-2}(2\omega) - n_e^{-2}(\omega)}} \quad (3.3)$$

where, $n_o(\omega)$ and $n_e(\omega)$ are the refractive indices for, respectively, the ordinary and extraordinary waves in the doubling crystal at the fundamental frequency ω .

The intensity of the second harmonic, however, depends on the phase mismatch induced by the angular deflection. The conversion efficiency also depends on the intensity of the input waves. The crystal length is limited by the angular sensitivity of the process and the beam divergence. Therefore, a minimum peak intensity is required to achieve efficient conversion [38]. The relevant figure of merit in comparing nonlinear materials is the ratio of the effective coupling to the angular sensitivity. The square of this ratio is expressible as a power which is approximately the peak laser power in a diffraction limited beam which is required for efficient conversion. The peak power required increases by Q^2 , where Q represents the beam quality, approximately the ratio of the beam divergence to the divergence of a diffraction-limited laser beam. The intensity of the SHG depends on the square of the intensity of the fundamental and on the square of the interaction length [39]. High peak powers and high beam quality are essential in order to achieve efficiency.

Conversion efficiency of SHG has been proven to be enhanced by focusing the fundamental light in the crystal [40]. Focusing the fundamental radiation can degrade the quality of the beam. A high efficiency also requires a narrow fundamental linewidth [41]. In the present work, 8 mm long β -barium borate (BBO) crystal has been used for the frequency doubling. The spectral acceptance bandwidth (FWHM) for type I SHG in BBO at $\lambda = 750$ nm is 0.29 nm which is wider than the actual linewidth of the fundamental beam

i.e. ($\sim 10^{-5}$ nm). This makes high-efficiency of SHG possible. Smaller optimum dimensions of the crystal (e.g. that for BBO in comparison to KDP) reduce the effects of beam walk-off [42]. A high resistance to optical damage permits the use of a smaller crystal size. The crystals are transparent in the UV and IR. For instance, the optical transparency range of BBO is in the range 188 to 3500 nm.

3.4.3 Setup

An efficient external SHG of the ns-pulsed amplified beam with narrow bandwidth has been achieved. The Autotracker III model from Inrad has been used for frequency doubling. This has a BBO-TSS Type I crystal, cut at $\theta = 28.7^\circ$, with a 5 x 7 mm cross section and 8 mm-long BBO crystal. In addition, it contains a compensator block assembly for the BBO, matched to the specific length of the crystal in order to avoid an overall refractive beam displacement as the crystal is tilted. The experimental configuration for frequency doubling is shown in Figure 3.17. BBO has been the choice instead of LBO as the effective SHG coefficient of BBO ($\sim 4.1 \times 10^{-9}$ esu) is larger than of LBO ($\sim 2.4 \times 10^{-9}$ esu).

The output pulse from the amplification system consisted of about 15-20 mJ with a duration of 30 ns. The input beam diameter is reduced to less than 2 mm from 4 mm with the help of a 1:2 Keplerian telescope before incident on the doubler. Within the limits of the angular acceptance of the BBO crystal, the propagation direction of the frequency-doubled beam is nearly independent of the deflection angle of the input beam. A conversion efficiency of 10% with SHG energy of 1.0 mJ/pulse has been reached for the fundamental energy of 15 mJ/pulse. The output energy and efficiency are dependent directly on the fundamental energy. Conversion efficiency decreased, as would be expected, because of phase mismatch in the crystal at increasing deflection angles. It can be seen that, due to the intrinsic properties of the BBO and the crystal thickness, the angular acceptance of the system is limited to a few milliradians. The angular sensitivity of β -BaB₂O₄ is $10600 \pm 200 \text{ cm}^{-1} \text{ rad}^{-1}$ [43]. A four prism filter (model 752-104) from Inrad has been utilized to separate the second harmonic from the fundamental radiation.

¹esu is the electrostatic system of units

3.4.4 The bandwidth

The temporal length and the bandwidth of the pulses is affected by the nonlinear processes used for the frequency upconversion. The bandwidth Γ_k of the radiation pulses at frequency $k\nu_{NIR}$ ($k = 2, 3, \dots$) generated in a nonlinear process, or a sequence of nonlinear processes, can be determined by convolution of the frequency spectrum of the beams involved in each process and amounts to $\sqrt{k}\Gamma_k$ if the pulses have a Gaussian frequency profile, or $k\Gamma_k$ if the frequency profiles are Lorentzian, where Γ_k represents the bandwidth of the NIR laser pulse. The pulse length t_k is correspondingly reduced and amounts to t_{NIR}/\sqrt{k} for Gaussian pulses. The estimated linewidth of the tunable blue output is ~ 20 MHz, provided that of NIR pulse is 15 MHz. The doubled beam can cover the spectral range from 350 to 470 nm with a maximum conversion efficiency of 10%.

3.5 Cavity ring down

A pulsed, nearly FT-limited light source has been produced. Its application for cavity ring-down spectroscopy (CRDS) in the UV spectral range is investigated. This is the case where the coherence time and duration of the light pulse (30 ns) exceeds the cavity roundtrip time (3.4 ns). That means mode beating would generate oscillations in the ring-down waveform. This situation can be avoided by careful choice of the cavity geometry and mode matching conditions together with suitable electronic filtering [44].

Normally, laser pulses having much larger spectral bandwidths than predicted by the FT limit have been used. The pulse duration has been much shorter than the cavity roundtrip time. The pulse can be viewed as a particle bouncing between two mirrors in which a small part of the pulse is transmitted each time the pulse hits a mirror surface (Figure 3.18a). The cavity output then consists of a train of pulses with exponentially decreasing maxima. The pulse never overlaps inside the cavity, and consequently interference phenomena cannot occur. A Fabry-Perot resonator has both longitudinal and transverse eigenfrequencies. In a stable optical 0.52 m long cavity with near continuum

mode structure, the minimum mode spacing (in MHz) is given by

$$\frac{c}{\pi d} \arctan \frac{d}{\sqrt{d(2r-d)}} = 98.3 \quad (3.4)$$

r , the radius of curvature of the plano-concave cavity mirrors, is 1 m. In the frequency domain, it can be stated that the free spectral range (FSR) of the cavity is much smaller than the pulse bandwidth for this situation so that the cavity transmits the pulse on many cavity modes. Typically, a laser power spectrum density width of ~ 1500 MHz at FWHM (0.3 ns pulse intensity width at FWHM) overlaps at least 15 cavity modes. The cavity output appears as pulses in time, which in frequency space, corresponds to the superposition of many cavity modes. As shown in Ref.[45], mode beating can be observed also in this situation. Figure 3.18 shows different combinations of pulse duration with cavity round trip time. In the present case, a pulse of a 30 ns FWHM has a coherence time slightly

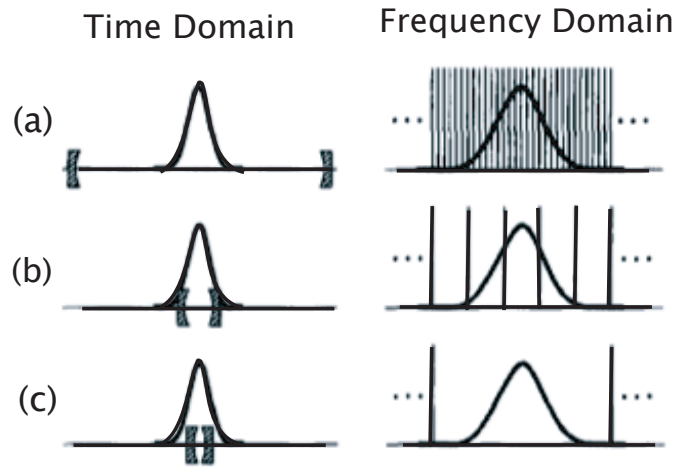


Figure 3.18: *Illustration of the interaction of an empty Fabry-Perot cavity with a Fourier-transform-limited Gaussian light pulse in the time and frequency domains: (a) the pulse duration is much shorter than the cavity roundtrip time; (b) the pulse duration and the cavity roundtrip time are comparable; and (c) the pulse duration is much longer than the cavity roundtrip time.*

smaller than 30 ns, and a bandwidth that is only slightly larger than the corresponding 15 MHz bandwidth in the Fourier limit at FWHM. This means that the pulse duration exceeds the cavity roundtrip time. This condition results in a cavity FSR exceeding the

laser bandwidth. In the case of FT-limited pulse (15 MHz), it does not overlap any cavity mode at all for some frequencies. If the center frequency of the pulse lies between two cavity modes, almost no light will be transmitted by the cavity. This situation makes it impossible to scan the laser frequency and record continuous absorption spectra.

In such cases, a simple and easy to use method is to couple laser into the cavity by the use of an off-axis cavity alignment geometry. The resonances commonly associated with optical cavities can be eliminated systematically while preserving the absorption signal amplified properties of such cavities [31]. This creates an extremely dense-mode spectrum and reduces the complexity of the apparatus [46]. The alignment patterns used here are common in multipass absorption cells but are actually first explored in conjunction with optical cavities [47]. Off-axis paths through optical cavities are first investigated in the mid-1960s [48]. This property is used to average the cavity transmission spectrum more effectively, resulting in an order-of-magnitude improvement in sensitivity. This allows a constant fraction of the incident laser power to be coupled through the cavity for each laser shot while the cavity remains passive, regardless of the laser center wavelength. To

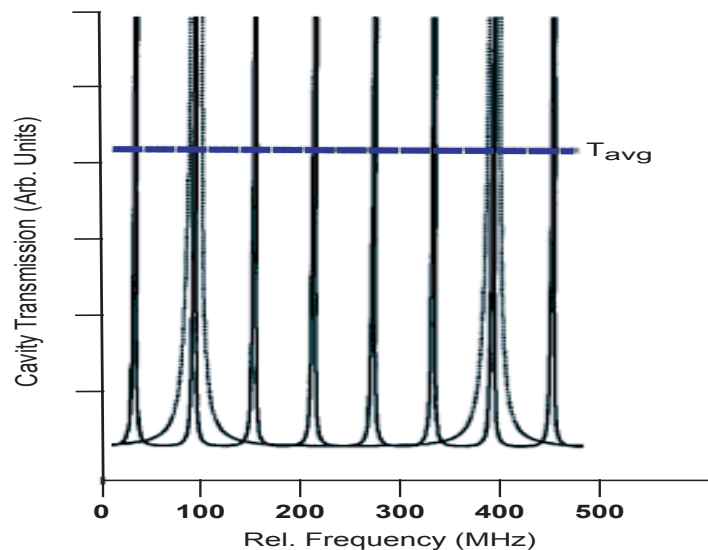


Figure 3.19: Predicted cavity-mode structure for a 52 cm cavity aligned on axis (dotted curve) and off axis in a 10-pass i.e. 5 round trip reentrant condition (solid curve). T_{avg} indicates the frequency-averaged transmission level.

illustrate this, consider Figure 3.19, which shows the expected cavity transmission versus frequency with reflective cavity mirrors aligned on axis (solid line) and off axis with a five round-trip reentrant condition (dotted curve). As the reentrant condition lengthens, the mode spacing continues to collapse. The limiting case in this situation is clearly the desired one, in which the cavity resonances are effectively suppressed. In this regime, the cavity transmission is frequency independent and is therefore determined solely by the round-trip cavity loss. The reentrant condition is dictated by the specific curvature and spacing of the mirrors forming the cavity. Any stable cavity geometry can produce stable off-axis paths through the cavity, with the stability condition (for a spherical two-mirror cavity) defined by the inequality

$$0 \leq (1 - d/R_1)(1 - d/R_2) \leq 1 \quad (3.5)$$

where d is the mirror spacing and R_1 and R_2 are the mirror curvatures. In the present case, $d = 52$ cm and $R_1 = R_2 = 100$ cm, the stability parameter is 0.2304, which satisfies the stability condition. The multiple reflections appear on the mirrors as a series of spots in an elliptical pattern. The per-pass rotation (θ) around the ellipse is again determined purely by the geometry of the cavity and is given by $\cos \theta = 1 - d/R$, assuming $R = R_1 = R_2$. Here, the per pass rotation (θ) is 61.3° . When $m2\theta = n2\pi$, where m equals the number of optical round-trip passes and n is an integer, the pattern becomes reentrant. $n \sim 10$, in the present case.

The non-resonant gain is reduced only by a factor of 2 compared with the expected gain when the laser is resonantly coupled to a single cavity mode [49]. The transmitted power level, on the other hand, is reduced by a factor of $\sim T/2$, or 2×10^4 for $T = 200$ ppm mirrors. In terms of the ultimately achievable shot-noise limit, however, the difference between the two methods is only $\sqrt{T/2}$ for a given source laser power or a factor of 200 in the current example.

Rather than a single possible alignment geometry (i.e., the laser on axis with the cavity), a virtually infinite number of stable paths through the cavity can be used. This allows for simpler alignment routines and lowers the sensitivity of the instrument to vibration

and misalignment. The potential drawbacks to this approach include the significantly lower power transmission through the cavity compared with resonant-coupling methods and the loss of spatial resolution in the probe axis that is due to the off-axis injection (Figure 3.19). In many cases, these are not limiting factors, particularly when moderately high-power lasers or sensitive detectors are available and when the sample of interest is not confined to a small area. Figure 3.20 presents a schematic overview of the experimen-

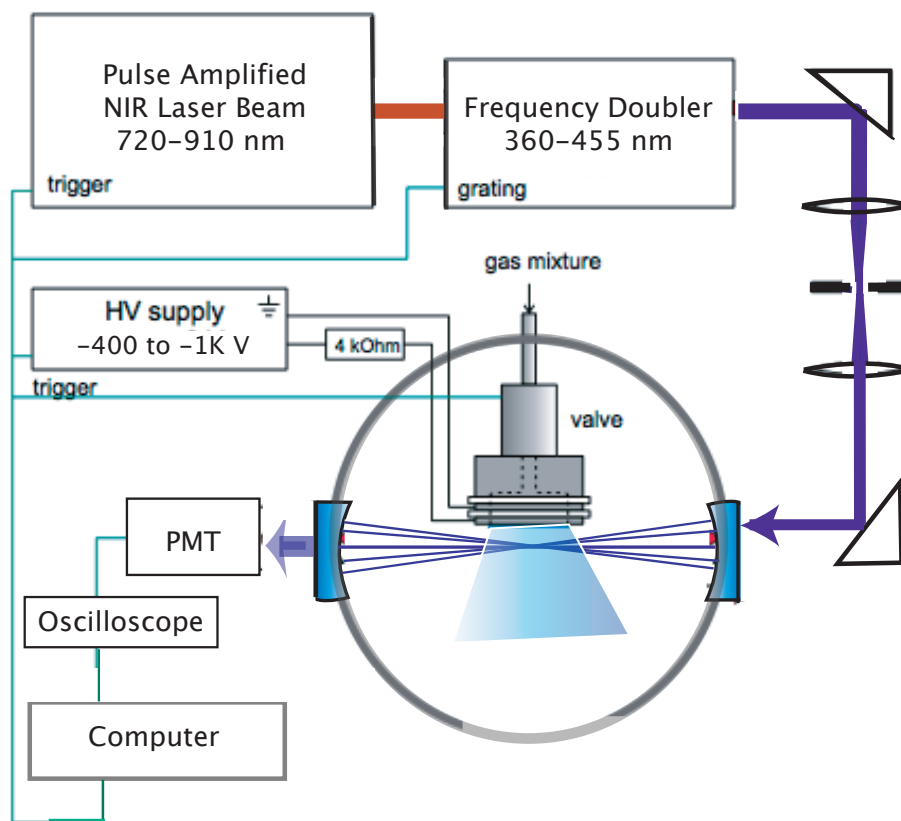


Figure 3.20: Schematic showing the off-axis technique for coupling the beam in a cavity of CRD.

tal setup. The pulse generated travels a distance of 2 m through a collimating telescope and enters an optical cavity that is formed by a pair of highly reflective plano-concave mirrors 52 cm apart. The mirrors of 25 mm diameter, 1000 mm radius of curvature and a reflectivity of 99.98 to 99.998% over 740-870 nm are produced by Layertec GmbH. Large

diameter mirrors would allow the multiple beams in the cavity to be spread over a larger area, thus decreasing their interaction. Mirrors are mounted on the chamber with flexible bellows tube that allowed fine adjustment of each mirror in order to create stable optical resonator. A roots pump system with total pumping capacity of 2775 m³/h maintained the background pressure of 10⁻³ mbar. During the experiment the pressure in the chamber is maintained at a certain level (normally, 0.060 to 0.200 mbar) by automatic adjustment of the valve opening time.

The off-axis cavity alignment is straightforward and reproducible. The laser and the cavity are aligned, first coaxially by centering the laser with respect to both mirrors and adjusting the mirrors such that the returning beams overlapped the incoming beam. At this point, any light leaving the cavity through the rear mirror would reveal a uniform spot with a minimum of non-TEM₀₀ structure, along with large power fluctuations in random intervals corresponding to mode coincidences between the laser and the unstabilized cavity. The final turning mirror in front of the cavity is then moved horizontally by ~ 1 cm with respect to the cavity axis. Following this, the light path through the cavity would trace out a horizontal line on each mirror. With a small adjustment of the same turning mirror in the vertical direction, the light path traces out a circle on each cavity mirror. The resulting image is actually the sum of thousands of slightly displaced spots. Figure 3.21 shows images that would be seen through the rear cavity mirror. The cavity output radiation is detected by a photo-multiplier tube (PMT). A narrow-band optical filter is placed in front of the detector to block most of the background light and the light generated by the discharge. The output from the detector is sent to a fast 400 MHz digital oscilloscope (LeCroy) controlled by a general-purpose interface bus from a standard PC. It records the ring-down waveforms at a 5 GSa/s sampling rate. The area of the signal is calculated and recorded. Traces are transferred to a personal computer, where they are summed and an average waveform is calculated. Typically, spectra are obtained by averaging the signal on 20 to 40 laser shots. LabView software together with a program written in tcl/tk language which runs on real time Linux system, is used to control the experiment and to process the data.

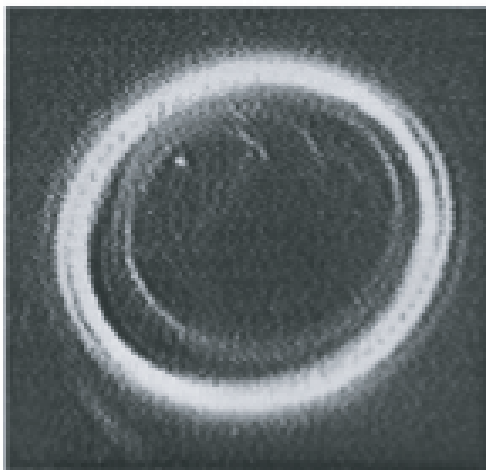


Figure 3.21: Image obtained by a video camera looking through the rear (spherical) mirror of the cavity showing the off-axis cavity alignment patterns.

The waveform gets modulated by different beat frequencies caused by different spacings of the overlapping modes. So, the problem of extracting the ring-down decay time constant from the waveform arises. The excitation of closely spaced modes causes the appearance of mode beating in the output from the passive optical resonator and changes the exponential decay waveform substantially. Consequently, a simple exponential decay of the waveform is not expected in general and failure to recognize the importance of interference effects can significantly bias the interpretation of ring-down spectra.

3.5.1 Result

The system was tested by recording C_3 lines in the region of 378.6 nm, as shown in Figure 3.22. As per simulation, the spectrum must show a hot band of the $A^1\Pi_u \leftarrow X^1\Sigma_g^+$ transition. Each point in this scan represents an average of 50 individual decay waveforms.

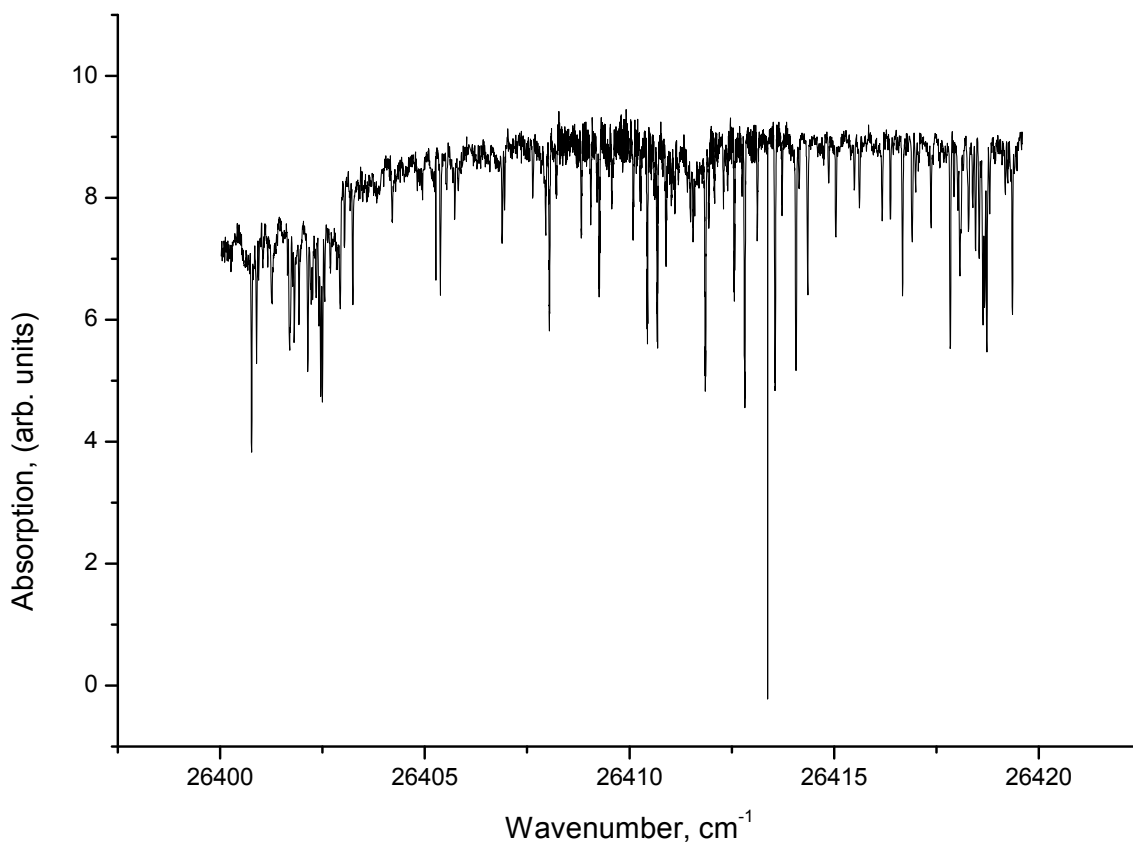


Figure 3.22: High resolution spectrum of C_3 in the region of its $A^1\Pi_u \leftarrow X^1\Sigma_g^+$ transition.

3.5.2 Calculation of the bandwidth of the laser beam.

The bandwidth of the beam can be inferred by acquiring an electronic transition spectrum of some radical available in the wavelength region of the system. The radicals are produced by the discharge of supersonic slit jet expansion which has a residual Doppler broadening of the order of 450 MHz. This is larger than the expected FT-limited bandwidth of the laser. Therefore, it is important to obtain a Doppler free spectrum [5] which can be achieved by the backward-geometry of DFWM. The width of the lines in the spectrum recorded will then give an estimation of the linewidth of the laser pulses produced by the pulsed amplification system, reported in this chapter. This in principle should be close to the value expected on the basis of the assumption that the bandwidth of the laser

is only limited by the FT of the laser pulse.

There is a possibility of shifts and chirps in the NIR frequencies [50]. The transient phenomena that are at the origin of the generation of pulsed side-band radiation in the AOM and of the amplification of the NIR radiation in the Ti:Sa crystals can cause time-dependent changes of the refractive index. This, potentially, results in the frequency chirps of the pulses. Such chirps can lead to a departure from the FT limit.

3.5.3 Outlook

The aim of the work presented in this chapter, is to produce the laser pulses in different wavelength regions which can be used for high resolution experiments. Such experiments demand high quality beams for better results. It has been observed that the process of amplification and frequency upconversion distorts the pulses. Therefore, it is important to implement a method to obtain a “clean” beam. The use of optical phase conjugation and frequency doubling to remove aberrations from a laser beam has been described in [51]. The technique, known as second-harmonic aberration correction (SHAC), produces a high-quality, collimated, second-harmonic beam from a distorted or divergent fundamental input beam. This allows correction of the beam distorted by the amplification media. The technique can improve beam quality .

In this method, a distorted input fundamental frequency beam is splitted into two beams of orthogonal polarization, one of which is directed onto a type II doubling crystal with conventional optics, as shown in Figure 3.23. The second beam is directed to the doubling crystal via a phase conjugate mirror. Thus the two beams overlapping at the crystal have orthogonal polarization and have conjugate wavefronts. The type II doubling process combines these beams to produce a second-harmonic beam with reduced aberrations. Since type II doubling requires one photon from each of the two polarizations, neither distorted beam alone can produce a second harmonic signal. Second harmonic remains along the principal axis, independent of the direction of the input beams. This has been tried on an artificially aberrated beam. The more general case is of a realistic laser beam with its own specific pattern of aberration. The SHAC technique has been proved

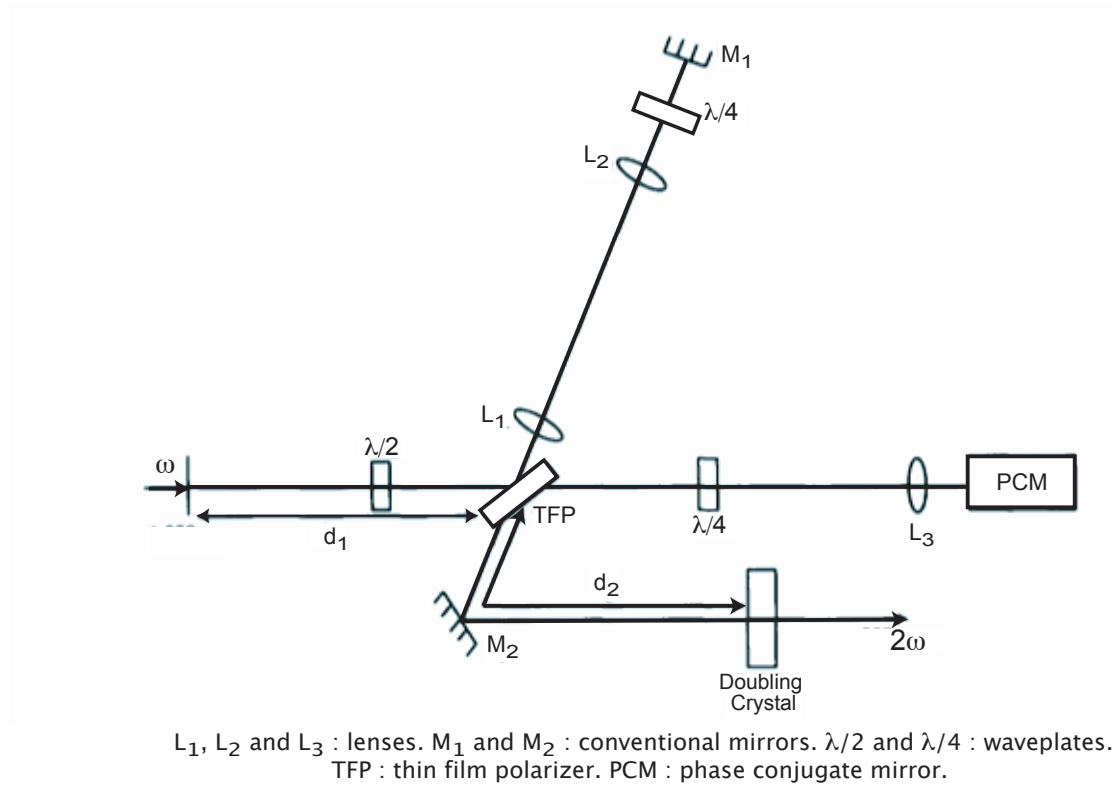


Figure 3.23: Schematic diagram of the apparatus for the second-harmonic aberration correction.

to be effective in removing much of the aberration in the general case as well.

Bibliography

- [1] B. C. Stuart, S. Herman, and M. D. Perry, *IEEE J. Quant. Electron.*, 1995, **31**, 528.
- [2] I. N. Ross, P. Matousek, M. Towrie, A. J. Langlely, and J. L. Collier, *Opt. Commun.*, 1997, **144**, 125.
- [3] H. Liua, W. Zhao, G. Chen, Y. Wang, L. Yu, C. Ruan, and X. Li, *Opt. Laser Tech.*, 2004, **36**, 309.
- [4] M. M. Salour, *Opt. Commun.*, 1977, **22**, 202.
- [5] U. Schubert, E. Riedle, and H. J. Neusser, *J. Chem. Phys.*, 1986, **84**, 5326.
- [6] N. Melikechi, S. Gangopadhyay, and E. E. Eyler, *J. Opt. Soc. Amer. B*, 1994, **11**, 2402.
- [7] E. E. Eyler, A. Yiannopoulou, S. Gangopadhyay, and S. Melikechi, *Opt. Lett.*, 1997, **22**, 49.
- [8] R. Seiler, T. Paul, M. Andrist, and F. Merkt, *Rev. Sci. Instrum.*, 2005, **76**, 103103.
- [9] M. Sneepe, S. Hannemann, E. J. van Duijin, and W. Ubachs, *Opt. Lett.*, 2004, **29**, 1378.
- [10] P. Dupre and T. A. Miller, (*private communication*).
- [11] J. Dong and P. Deng, *J. Crys. Growth*, 2004, **261**, 514.
- [12] R. R. Joyce and P. L. Richards, *Phys. Rev.*, 1969, **179**, 375.
- [13] E. D. Nelson, J. Y. Wong, and A. L. Schawlow, *Phys. Rev.*, 1967, **156**, 298.
- [14] H. H. Tippins, *Phys. Rev. B*, 1970, **1**, 126.
- [15] H. A. Weakliem and D. S. McClure, *J. Appl. Phys.*, 1962, **33**, 347–354.
- [16] A. Sennaroglu, *Prog. Quant. Electron.*, 2002, **26**, 287.
- [17] J. F. Pinto, L. Esterowitz, G. H. Rosenblatt, M. Kokta, and D. Peressini, *IEEE J. Quant. Electron.*, 1994, **30**, 2612.

- [18] P. F. Moulton, *J. Opt. Soc. Amer. B*, 1986, **3**, 125.
- [19] S. García-Revilla, F. Rodríguez, R. Valiente, and M. Pollnau, *J. of Phys: Condens. Matt.*, 2002, **14**, 447.
- [20] J. M. Eggleston, L. G. DeShazer, and K. Kangas, *IEEE J. QuantumElectron.*, 1988, **24**, 1009.
- [21] K. J. Weingarten, B. Braun, and U. Keller, *Opt. Lett.*, 1994, **19**, 1140.
- [22] M. J. Yarrow, J. W. Kim, and W. A. Clarkson, *Opt. Commun.*, 2007, **270**, 361.
- [23] J. Stanco, *J. Phys. D: Appl. Phys.*, 1997, **30**, 2536.
- [24] D. S. McClure, *J. Chem. Phys.*, 1962, **36**, 2757.
- [25] G. Malcolm and A. Ferguson, *Opt. Commun.*, 1991, **82**, 299.
- [26] W. R. Rapoport and C. P. Khattak, *Appl. Opt.*, 1988, **27**, 2677.
- [27] I. T. McKinnie, A. L. Oien, D. M. Warrington, P. N. Tonga, L. A. W. Gloster, and T. A. King, *IEEE J. Quant. Electron.*, 1997, **33**, 1221.
- [28] U. O. Farrukh and P. Brockman, *Appl. Opt.*, 1993, **32**, 2075.
- [29] M. E. Innocenzi, H. T. Yura, C. L. Fincher, and R. A. Fields, *Appl. Phys. Lett.*, 1990, **56**, 1831.
- [30] P. A. Schulz and S. R. Henion, *IEEE J. Quant. Electron.*, 1991, **27**, 1039.
- [31] C. Dudley, Absorption, fluorescence and amplified spontaneous emission of blue-emitting dyes, Master's thesis, Washington State University, 2004.
- [32] D. Goswami, *Phys. Rep.*, 2003, **374**, 385.
- [33] S. Hannemann, E.-J. van Duijn, and W. Ubachs, *Rev. Sci. Instrum.*, 2007, **78**, 103102.
- [34] J. Dingjan, B. Darquie, J. Beugnon, M. P. A. Jones, S. Bergamini, G. Messin, A. Browaeys, and P. Grangier, *Appl. Phys. B*, 2006.
- [35] P. Egger and J. Hulliger, *Coord. Chem. Rev.*, 1999, **183**, 101.
- [36] Z. Wang, B. Teng, K. Fu, X. Xu, R. Song, C. Du, H. Jiang, J. Wang, Y. Liu, and Z. Shao, *Opt. Commun.*, 2002, **202**, 217.
- [37] C. Song, J. Zhao, and J. Liu, *J. China Univ. Posts and Telecomm.*, 2006, **13**, 77.
- [38] Y. N. Lokhov, V. S. Mospanov, and Y. D. Fiveiskii, *Sov. J. Quan. Elec.*, 1972, **2**, 177.
- [39] K. Hussain and P. Kumbhakar, *Brazilian J. Phys.*, 2006, **36**, 1281.

- [40] G. A. Skripko, S. G. Bartoshevich, I. V. Mikhnyuk, and I. G. Tarazevich, *Opt. Lett.*, 1991, **16**, 1726.
- [41] X. Liu, D. Deng, Y. Zhang, and Z. Xu, *Chin. Phys. Lett.*, 1994, **11**, 551.
- [42] E. Li, J. Xi, and J. Chicharo, *Opt. Commun.*, 2004, **234**, 329.
- [43] D. Eimerl, L. Davis, S. Velsko, E. K. Graham, and A. Zalkin, *J. Appl. Phys.*, 1987, **62**, 1968.
- [44] J. Martin, B. A. Paldus, P. Zalicki, E. H. Wahl, T. G. Owano, J. S. Harris, C. H. Kruger, and R. N. Zare, *Chem. Phys. Lett.*, 1996, **258**, 63.
- [45] J. T. Hodges, J. P. Looney, and R. D. van Zee, *J. Chem. Phys.*, 1996, **105**, 10278.
- [46] G. Meijer, M. G. Boogaarts, R. T. Jongma, D. H. Parker, and A. M. Wodtke, *Chem. Phys. Lett.*, 1994, **217**, 112.
- [47] D. R. Herriott, H. Kogelnik, and R. Kompfner, *Appl. Opt.*, 1964, **3**, 523.
- [48] D. R. Herriott and H. J. Schulte, *Appl. Opt.*, 1965, **4**, 883.
- [49] J. B. Paul, L. Lapson, and J. G. Anderson, *Appl. Opt.*, 2001, **40**, 4904.
- [50] K. F. Wall, P. A. Schulz, R. L. Aggarwal, P. Lacovara, and A. Sanchez, *IEEE J. Quant. Electron.*, 1993, **29**, 1505.
- [51] R. P. Johnson, *Opt. Commun.*, 1990, **77**, 231.

Chapter 4

Molecules studied by four wave mixing spectroscopy

4.1 Theory of degenerate and two-color variants of the method

4.1.1 Overview

With the progress in laser technology, non-linear optical (NLO) techniques [1] are becoming increasingly important tools in chemistry. Most NLO techniques involve a few to several laser beams and a distinct signal beam. However, the single defining characteristic of a NLO experiment is that the intensity of the observed signal is proportional to the n^{th} power of the laser intensity, where $n > 1$. Examples of NLO techniques which have been used in chemistry include the photon echo [2], second-harmonic generation [3], and hole burning [4, 5]. The most widely used NLO technique in chemistry, is the transient grating (TG) [6, 7]. TG experiments have been performed in all phases of matter.

To form a TG, two time-coincident laser pulses of wavelength λ are crossed at an angle θ in a medium. The electric fields of these excitation beams interfere with one another, resulting in a spatially-modulated net electric field in the beam-crossing volume. Figure 4.1 illustrates the phenomenon. The fringe spacing of the pattern formed is given by

$$d = \frac{\lambda}{2\sin(\theta/2)} \quad (4.1)$$

The interference pattern can then interact with the medium through mechanisms such as absorption, the optical Kerr effect, and stimulated Brillouin scattering (Figure 4.2). This

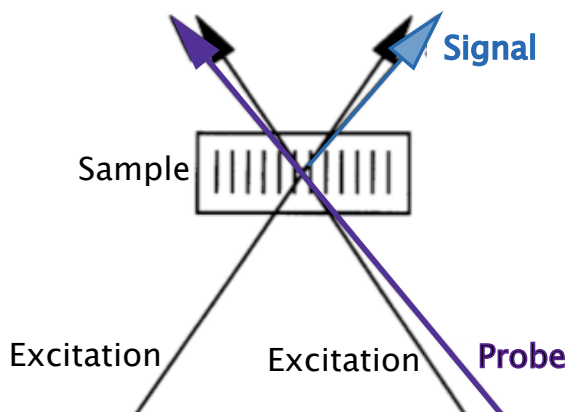


Figure 4.1: TG experimental geometry. The excitation beams are crossed at an angle and temporally and spatially overlapped, creating a spatial interference pattern that writes a grating (volume hologram) into the medium being studied. The probe beam is sent at the grating Bragg angle with a delay time t ; the resultant diffracted signal is recorded as a function of t .

interaction in turn produces a periodic spatial modulation in the complex index of refraction of the medium, thereby creating what is, in essence, a temporary volume hologram (a diffraction grating). If after certain delay time t a probe laser beam is sent to the grating at the corresponding Bragg angle, a part of the beam will be diffracted. The strength of the diffracted signal is directly related to the depth of the induced grating (i.e., the peak/null difference in the complex index of refraction). This can be monitored as a function of t . The TG signal is sensitive to any time-dependent process that can affect the spatial modulation of the complex index of refraction. The polarizations of the excitation beams determine the dynamic processes to which the TG decay is sensitive. These beams are most commonly of either parallel linear polarizations, forming an intensity grating (IG), or perpendicular linear polarizations, forming what is called a polarization grating (PG). The IG electric field is of the same polarization throughout, but is modulated sinusoidally in amplitude across each grating fringe (Figure 4.3). The IG signal beam is in general of the same polarization as the beam used to probe the grating. The PG electric field is constant in amplitude, but its polarization is spatially modulated; the polarization changes from right circularly polarized (rcp) to linearly polarized at -45° to left circularly

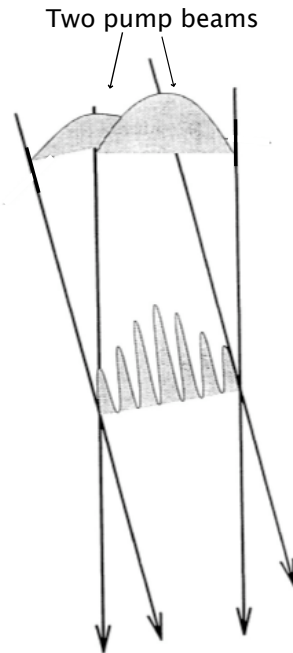


Figure 4.2: The interference of two frequency-degenerate beams leads to a spatial modulation of the refractive index of a non-linear medium. In the regions where electric field strength is high as a result of constructive interference the local refractive index is modified through the photo-refractive effect.



Figure 4.3: Electric-field picture for a single fringe of an IG (in which the excitation beams have parallel polarizations). The polarization of the electric field is constant across the grating, but the field amplitude is sinusoidally modulated.

polarized (lcp) to linearly polarized at $+45^\circ$ and then back to rcp across each fringe, with elliptical polarizations interspersed in between. Figure 4.4 shows the sequence of the different polarizations of the electric field [8]. If the polarization of the beam used to probe a PG is parallel to the polarization of one of the excitation beams, then the signal beam is polarized parallel to the other excitation beam.

Because the IG electric field is a sinusoidal modulation, it is easy to understand both how the IG diffracts light and decays. Any process that causes the grating peaks to lose



Figure 4.4: *Electric-field picture for a single fringe of a PG (in which the excitation beams have perpendicular polarizations).*

population and/or the grating nulls to gain population will wash out the grating and, therefore, cause the diffracted signal to decrease. There are frequency-domain analogues of TG, *viz.* degenerate four wave mixing (DFWM).

4.1.2 Degenerate four wave mixing

While many variants of DFWM spectroscopy are possible [9], the present work has made use of the forward-box configuration illustrated in Figure 4.5. For this phase-matching geometry, the three incident beams of identical frequency are directed to the target medium in a nearly-copropagating fashion such that they traverse distinct diagonals of a rectangular parallelepiped (or box). Nonlinear interactions enhanced strongly by resonant interaction with the molecular sample give rise to a signal wave. The signal is constrained, by conservation of linear momentum, to emerge along the “dark” axis of the detection defined by the remaining diagonal ($\vec{k}_4 = \vec{k}_1 - \vec{k}_2 + \vec{k}_3$) [10, 11]. Although not affording the sub-Doppler spectral resolution inherent to other DFWM schemes [9], this forward-box arrangement does provide superior immunity from scattered background light. Further, it has the unique advantage of ensuring temporal coincidence among all optical pulses as they pass through the molecular sample. Resonant DFWM spectroscopy makes use of the photo-refractive response of a non-linear medium to generate a fourth signal beam. The effect is particularly strong close to a molecular resonance and, hence, can be used as a spectroscopic probe. In the gas phase the technique is a hybrid between laser induced fluorescence (LIF) and Coherent anti-Stokes Raman scattering (CARS). Similar to CARS, the signal is detected as a spatially and temporally coherent beam, but like LIF the tech-

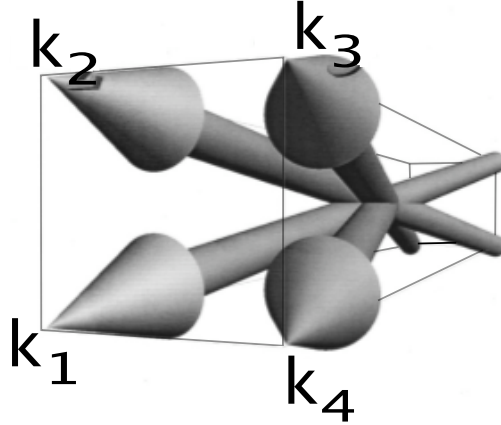


Figure 4.5: Forward-box configuration for DFWM spectroscopy. Three degenerate waves denoted by propagation wave vectors \mathbf{k}_1 , \mathbf{k}_2 , and \mathbf{k}_3 are directed in a nearly copropagating fashion through distinct diagonals of a rectangular parallelepiped (or box). Resonant nonlinear interactions mediated by target molecules placed in the region of mutual beam overlap (the DFWM interaction region) generate a signal beam (\mathbf{k}_4) that emerges along the dark axis of detection defined by the remaining diagonal so as to satisfy conservation criteria imposed upon linear momentum ($\mathbf{k}_4 = \mathbf{k}_1 - \mathbf{k}_2 + \mathbf{k}_3$).

nique relies on the resonant interaction of the light frequency with a molecular transition frequency (see Figure 4.6). It is therefore more sensitive than non-resonant CARS and less complicated experimentally [12].

Lets us denote the signal intensity as I_{DFWM} and the probe intensity as I_P . If the two pump beam intensities are assumed to be equal (denoted by I) and no gain is considered, one can obtain an expression for the line-centre signal intensity,

$$I_{DFWM} = \alpha_0^2 L^2 \frac{4(I/I_{sat})^2}{(1 + 4I/I_{sat})^3} I_P \quad (4.2)$$

where α is the one-photon absorption coefficient, L is the interaction length, and I_{sat} is the saturation parameter. One should note that equation (4.2) predicts a quadratic dependence of the signal on the absorption coefficient.

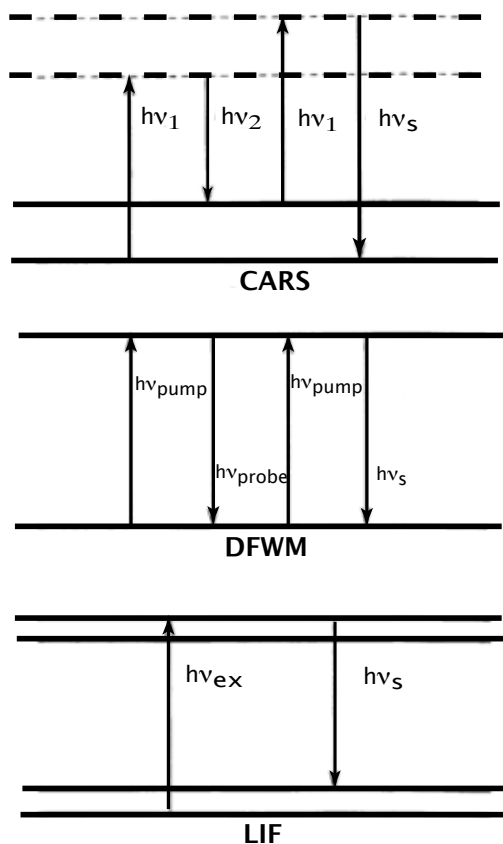


Figure 4.6: Excitation schemes for CARS, DFWM and LIF. Like CARS, DFWM is a four-wave mixing process but is similar to LIF because it is a resonant process. The energy of the signal photon is denoted by $h\nu_s$.

4.1.3 Two-color resonant four-wave mixing

Two-color resonant four-wave mixing (TC-RFWM) represents another set of fully resonant wave-mixing processes in which two optical fields have frequencies in resonance with two distinct molecular transitions. TC-RFWM has potential as a tool for various double-resonance schemes in molecular spectroscopy (where two transitions share a common level). TC-RFWM has been used to perform excited-state double-resonance spectroscopy on stable molecules [13, 14] and to provide background-free stimulated emission pumping (SEP) spectra of stable [15] and transient species [16, 17]. TC-RFWM has also been used to detect the CH radical in an oxyacetylene flame [18]. Such works prove

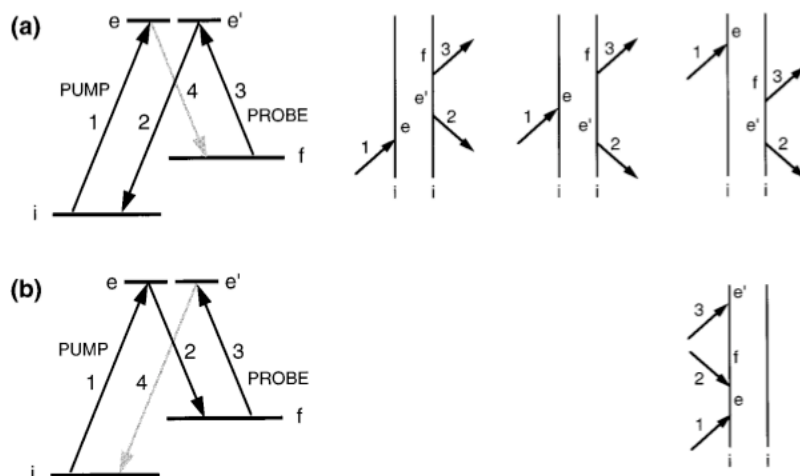


Figure 4.7: *Folded energy-level schematics and double-sided Feynman diagrams used to identify the resonant terms in χ^3 for the TC-RFWM schemes appropriate to SEP spectroscopy: (a) $\omega_1 = \omega_2$ (PUMP) and $\omega_3 = \omega_4$ (PROBE or DUMP); (b) $\omega_1 = \omega_4$ (PUMP) and $\omega_3 = \omega_2$ (PROBE or DUMP). The letter labels refer to specific degenerate magnetic sublevels in each rovibronic state; the letters e and e' denote magnetic sublevels (either the same or different) in the excited state.*

the versatility of the technique. Let us consider three input fields of arbitrary polarization which interact with an isotropic sample to produce a fourth field. Assume that field propagation effects can be ignored (negligible absorption) and the TC-RFWM process couples levels of sharp (definite) angular momentum J (omitting nuclear spin). The three-level energy diagrams and field labelings are presented in the following Figures 4.7, 4.8 and 4.9. The level labels correspond to individual magnetic sublevels, either the same or different, of each rovibronic state where i denotes levels in the ground state and e and f denote levels in excited states. RFWM is subject to both energy and phase matching constraints. In TC-RFWM there are three types of spectroscopic schemes which can be constructed within the energy constraints of two resonant input frequencies. Figures 4.7 and 4.8, each, illustrate double resonances where the excited-state level e is common to both transitions. The folded diagram in Figure 4.7 corresponds to SEP spectroscopy in which the $e - i$ transition is the PUMP and the $e - f$ transition is (for consistency) denoted as the PROBE. The probe transition is more commonly referred to as the DUMP transition

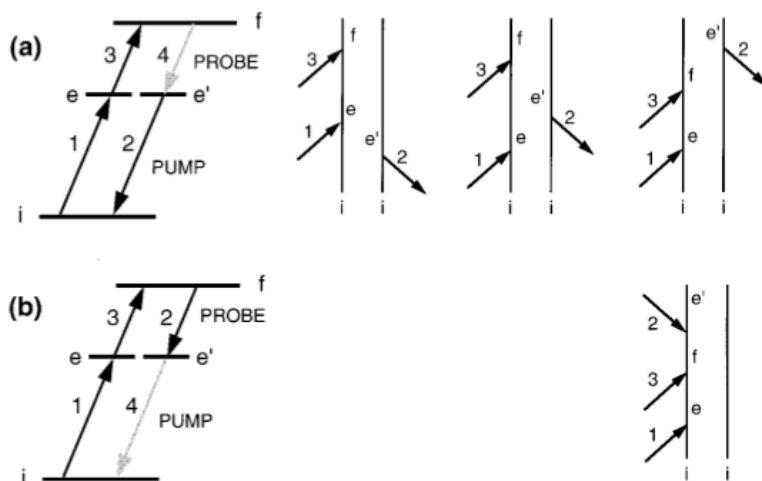


Figure 4.8: Unfolded energy-level schematics and double-sided Feynman diagrams used to identify the resonant terms in $\chi^{(3)}$ for the TC-RFWM schemes appropriate for excited-state PUMP/PROBE spectroscopy: (a) $\omega_1 = \omega_2$ (PUMP) and $\omega_3 = \omega_4$ (PROBE); (b) $\omega_1 = \omega_4$ (PUMP) and $\omega_3 = \omega_2$ (PROBE). The letter labels refer to specific degenerate magnetic sublevels in each rovibronic state; the letters e and e' denote magnetic sublevels (either the same or different) in the excited state.

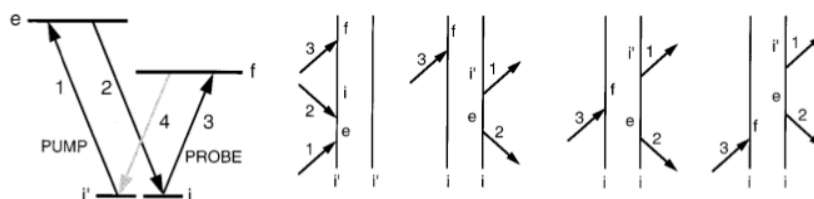


Figure 4.9: Open energy-level schematics and double-sided Feynman diagrams used to identify the resonant terms in $\chi^{(3)}$ for the TC-RFWM process appropriate for ground-state double-resonance (hole-burning) spectroscopy: $\omega_1 = \omega_2$ (PUMP) and $\omega_3 = \omega_4$ (PROBE). The letter labels refer to specific degenerate magnetic sublevels in each rovibronic state; the letters i and i' denote magnetic sublevels (either the same or different) in the ground state.

in SEP. Figure 4.8 shows the unfolded diagram appropriate for excited-state spectroscopy (often called optical - optical double resonance (OODR) in which the $e - i$ transition is again the PUMP and the $f - e$ transition is the PROBE. For each of these excited-state common schemes, there are two possible RFWM energy level diagrams which satisfy the same energy conservation constraints but have different phase matching criteria, i.e., (a)

$\omega_1 = \omega_2$ (PUMP) and $\omega_3 = \omega_4$ (PROBE) and (b) $\omega_1 = \omega_4$ (PUMP) and $\omega_3 = \omega_2$ (PROBE). Figure 4.9 illustrates a double resonance in which the ground-state level i is the common level. Here the $e - i$ transition is the PUMP and the $f - i$ transition is the PROBE. This double-resonance approach is often referred to as hole-burning spectroscopy since the effect of the PUMP laser is to burn a hole in the ground state population that is detected by its effect on the action (usually *fluorescence*) induced by the PROBE laser. There is only one TC-RFWM energy level diagram for hole-burning spectroscopy, because both transitions sample the initially populated level and their labeling as PUMP and PROBE is arbitrary [19].

4.2 Observation of N_2^+ and C_2

4.2.1 Introduction

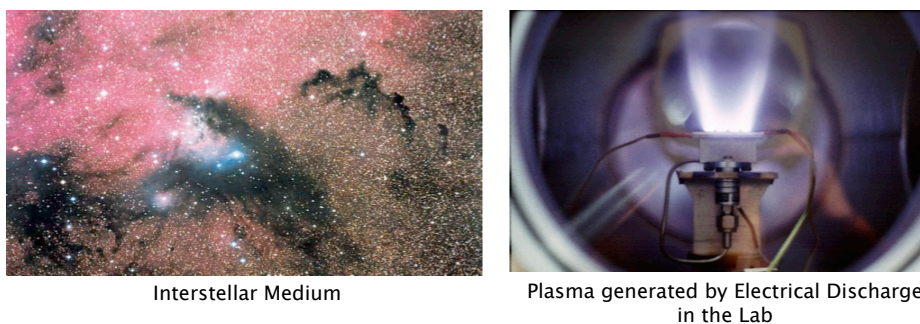


Figure 4.10: *Ionized Environment.*

Spectroscopic studies of gas-phase molecular ions and in natural environments unsaturated carbon-chain radicals provide an important means to enable their identification. Such transient species play crucial roles in combustion, plasmas and ionized environments prevalent in interstellar space (Figure 4.10). The studies furthermore would make a radio-astronomical search for these species in the dense interstellar clouds possible. Atomic hydrogen (H) is efficiently converted to H_2 on the surfaces of the cosmic dust grains and therefore little H remains in the gas phase. Much or most of the chemically

active atoms then react with H_2 and each other, to form the many observed molecules by a complex web of reactions. In this synthetic process ions produced by cosmic rays are thought to play a key role [20]. There are several ions which are particularly important in the formation of interstellar molecules, most notably $C_3H_3^+$ [21] and $SiCCH^+$ [22]. Ion-

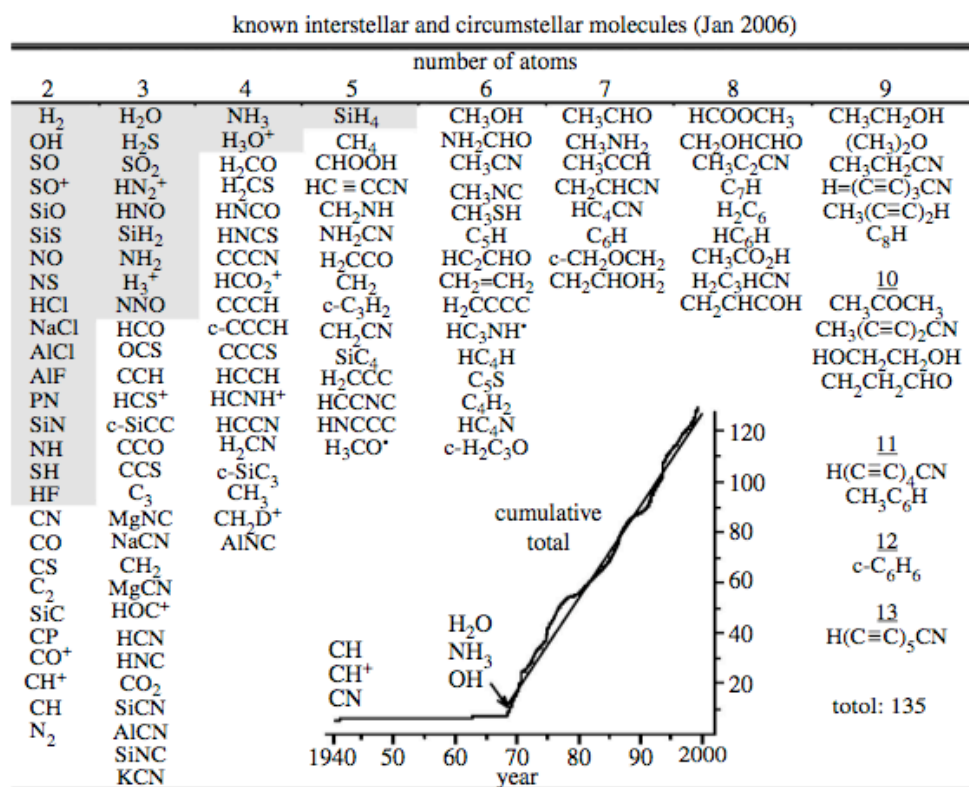


Figure 4.11: Molecules identified in the interstellar gas and in circumstellar shells, ranked by number of atoms. Reproduced from [23].

molecule reactions are especially important because their reaction cross-section may be hundreds or thousands of times larger than the geometrical cross section of the molecules involved. Moreover, such reactions typically have no activation barrier, and so remain very rapid at temperatures close to absolute zero where many neutral molecule reactions are frozen out [24]. Positive ions are readily formed in the interstellar gas. At least eleven positive molecular ions have now been detected in space (Figure 4.11). Probably many

more will be found when laboratory rest frequencies are in hand. Besides H_2 carbon has an exceptional position (refer to Figure 4.11) [25, 26].

In 2004, Maier et al. [27] summarized the current situation in the context of laboratory studies carried out in recent years not only on bare carbon chains, but also their ions and simple derivatives containing hydrogen or nitrogen. This is of interest as the number of microwave studies of carbon chain cations is still rather limited [28]. Carbon is abundant in the universe. The carbon atoms readily form stable compounds with themselves and with atoms of other elements, like H, N, and O. The addition of any of the three

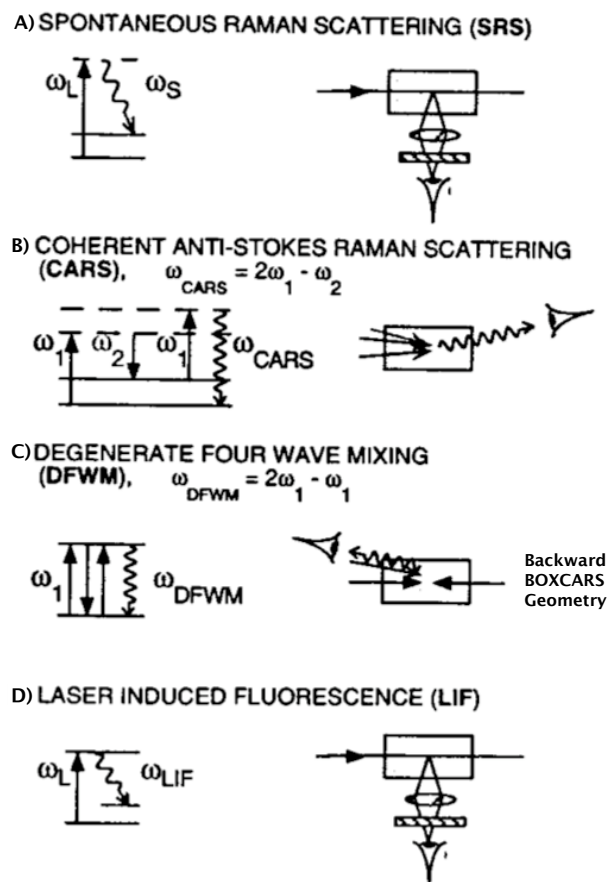


Figure 4.12: Laser spectroscopic techniques. The relevant energy level diagrams are on the left. Upward-facing arrows indicate photon absorption (or conversion); downward-facing arrows depict photon emission; $\omega_i = 2\pi\nu$ are the frequencies of the fields involved. The right column depicts a simplified experimental setup for the corresponding method with beam(s) and detection arrangements. [?]

remaining elements to carbon increases enormously the number of possible stable compounds. Besides, the radioastronomical observation of many interstellar molecules with a carbon skeleton point to carbon as the basic building material of the carriers of DIBs. Inert-gas matrix studies of the cations of fullerenes, PAHs, and of neutral and charged carbon chains that contain additional hydrogen or nitrogen atoms have shown that these systems may be responsible for the existence of DIBs. However, no convincing identification exists to date [29]. Another exceptional element is nitrogen, because it can easily replace carbon atoms in molecules to form chain, planar or spherical systems. Elementary nitrogen element is also considered to be the possible candidates for DIB carriers, but some contribution of heavier elements to the formation of such molecules cannot be excluded.

For the laboratory studies of such species, a variety of spectroscopic techniques are available. The particular strengths and weaknesses of the techniques govern the viability of their application. The factors which can be considered before choosing a technique include sensitivity, dynamic range, applicability to a variety of chemical species, the capability for multidimensional measurements, the capability for quantitative measurements and the degree of experimental complexity. Among the leading diagnostics are spontaneous Raman scattering, LIF and CARS, which are compared in Figure 4.12. DFWM and its variant TC-RFWM has received a renewed attention as the technique offers many advantages. DFWM is a non-linear optical process. It is background-free and produces

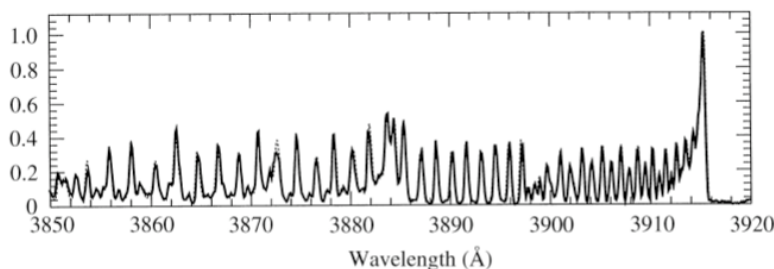


Figure 4.13: Spectrum obtained with a plasma of nitrogen (100 slpm) diluted into argon (50 slpm). The plasma generated with a 50 kW radio-frequency inductively plasma torch operating at atmospheric pressure. Rotational temperature of 4850 K has been obtained. Reproduced from[30].

a coherent signal which can be discriminated from scattered radiation [31]. The process does not suffer from fluorescence quenching compared to incoherent techniques, such as LIF [32, 33]. DFWM can therefore probe non-fluorescing species. The dynamic range which can be covered is large. It has also proven to be highly sensitive, with obtained signal-to-noise (S/N) ratios as high as 10^4 with the species concentrations present in a discharge [34]. These make DFWM particularly attractive for measurements in luminous and harsh environments like air and nitrogen plasmas.

Accurate spectroscopic measurements of temperature and species concentrations in air and nitrogen plasmas are of importance for the understanding of atmospheric reentry flows, and for the characterization of arcjets, radiofrequency or microwave plasma torches. In addition, nitrogen plasmas have much potential application in industry for the modification and improvement of the biological and chemical properties of the surface of different materials (hardness, anti-corrosion and wear). Flowing post-discharges in nitrogen-containing plasmas have been used for steel surface nitriding [35], for thin-film deposition [36] and more recently in bacterial sterilization [37]. In order to gain a better understanding of elementary processes occurring in these media, also with the aim of improving the efficiency of its applications, a large number of both experimental and theoretical works have appeared in the literature during the last few decades (see [38] and references therein). In air or nitrogen plasmas, the 0-0 band of the N_2^+ first negative system has often been used for rotational and vibrational temperature measurements. Figure 4.13 shows a part of this spectrum. In the figure, slpm is the flow rate unit 'standard liters per minute'.

In order to aid some proposed laser experiments and astronomical observations of O_2^+ and N_2^+ , some of the molecular constants have been remeasured. Although spectra of N_2^+ have been known for many years, there were serious omissions of the constants of their ground electronic states [39]. Rotational analyses of the $B^2\Sigma_u^+ - X^2\Sigma_g^+$ system of the $^{14}N_2^+$ molecule have been extended to include the vibrational levels up to $v' = 4$. The application of cavity ringdown laser absorption spectroscopy (CRDS) has been demonstrated by the measurement of the (6,0) band of $A^2\Pi_u - X^2\Sigma_g^+$ transition in N_2^+ molecule [40]. This electronic transition in the near infrared, known as the Meinel bands, has been studied by

several investigators [41, 40].

In the work reported, here, the potential of DFWM for cation spectroscopy has been tested by applying it to the detection of $B^2\Sigma_u^+ - X^2\Sigma_g^+$ transition of $^{14}\text{N}_2^+$ with the origin at 391.03 nm. Until now, the FWM technique has been used for measurements in molecular free-jet expansions only for a limited class of relatively small molecules and radicals, such as formaldehyde, SO_2 [42, 43], SiC_2 [44], C_2H_2 [45], CS_2 [46], C_3 [47] generated by laser vaporization, predissociation spectroscopy of NO [47, 48]. The detection of C_2 and of HC_4S also have been reported in a supersonic slit-jet discharge with DFWM and TC-RFWM [49, 50]. To date, FWM has not been applied to cations in a discharge. The first detection of a molecular cation N_2^+ by DFWM with origin at 391.0 nm has been reported. A high-quality absorption spectrum of nitrogen ions by DFWM has been obtained. DFWM is very critical to the alignment of the input beams. The measurement of singlet-singlet transition of C_2 with origin at 385.06 nm by the same configuration has been demonstrated. This transition is excited from a state 8391 cm^{-1} above the ground level. This finding is important and promising, because, it paves the way to look for the vibronic bands of different molecules or radicals, as well.

4.2.2 Experimental

Radicals have been generated by pulsing pure nitrogen or $\text{C}_2\text{H}_2/\text{Ar}$ gas through a $30.0\text{ mm} \times 1.0\text{ mm}$ slit-jet nozzle. A short ($\sim 10\ \mu\text{s}$) negative high voltage pulse ($\sim -1000\text{ V}$) is applied to the electrodes. The timing between the gas pulse, discharge and laser is optimized by the help of a digital delay generator with nanosecond (ns) resolution. Backing pressure of 10 bar is used with a cavity pressure of about 0.04-0.06 mbar. The point of observation height is set to $\sim 3\text{ mm}$ after the orifice of the nozzle. A dye laser pumped by the third harmonic of a Nd:YAG laser operated at 20 Hz produced pulses of 8 ns duration. PBBO dye is used allowing continuous coverage of the 386 to 420 nm spectral range with a 0.1 cm^{-1} linewidth. An intracavity etalon enabled reduction of the laser linewidth by a factor of 5. The laser energy is of the order of 1 mJ per pulse and variable neutral-density filters are used to reduce the laser-beam intensity because saturation of the FWM signal results in broadening of the absorption lines. Frequencies are calibrated by a wavemeter

(High Finesse/Angstrom, WS7). The beam is spatially filtered by a set of pinholes and a telescope in order to obtain a homogeneous profile. Broadband dielectric mirrors and beamsplitters divide the light into three collinear components and a lens of 1000 mm focal length overlaps the beams in the center of the vacuum chamber close to the orifice of the slit nozzle. The crossing angle of the beams is set to 1.4° while the beam diameter is about 2 mm in front of the focusing lens defining an overlap region with the plasma produced by the slit source of ~ 22 mm in length. The setup is shown in Figure 4.14. The rest of the configuration has been identical to the one explained in [49]. Thus, the absorption spectra of N_2^+ and C_2 have been recorded, whereby the former is found to be produced in a time earlier by a factor of 10 than the later.

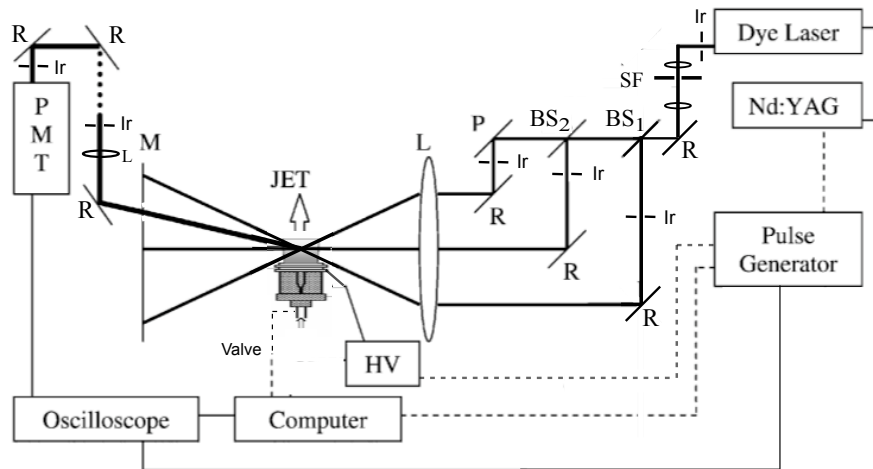


Figure 4.14: Schematic of the experimental setup used for Degenerate Four-Wave Mixing. The Nd:YAG laser is triggered electronically by a pulse generator. R represents broadband dielectric reflectors, P is a prism, BS_1 is a 70:30 and BS_2 is 50:50 broadband beamsplitter, SP represents spatial filters, L is lens, Ir is iris and M is a mask. The pulse generator triggers the oscilloscope which sends data to a computer. Control of the timing between lasers, valve opening and the high-voltage (HV) pulse applied on the source electrodes is done by the pulse generator via a computer analogical card. The signal travels along a 4-meter path consisting of spatial filters, resulting in efficient elimination of scattered light and emission from plasma.

4.2.3 Results and discussion

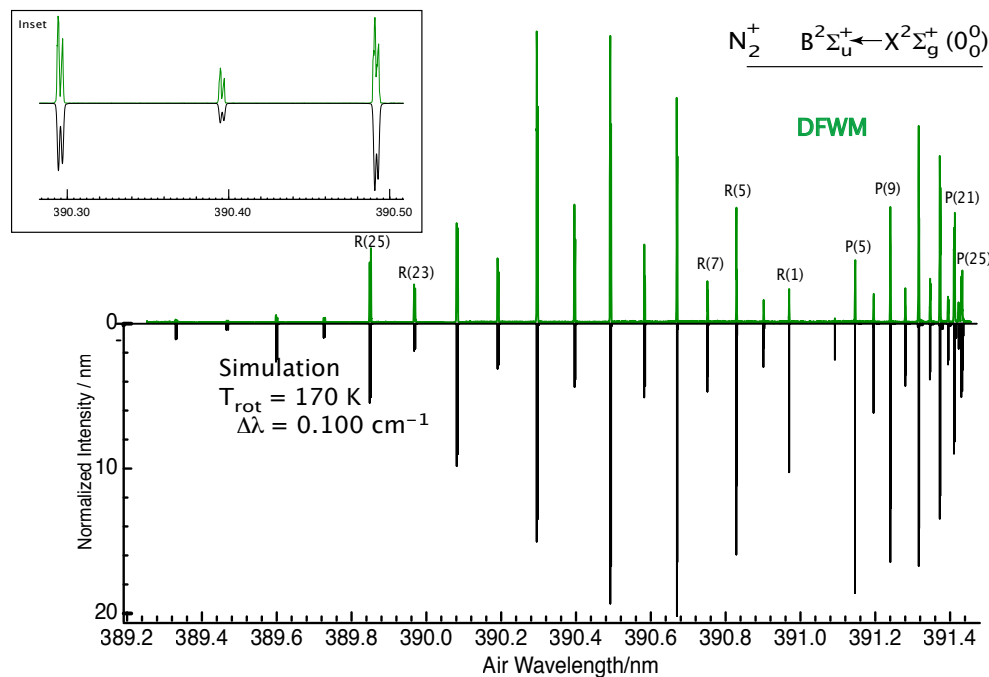


Figure 4.15: $0-0$ band of the $B^2\Sigma_u^+ \leftarrow X^2\Sigma_g^+$ electronic transition of N_2^+ measured by degenerate four-wave mixing. The simulation indicates a rotational temperature of 170 K. The signal-to-noise ratio observed is 10^3 for the strongest transitions. The inset contains a magnified portion to show the rotational lines with resolved doubling.

Detection of the origin band of $B^2\Sigma_u^+ - X^2\Sigma_g^+$ transition of N_2^+ A strong FWM signal is observed when the laser is tuned to the origin band of the $B^2\Sigma_u^+ \leftarrow X^2\Sigma_g^+$ electronic transition of N_2^+ . The spectrum obtained is shown in Figure 4.15. The absorption spectrum is the blue degraded $0-0$ transition of the first negative band of the nitrogen ion with the origin at 391.03 nm [51]. A large number of rotational lines have been observed. The pgopher software using a Boltzmann distribution of rotational level population has been used to produce the simulation. The spectroscopic constants from [52] have been taken and a rotational temperature of 170 K was assumed for the simulation. The experimental spectrum matches perfectly the simulated one. The comparison between the two provides both N_2^+ ion density and the rotational temperature (T_r) in the $X^2\Sigma_g^+$ ground state and the $B^2\Sigma_u^+$ excited state. N_2^+ ion density as low as 10^9 ions cm^{-3} in the discharge could be easily measured.

The spectral profile of individual lines is well reproduced with a FWHM Gaussian of 0.1 cm^{-1} (1.5286 pm) and Lorentzian of 0.005 cm^{-1} (0.076 pm). The calculated Doppler width of the rotational lines of N_2^+ is $\sim 0.748 \text{ pm}$, i.e., 0.0489 cm^{-1} at 170 K. The DFWM signal detected amounts to $S/N > 10^3$ for the strongest transitions. With S/N of about 10^4 for DFWM, the sensitivity of this setup is estimated to be $10^9 \text{ ions cm}^{-3}$. The maximum absorbance of 6% is observed in the P branch. The factor of 2 alternation in the intensity of the even rotational lines compared with the odd ones, due to the nuclear spin statistics [53] is not exactly reproduced as in the simulation. This is indicative of the absorption saturation phenomenon at the experimental conditions used. A clear progression in the rotational line doublets is observed in the high J transitions of the P and R branch due to the spin multiplicity [51]. Several rotational lines have been identified and indicated in the Figure 4.15. For high laser powers (several hundreds of μJ) saturation of the spec-

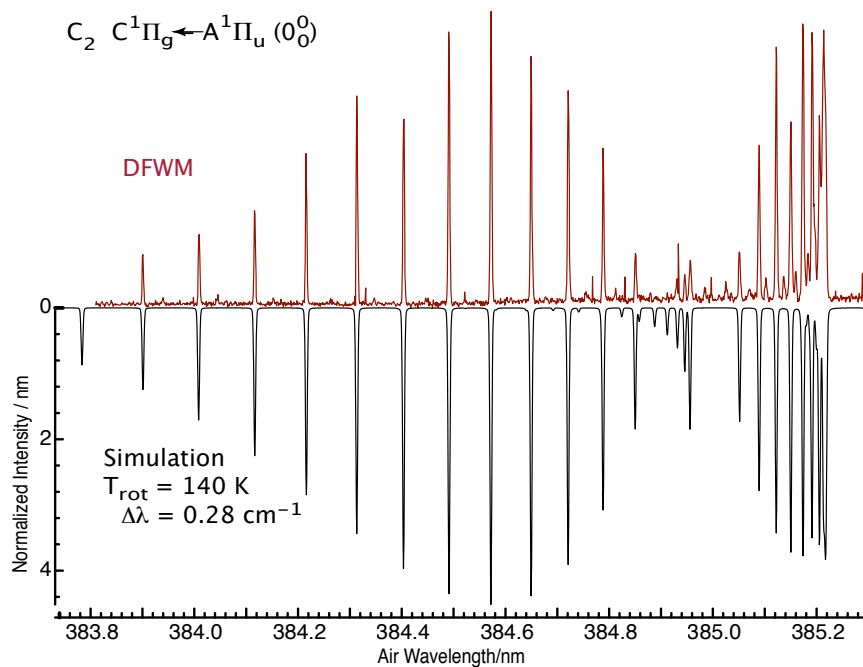


Figure 4.16: 0-0 band of the $C^1\Pi_g \leftarrow A^1\Pi_u$ electronic transition of C_2 measured by degenerate four-wave mixing. The simulation indicates a rotational temperature of 140 K.

trum was observed. The spectrum would then display a broad envelope, showing no rotational structure. When the laser-power intensity is reduced (to 20-100 μJ) different

branches could be easily resolved. The spectrum is recorded near the nozzle slit, where the temperature of the radicals is higher. At the higher resolution achieved with an intracavity etalon, the intensity and line positions in the scan obtained (Figure 4.15) is found to be in good agreement with the simulation. For these preliminary measurements, the rms of the fitted experimental line positions is 0.02 cm^{-1} , which is smaller than the laser linewidth. About 46 lines are used in the fit with J up to 14.5 in the P branch.

Detection of $A^1\Pi_u \rightarrow C^1\Pi_g$ transition of C_2 The origin of this transition is 385.06 nm, which is readily detected within the spectral region of the dye. The 0-0 band obtained is shown in Figure 4.16, with a rotational temperature of 140 K. The spectral profile of individual lines is reproduced with a Gaussian of 0.25 cm^{-1} and Lorentzian of 0.03 cm^{-1} , FWHM. This demonstrates the potential of DFWM on probing different radicals produced in the same region of the plasma. The radicals can be, even, at different rotational temperatures. The spectra of the different radicals can be obtained by just varying the delay between the probe beam and the discharge pulse.

4.2.4 Conclusion

In this chapter four wave mixing spectra of C_2 and for the first time, of a cation N_2^+ produced in a slit-jet discharge were presented. A coherent beam which can be discriminated from laser scattering and plasma emission results in high S/N spectra and a high DFWM sensitivity. It has been applied to obtain the $B^2\Sigma_u^+ \leftarrow X^2\Sigma_g^+$ system of N_2^+ along with $C^1\Pi_g \leftarrow A^1\Pi_u$ electronic transition of C_2 with the same configuration with a slight adjustment of the alignment. This shows the versatility of the technique for the detection of radicals over a wide range. The technique provides a spectroscopic tool to facilitate the unambiguous assignment while offering the possibility of disentangling the overlapping components using TC-RFWM which is a modified version of DFWM.

4.3 Detection of HC_2S

4.3.1 Introduction

The $A\ ^2\Pi_i - X\ ^2\Pi_i$ electronic transition of HC_2S has been extensively investigated experimentally by means of several techniques as well as theoretically. This radical has attracted interest because of the identification of sulfur containing carbon chains by radio astronomy [60, 61, 62]. Furthermore, it is a tetra-atomic molecule exhibiting the Renner-Teller effect for which a theoretical framework has been developed. It is thus a suitable candidate for testing the theory. Its spectrum was first reported by the flash photolysis of thiophene. Rotational parameters (B_{eff} and D_0) were inferred from emission spectra obtained between 390 and 450 nm in a radio-frequency discharge [63]. Spin-orbit calculations were made taking Renner-Teller interactions into account [64]. The ground state was studied in a slit-jet supersonic discharge by fluorescence [65] and dispersed fluorescence [66]. Effective Hamiltonian matrix calculations were carried [67] out for a tetra-atomic molecule (including Renner-Teller coupling terms, bending mode anharmonicity, spin-orbit coupling, and Fermi resonance interactions) in order to shed light on the complex ground state vibrational structure of this radical. Another study was able to retrieve the ν_4 and ν_5 bending mode harmonic frequencies from microwave spectroscopic data as well as other constants.

Rotationally resolved spectra of HC_4S have already been reported [68]. These initial experiments clearly established that the ground state of this radical is linear of 2Π symmetry with inverted spin sublevels. In addition the microwave spectra allowed an accurate determination of the effective molecular constants for the ground state including hyperfine parameters. Optical spectroscopy of HC_4S was reported with LIF characterization of HC_4S and DC_4S in a free jet environment [69]. The observed bands are due to the $^2\Pi_{3/2} - ^2\Pi_{3/2}$ component. Band origins and effective rotational constants have been determined for both isotopologues. The analysis yielded effective rotational constants for several vibrational states of the upper electronic state. Recently ground-state vibrational levels of HC_4S have been the focus of a dispersed fluorescence study from single vibronic levels [70].

In order to gain further insight into the low-lying ground state levels of ${}^2\Pi_{3/2}$ symmetry we have obtained rotationally resolved spectra by using TC-RFWM. The high selectivity of the optical-optical double-resonance method permits the unambiguous assignment of rovibronic DUMP transitions occurring upon specific excitation of one or a few overlapping rotational transitions in the origin band of the A ${}^2\Pi_{3/2}$ - X ${}^2\Pi_{3/2}$ system. The DUMP transitions observed are between the vibrationless A ${}^2\Pi_{3/2}$ state and low-lying vibrational levels (388-582 cm^{-1}) of the X ${}^2\Pi_{3/2}$ ground electronic state of HC₄S. We also report similar measurements of the 0-0 band of the A ${}^2\Pi_{3/2}$ - X ${}^2\Pi_{3/2}$ electronic transition of HC₂S. Effective rotational constants were determined for the levels observed previously by dispersed fluorescence.

4.3.2 Experimental setup

The slit of the discharge source is 30 mm \times 1 mm in size and a negative potential of 1.2 kV is applied to the electrodes separated by a distance of approximately 1 mm. Refer to Figure 4.14. Backing pressures of 5-10 bar were used and the pressure in the chamber is 0.05 mbar. The timing between the two lasers, the opening of the valve and the discharge voltage were controlled by a fast electronic delay generator. These timings were critical for the efficient production of the HC₂S and HC₄S radicals, which were generated by using a C₂H₂/CS₂/Ar (1%/0.5%/98.5%) mixture as precursor. The discharge pulse length was in the range 0.3-3 μs , resulting in a short but intense pulse of radicals. A dye laser with an intracavity etalon is used in conjunction with a double grating dye laser pumped with the 355 nm output of two Nd:YAG lasers. Frequency calibration is achieved with a wavemeter. The spectral bandwidth of the two laser sources was around 0.05 cm^{-1} . For DFWM, one of the lasers was split into three different components of equal intensities by broadband beamsplitters and sent into the vacuum chamber in a BOXCAR configuration [71] using broadband dielectric mirrors. The energy of the lasers used for recording the spectra was hundreds of μJ to 1 mJ per pulse and after attenuation using neutral density filters. For TC-RFWM, the third beam was replaced by the second laser beam (probe) and scanned in frequency as the pump laser remained at a fixed wavelength. A series

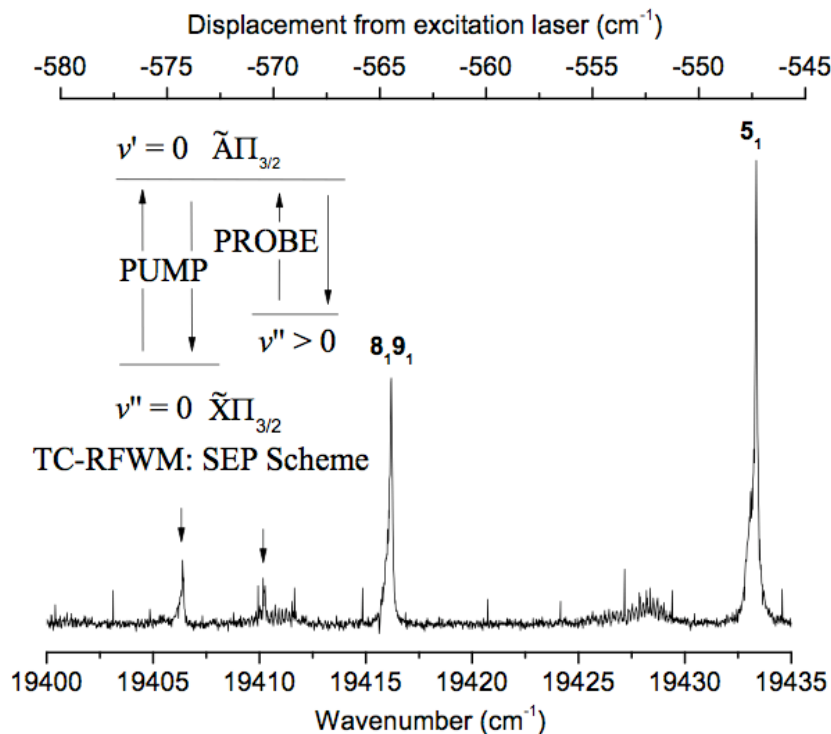


Figure 4.17: Two-color resonant four-wave mixing spectrum. Several R-transitions in the band-head of the $0_0^0 \ ^2\Pi_{3/2} - \ ^2\Pi_{3/2}$ of HC_4S transition are simultaneously excited by tuning the PUMP laser to the bandhead of the origin band at 19982.58 cm^{-1} . By scanning the dump laser an overview of the ground state vibrational levels in the vicinity of 5_1 is observed. The two arrows show unassigned bandheads.

of spatial filters and irises were used to obtain the beam with a Gaussian TEM_{00} profile ($\sim 1 \text{ mm}$ waist). In the detection arm, a 6-m pathlength lined with irises and spatial filters helped reject the stray radiation against the signal beam which is coherent and collimated, resulting in nearly background-free spectra. The signal was detected with a UV photomultiplier. Special masks were used to position the three beam crossing angles (which were around 1.4°) in order to satisfy the phase-matching condition (Bragg condition) [72]. In order to maximize signal production, the pump beams were positioned so that the optically induced fringes were directed along the flow of molecules in the supersonic expansion [72]. The signal was digitized by a fast oscilloscope and averaged during 2-3 seconds for every single point of the spectrum.

4.3.3 Results and discussion

The A $^2\Pi_{3/2}$ - X $^2\Pi_{3/2}$ transition of HC₄S: TC-RFWM

Guided by previous rotationally resolved DFWM experiments on the origin band and the dispersed fluorescence data [70] we have obtained rotationally resolved double-resonance spectra by applying the TC-RFWM technique. After exciting known rotational transitions in the 0_0^0 band of the A $^2\Pi_{3/2}$ - X $^2\Pi_{3/2}$ transition with the PUMP beams, the DUMP (or probe) laser is scanned in the vicinity of the 51 vibrational level of the electronic X $^2\Pi_{3/2}$ ground state. An overview is obtained by tuning the PUMP laser to the bandhead at 19982.58 cm^{-1} thus exciting several transitions in the R-branch ($J = 15.5\text{-}40.5$) and scanning the DUMP laser between 19400 and 19435 cm^{-1} . The rotationally resolved spectrum observed is shown in Figure 4.17. Three dominant features are observed which are dis-

Table 4.1: Results for the rotational fits of the bands originating from the ground state in the $^2\Pi_{3/2}$ - $^2\Pi_{3/2}$ electronic transition of HC₂S and HC₄S.

Label	$T_{0\nu}$	B''_{eff}	Residuals $\times 10^{-2}$	ΔE	Assignment	$(B''_{\nu} - B''_0) \times 10^{-3}$
HC ₄ S						
	19414.61(1)	0.047946(11)	0.7	566.07	$8_1 9_1$	0.14(1)
	19431.68(1)	0.047861(3)	0.6	549.00	5_1	0.05(1)
HC ₂ S						
24	22556.95(1)	0.19617(9)	2.8	1742.56	$4_2 5_2$	0.39(9)
23	22587.24(1)	0.19731(2)	0.6	1712.26	$3_1 4_2$	1.54(2)
20	22648.56(1)	0.19683(3)	1.5	1650.95	$3_1 4_1 5_1$	1.06(3)
19	22680.750(3)	0.19671(1)	0.8	1618.76	$4_3 5_1$	0.93(1)
18	22703.09(1)	0.19582(5)	2.7	1596.41	3_2	0.04(5)
16	22746.69(1)	0.19559(5)	2.7	1552.81	$3_1 4_1 5_1$	-0.19(5)
14	22784.75(1)	0.19672(4)	1.8	1514.76	4_2	0.94(4)
13	22792.09(1)	0.19665(5)	1.4	1507.41	$3_1 5_2$	0.87(5)
12	22800.31(1)	0.19682(4)	0.9	1499.19	$4_2 5_2$	1.04(4)
11	22845.93(1)	0.19715(2)	0.8	1453.58	$4_1 5_3$	1.37(2)
6	23429.14(1)	0.19693(8)	2.5	870.36	4_2	1.15(8)
5	23477.25(1)	0.19586(4)	2.6	822.25	$4_1 5_1$	0.08(4)
4	23523.05(1)	0.19558(3)	1.9	776.46	3_1	-0.21(3)
2	23623.53(1)	0.19614(4)	1.2	675.97	5_2	0.36(4)

placed from the pump laser frequency by 549.23 , 566.40 and 576.18 cm^{-1} . Each peak dis-

plays, in addition, another feature with rotational substructure displaced to the red by ~ 5 cm^{-1} . As has been discussed (Figure 7 in [49]), the analogous excitation of the bandhead and subsequent scanning in the region of the origin band yields a rotational structure which is similar to the bands observed in Figure 4.17. Thus, we assign the features in the SEP spectrum to three parallel transitions that occur from the excited rotational levels in the $0_0 A^2\Pi_{3/2}$ state. Based on the previous dispersed fluorescence measurements, we attribute the observed rotational structures around 19430 cm^{-1} and 19412 cm^{-1} to the 5_0^1 and $8_1^0 9_1^0$ transitions, respectively. The fitted effective rotational constants are presented in Table 4.1.

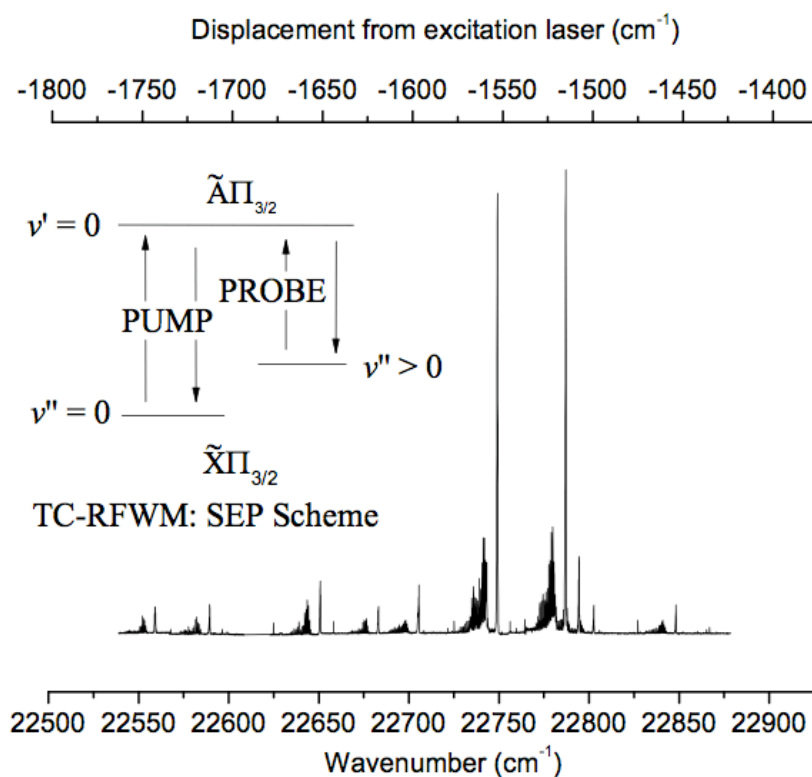


Figure 4.18: Rotationally resolved stimulated emission pumping by two-color four-wave mixing trace near 22700 cm^{-1} , recorded in the vicinity of the 5_2^0 vibronic $^2\Pi_{3/2} - ^2\Pi_{3/2}$ transition of HC_2S .

Rovibronic levels of the A $^2\Pi_{3/2}$ - X $^2\Pi_{3/2}$ electronic transition of HC₂S

The pump laser is tuned to the bandhead of the A $^2\Pi_{3/2}$ - X $^2\Pi_{3/2}$ origin electronic transition. Figure 4.18 gives an overview of the spectrum recorded when the probe laser is scanned in a 350 cm^{-1} range located around the 4_2 vibronic feature. The third major peak

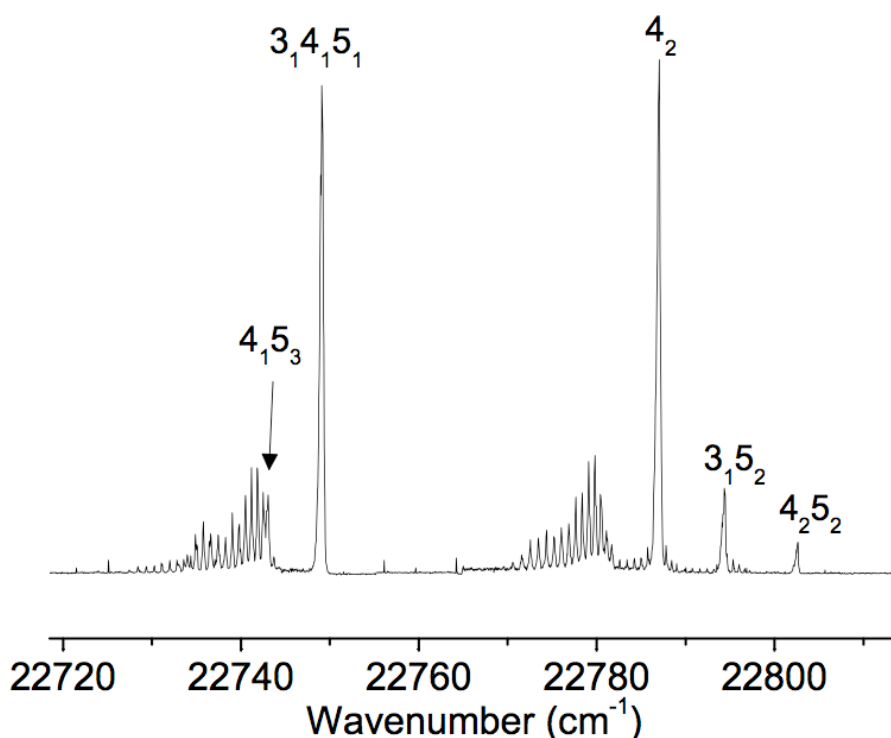


Figure 4.19: Portion of the high resolution scan showing several ground state rovibronic features of HC₂S by two-color four-wave mixing. The pump laser is set on the bandhead of the $^2\Pi_{3/2}$ - $^2\Pi_{3/2}$ origin band. Notice the high S/N ($\sim 10^3$) achieved by the method enabling to carry out a fit on the weakest features like the $4_2 5_2$ band.

at $\sim 19406\text{ cm}^{-1}$, displaced 576 cm^{-1} from the origin, has also been observed by dispersed fluorescence but could not be definitely assigned. It has been suggested to correspond to a lower Renner-Teller component of a higher bending vibration. A weaker, unassigned component at $\sim 19410\text{ cm}^{-1}$ not previously reported by LIF was also present.

The phase matching condition [72] requires that the incident beams subtend different angles as the probe is scanned in frequency. However, in practice, a small phase mismatch is permitted and a phase-matching bandwidth of $\sim 900\text{ cm}^{-1}$ is achievable with our setup without major realignment. A high S/N ratio is achieved on the stronger transitions (\sim

10^3) because of the inherent background-free character of the FWM technique, enabling an accurate determination of line positions. In addition, the ground vibronic levels are rotationally resolved, as displayed on Figure 4.19. For these measurements, the intracavity etalon was removed from the pump laser, enabling a larger number of excited transitions. This resulted in the observation of ~ 13 lines in the P branch, namely $P_1(7.5-19.5)$. For these measurements, the intracavity talon is removed from the pump laser, enabling a larger number of excited transitions. This resulted in the observation of ~ 13 lines in the P branch, namely $P_1(7.5-19.5)$.

The results of the rotational fits are shown in Table 4.1 for the observed ground state vibrations, with the pump beam set on the R branch (bandhead) of the $A^2\Pi_{3/2} - X^2\Pi_{3/2}$ origin. The rotational constants in the $A^2\Pi_{3/2}$ state were taken from [63] and kept fixed while B''_{eff} and T_{00} were varied. The centrifugal distortion term is kept fixed as the number of rotational transitions observed is not high enough to enable its reliable determination. Provided are more precise determinations of the vibrational frequencies than previously measured by dispersed fluorescence [66]. The rotational constants inferred in [63] for commonly detected ground state vibrations labeled 5 and 16 are in agreement with our findings to within a standard deviation. Their tentative assignment of band 16 is in disagreement with a recent study of this molecule [66]. We could not deduce a direct linear trend in the variation of the rotational constant versus the vibrational excitation rank. This is probably due to the complex Renner-Teller interaction. There are two vibronic bands (4 and 16) for which the rotational constant decrease rather than increase, relatively to the $v = 0$ vibrationless state. Both of them involve one quanta of the C-S stretching mode. A detailed theoretical *ab initio* study of the ground state vibrations of this radical will help in the analysis of the rotational constants variation with vibrational quantum numbers.

4.3.4 Conclusion

Degenerate and two-color FWM spectra were recorded and analyzed for the $A^2\Pi_{3/2} - X^2\Pi_{3/2}$ electronic transition of HC_2S and HC_4S . The high S/N ratio enables the precise determination of the line positions. Rotational constants for selected ground state vibrations

with ${}^2\Pi_{3/2}$ symmetry are determined for both radicals, the double-resonance technique providing unambiguous assignment. The position of the rovibronic bands has been determined with higher precision compared with previous studies. This work will serve as a basis for *ab initio* calculations on HC_2S in order to give a better understanding of the complex ground-state vibrational structure of the radical due to Renner-Teller coupling, spin-orbit interaction and Fermi resonances.

Bibliography

- [1] M. D. Levenson and S. S. Kano, *Introduction to Nonlinear Laser Spectroscopy*, Academic Press: Boston, 1988.
- [2] C. A. Walsh, M. Berg, L. R. Narasimhan, and M. D. Fayer, *Acc. Chem. Res.*, 1987, **20**, 120.
- [3] G. L. Richmond, J. M. Robinson, and V. L. Shannon, *Prog. Surf. Sci.*, 1988, **28**, 1.
- [4] *Persistent Spectral Holeburning: Science and Applications*, ed. W. E. Moemer, Springer : New York, 1988.
- [5] M. Berg, C. A. Walsh, L. R. Narasimhan, K. A. Littau, and M. Fayer, *J. Chem. Phys.*, 1988, **88**, 1564.
- [6] H. J. Eichler, P. Gunter, and D. W. Pohl, *Laser-Induced Dynamic Gratings*, Springer-Verlag: Berlin, 1986.
- [7] M. D. Fayer, *Annu. Rev. Phys. Chem.*, 1982, **33**, 63.
- [8] J. T. Fourkas and M. D. Fayer, *Acc. Chem. Res.*, 1992, **25**, 227.
- [9] P. H. Vaccaro, *Nonlinear Spectroscopy for Molecular Structure Determination*, Blackwell Scientific, London, 1998.
- [10] S. Mukamel, *Principles of Nonlinear Optical Spectroscopy*, Oxford University Press, New York, 1995.
- [11] P. N. Butcher and D. Cotter, *The Elements of Nonlinear Optics*, Cambridge University Press, Cambridge, England, 1990.
- [12] G. Hall and B. J. Whitaker, *J. Chem. Soc. Faraday Trans.*, 1994, **90**, 1.
- [13] E. F. McCormack, S. T. Pratt, P. M. Dehmer, and J. L. Dehmer, *Chem. Phys. Lett.*, 1993, 1994, **211**, **227**, 147, 656.
- [14] M. A. Buntine, D. W. Chandler, and C. C. Hayden, *J. Chem. Phys.*, 1995, **102**, 2718.

- [15] M. A. Buntine, D. W. Chandler, and C. C. Hayden, *J. Chem. Phys.*, 1992, **97**, 707.
- [16] T. J. Butenhoff and E. A. Rohlfing, *J. Chem. Phys.*, 1992, **97**, 1595.
- [17] S. Williams, J. D. Tobiasson, J. R. Dunlop, and E. A. Rohlfing, *J. Chem. Phys.*, 1995, **102**, 8342.
- [18] W.-C. Hung, M.-L. Huang, Y.-C. Lee, and Y.-P. Lee, *J. Chem. Phys.*, 1995, **103**, 9941.
- [19] S. Williams, E. A. Rohlfing, L. A. R. Richard, and N. Zare, *J. Chem. Phys.*, 1997, **106**, 3090.
- [20] P. Thaddeus and M. McCarthy, *Spectr. Acta Part A*, 2001, **57**, 757.
- [21] T. J. Lee, A. Willetts, J. F. Gaw, and N. C. Handy, *J. Chem. Phys.*, 1989, **90**, 4330.
- [22] J. R. Flores, A. Largo-Cabrerizo, and J. Largo-Cabrerizo, *J. Mol. Struct.:Theochem.*, 1986, **148**, 33.
- [23] P. Thaddeus, *Phil. Trans. R. Soc. B*, 2006, **361**, 1681.
- [24] D. Woon, *Chem. Phys. Lett.*, 1996, **244**, 45.
- [25] P. Sorokin and J. Glowina, *Chem. Phys. Lett.*, 1995, **234**, 1.
- [26] P. Sorokin and J. Glowina, *Astrophys. J.*, 1996, **473**, 900.
- [27] J. P. Maier, G. A. H. Walker, and D. A. Bohlender, *The Astr. J.*, 2004, **602**, 286.
- [28] C. A. Gottlieb, A. J. Apponi, M. C. McCarthy, and P. Thaddeus, *J. Chem. Phys.*, 2000, **113**, 1910.
- [29] J. Fulara and J. Krelowski, *New Astr. Rev.*, 2000, **44**, 581.
- [30] C. O. Laux, R. J. Gessman, C. H. Kruger, F. Roux, F. Michaud, and S. P. Davis, *J. Quant. Spect. Rad. Trans.*, 2001, **68**, 473.
- [31] R. L. Farrow and D. J. Rakestraw, *Science*, 1992, **257**, 1894.
- [32] T. J. Butenhoff and E. A. Rohlfing, *J. Chem. Phys.*, 1993, **98**, 5460.
- [33] J. R. Dunlop and E. A. Rohlfing, *J. Chem. Phys.*, 1994, **100**, 856.
- [34] M. Tulej, M. Meisinger, G. Knopp, A. M. Walser, T. Gerber, and P. P. Radi, *J. Ram. Spectrosc.*, 2007, **38**, 1022.
- [35] E. Guiberteau, G. Bonhomme, and G. H. R. Hugon, *Surf. Coat. Technol.*, 1997, **97**, 552.
- [36] T. Ohtani, N. Ihashi, and O. Matsumoto, *Trans. Mater. Res. Soc. Japan*, 2000, **25**, 47.
- [37] N. Philip, B. Saoudi, M.-C. Crevier, M. Moisan, J. Barbeau, and J. Pelletier, *IEEE Trans. Plasma Sci.*, 2002, **30**, 1429.

- [38] P. A. Sa, V. Guerra, J. Loureiro, and N. Sadeghi, *J. Phys. D: Appl. Phys.*, 2004, **37**, 221.
- [39] M. Aldener, B. Lindgren¹, A. Pettersson, and U. Sassenberg, *Phys. Scripta*, 2000, **61**, 62.
- [40] M. Kotterer, J. Conceicao, and J. P. Maier, *Chem. Phys. Lett.*, 1996, **259**, 233.
- [41] A. Al-Khalili, H. Ludwigs, and P. Royen, *Chem. Phys. Lett.*, 1998, **284**, 191.
- [42] A. Okazaki, T. Ebata, and N. Mikami, *Chem. Phys. Lett.*, 1995, **241**, 275.
- [43] D. Y. Chen, R. W. Fan, X. J. Yang, Q. K. Zheng, and Q. Z. Qin, *Chin. Phys. Lett.*, 2004, **21**, 295.
- [44] T. J. Butenhoff and E. A. Rohlfing, *J. Chem. Phys.*, 1992, **97**, 1595.
- [45] Y. Tang and S. A. Reid, *Chem. Phys. Lett.*, 1996, **248**, 476.
- [46] T. J. Butenhoff and E. A. Rohlfing, *J. Chem. Phys.*, 1992, **97**, 1595.
- [47] Y. Tang and S. A. Reid, *Chem. Phys. Lett.*, 1998, **292**, 691.
- [48] Y. Tang, J. P. Schmidt, and S. A. Reid, *J. Chem. Phys.*, 1999, **110**, 5734.
- [49] F. J. Mazzotti, E. Achkasova, R. Chauhan, M. Tulej, P. P. Radib, and J. P. Maier, *Phys. Chem. Chem. Phys.*, 2008, **10**, 136.
- [50] F. J. Mazzotti, R. Chauhan, Z. Jamshidi, M. Tulej, P. P. Radi, and J. P. Maier, *Mol. Phys.*, 2008.
- [51] T. Gherman, E. Eslami, D. Romanini, S. Kassi, J.-C. Vial, and N. Sadeghi, *J. Phys. D: Appl. Phys.*, 2004, **37**, 2408.
- [52] F. Michaud, F. Roux, S. P. Davis, A.-D. Nguyen, and C. O. Laux, *J. Mol. Spectr.*, 2000, **203**, 1.
- [53] G. Herzberg, *Molecular Spectra and Molecular Structure I. Spectra of Diatomic Molecules*, New York:Van Nostrand Reinhold, 1950.
- [54] T. M. Tulej, M. Meisinger, G. Knopp, A. M. Walser, P. Beaud, T. Gerber, and P. Radi, *J. Ram. Spectrosc.*, 2006, **37**, 680.
- [55] F. D. Teodoro and E. M. Cormack, *J. Chem. Phys.*, 1999, **110**, 8369.
- [56] M. Tulej, M. Meisinger, G. Knopp, A. M. Walser, P. Beaud, T. Gerber, and P. P. Radi, *J. Raman Spectrosc.*, 2006, **37**, 376.
- [57] T. Settersten, R. Farrow, and J. Gray, *Chem. Phys. Lett.*, 2003, **369**, 584.
- [58] P. Radi, M. Tulej, G. Knopp, P. Beaud, and T. J. Gerber, *Ram. Spectrosc.*, 2003, **34**, 1037.
- [59] A. K. Bultitude, R. Bratfalean, and P. Ewart, *J. Raman Spectrosc.*, 2003, **34**, 1030.

- [60] J. Cernicharo, M. Guelin, H. Hein, and C. Kahane, *Astron. Astrophys.*, 1987, **181**, L9.
- [61] M. B. Bell, L. Avery, and P. Feldman, *Astrophys. J.*, 1993, **417**, L37.
- [62] T. Millar, J. Flores, and A. Markwick, *Mon. Not. R. Astron. Soc.*, 2001, **327**, 1173.
- [63] B. Coquart, *Can. J. Phys.*, 1985, **63**, 1362.
- [64] A. M. Perić, L. Stevanović, and S. Jerosimić, *J. Chem. Phys.*, 2002, **117**, 4233.
- [65] H. Kohguchi, Y. Ohshima, and Y. Endo, *Chem. Phys. Lett.*, 1996, **254**, 397.
- [66] S.-G. He and D. Clouthier, *J. Chem. Phys.*, 2005, **123**, 014317.
- [67] S.-G. He and D. Clouthier, *J. Chem. Phys.*, 2005, **123**, 014316.
- [68] Y. Hirahara, Y. Ohshima, and Y. Endo, *J. Chem. Phys.*, 1994, **101**, 7342.
- [69] M. Nakajima, Y. Sumiyoshi, and Y. Endo, *Chem. Phys. Lett.*, 2002, **351**, 359.
- [70] N. Reilly, G. Cupitt, S. Kable, and T. Schmidt, *J. Chem. Phys.*, 2006, **124**, 194310.
- [71] A. Eckbreth, *Appl. Phys.*, 1978, **32**, 421.
- [72] *Nonlinear Spectroscopy for Molecular Structure Determination*, ed. R.W. Field, E. Hirota, J.P. Maier and S. Tsuchiya, Blackwell Science Ltd., 1998.

Rotationally Resolved Ground State Vibrational Levels of HC₂S Studied by Two-Color Resonant Four-Wave Mixing[†]

Richa Chauhan,[‡] Fabio J. Mazzotti,[‡] Ranjini Raghunandan,[‡] Marek Tulej,^{§,‡} Peter P. Radi,^{||} and John P. Maier^{*,‡}

Department of Chemistry, University of Basel, Klingelbergstrasse 80, CH-4056 Basel, Switzerland, and General Energy Research, Paul Scherrer Institute, CH-5232 Villigen, Switzerland

Received: October 11, 2009; Revised Manuscript Received: November 13, 2009

A high-resolution study of the $\tilde{X}^2\Pi_{3/2}$ ground state rovibronic energy levels of jet-cooled HC₂S radical using the double-resonance two-color four-wave mixing technique (TC-RFWM) is reported. The rotational structure of the bands is observed by excitation of selected R-branch lines in the origin band of the $\tilde{A}^2\Pi_{3/2}-\tilde{X}^2\Pi_{3/2}$ electronic system. The second laser frequency is scanned to transfer the population from the rotational level(s) of the upper state to selected vibronic levels of the ground state. Fourteen rotationally resolved vibrational bands have been recorded for energies up to 1800 cm⁻¹ above the $v'' = 0$ $\tilde{X}^2\Pi_{3/2}$ electronic ground state. Effective rotational constants and origins are determined for levels that involve fundamental and overtone combinations of the ν_3 (CS stretch), ν_4 (CCH bend), and ν_5 (CCS bend) vibrations. This illustrates the power and advantages of the TC-RFWM approach for the study of the ground state manifold of reactive intermediates produced in low concentrations with high resolution, good signal-to-noise and wide dynamic range.

I. Introduction

The resonant four-wave mixing (RFWM) technique has been recently applied to spectroscopic investigations of charged and neutral species generated in a supersonic discharge.^{1–3} The detection limit of $\sim 10^8$ molecules cm⁻³ or lower determined in these studies is comparable to that achieved for laser induced fluorescence (LIF) or cavity ring-down spectroscopy (CRDS) rendering the RFWM technique highly competitive.^{1,2,4} Compared to linear methods, the application of RFWM can be advantageous due to complementary capabilities.^{2,5} The high signal-to-noise ratio stems from the fully resonant processes involved and from an essentially background-free signal. Furthermore, because the method is based on molecular absorption, it is not dependent on the lifetime of the upper level and is consequently applicable to the detection of predissociative or short-lived excited states.^{6–8} The nonlinear character of the coherent method introduces the quadratic scaling of the signal intensity with species number density.⁹ This is considered as a limitation of its sensitivity but leads also to a high dynamic range of the RFWM response. RFWM has been exploited in a variety of environments including flames, low-pressure gases and to a lesser extent in supersonic free-jet expansions.^{10–12}

The paper presents the spectroscopic study of the ground state energy levels of HC₂S radical. It shows that the RFWM can be a superior method for studying the molecular structure in the ground state. From the analysis of the rotationally resolved spectra new structural parameters are determined for a number of vibrational energy levels. The unambiguous spectroscopic assignment can be prepared in a straightforward manner using intermediate level labeling. We show that the approach is applicable to the species present in low concentrations and the

spectra can be measured with a high signal-to-noise ratio due to a fully resonant process. The method is background free in contrast to absorption techniques where a weak signal need to be extracted from a large, fluctuating one. The laser-like signal is detected due to coherent character of the four-wave mixing process and the signal beam can be probed remotely without significant loss, reducing background due to stray light. This approach shows the potential of providing a detailed insight to the spectroscopic pattern in the ground state manifold. An access to high lying energy levels in the ground state can also be useful in studies of the reactive properties of transient species such as unimolecular dissociation.

The investigations discussed here utilize a two-color variant of resonant four-wave mixing (TC-RFWM) resulting in a stimulated emission pumping (SEP) type experiment. Classically, the SEP method is based on optical–optical double-resonance involving two laser beams.^{13,14} The first beam (PUMP) transfers population from an initial ground state to a specific level in the electronic excited state while a second beam (DUMP) is used to bring the population back to the ground state manifold. The common SEP detection relies on the competition between spontaneous and stimulated emission by the DUMP laser and results in a small decrease in fluorescence (fluorescence-dip) signal. Only fluorescing molecules can be studied using this technique. In contrast, TC-RFWM does not rely on fluorescing molecules and provides often superior signal-to-noise ratios. The signal is generated by a nonlinear process coupling three input laser beams (2 PUMP and 1 DUMP) that are (i) resonant with two molecular transitions, (ii) share a common (upper) level, and (iii) satisfy the phase matching condition. The double-resonance feature offers a high selectivity for species detection. In addition, intermediate level labeling simplifies complex and congested one-color spectra, allowing precise measurements of line positions and, in most cases, a straightforward assignment of the observed transitions. However, the technique is sensitive to alignment and requires a high quality laser spatial profile as well as good control of beam

[†] Part of the “Benoît Soep Festschrift”.

* Corresponding author. E-mail: j.p.maier@unibas.ch.

[‡] University of Basel.

[§] Present address: Institute of Physics, Planetology and Space Research, University of Bern, Sidlerstr. 5, CH-3012 Bern, Switzerland.

^{||} Paul Scherrer Institute.

intensities to avoid broadening of the molecular transitions due to saturation effects. A variety of theoretical investigations of TC-RFWM can be found in the literature including discussion of the polarization-based schemes and saturation effects.^{15–18} The derivation of the signal intensities based on diagrammatic perturbation theory was particularly well tested experimentally.^{15,19,39}

The interest in HC₂S stems from its importance in interstellar chemistry. A number of sulfur containing carbon chains have been detected by millimeter-wave techniques in star forming regions and in circumstellar envelopes²⁰ and their importance in understanding physical conditions in these regions was discussed.²¹ Although HC₂S has not been yet detected in space, it is expected to be an important intermediate for the formation of large sulfur-containing molecules.²² Two bimolecular reactions are proposed to contribute to the synthesis of HC₂S under interstellar conditions: the sulfur cation with acetylene and the carbon dimer with H₂S.^{22,23}

HC₂S has been extensively studied by spectroscopy. Since its first detection via the $\tilde{A}^2\Pi-\tilde{X}^2\Pi$ electronic transition in flash photolysis of thiophene,^{24,25} HC₂S has attracted considerable attention by experiment and theory. It is an example of a tetraatomic molecule that exhibits a complex coupling of the spin-orbit and Renner-Teller effects. In this context, a number of experimental and theoretical approaches were applied to study the vibrational and rotational structure of this molecule in both the ground and excited state. The ground state structural parameters determined initially from the emission spectra studied in the range 390–450 nm²⁶ have been improved by millimeter-wave spectroscopy for several vibrational bands including the ν_4 and ν_5 bending modes frequencies.^{27,28} The extensive studies by dispersed fluorescence have provided the spin-orbit splitting of 259 cm⁻¹ in the ground state and the vibrational energy levels up to 1700 cm⁻¹.²⁹ The excited state of HC₂S was investigated by LIF yielding complex rovibrational structure.^{30,31} In parallel, theoretical studies attempted to combine spin-orbit with Renner-Teller interactions to explain the experimental findings.^{32,33} Effective Hamiltonian calculations were carried out to shed light on the complex ground state vibrational structure of this radical.^{34,35} In model calculations accompanying the LIF studies it has been shown that the large Renner-Teller effect observed in the excited state and the different HCCS and DCCS excited state zero-point spin-orbit splitting can be explained with the assumption of a quasilinear excited state geometry.³¹ In spite of considerable advances made in the understanding of the spectral complexity of HC₂S, the theoretical approaches developed so far do not offer an unambiguous explanation of all features observed.³³

In this paper, the structure of the $\tilde{X}^2\Pi_{3/2}$ ground state of the HC₂S radical is further characterized by measuring rotationally resolved spectra of vibrational levels by TC-RFWM. Due to the high sensitivity of the method 14 excited vibrational states could be observed in the ground state manifold, 650–1800 cm⁻¹ above the $\nu'' = 0$ $\tilde{X}^2\Pi_{3/2}$ level. The selectivity of the optical-optical double-resonance method permits an unambiguous assignment based on intermediate level labeling and yields effective rotational constants and band origins.

II. Experimental Setup

The HC₂S radical was produced by a slit-jet discharge.³⁶ The slit length was 30 mm × 1 mm and -1000 V was applied to the electrodes, which were separated by 2 mm. The discharge pulse length was 3–10 μ s, resulting in a short but intense pulse of radicals. During the operation of the assembly at 10 Hz, a pressure in the source chamber of approximately 0.05 mbar was

maintained by the vacuum system for a backing pressure of 5–10 bar. The timing between the two lasers, the triggering of the valve and the discharge voltage were controlled by a fast electronic delay generator. These timings are critical for the efficient production of HC₂S which was generated by using a C₂H₂/CS₂ (1%/0.5%) mixture in argon as precursor. The optical configuration used has also been described.³ Two separate Nd:YAG pumped dye lasers were used, one with an intracavity etalon and the other with a double grating. The spectral bandwidth of the two laser sources was around 0.05 cm⁻¹. Frequency calibration was achieved by a wavemeter with an accuracy of 0.002 cm⁻¹. For degenerate four-wave mixing, one of the lasers was split into three components of equal intensities by broadband beam splitters and sent into the vacuum chamber in a BOXCARS configuration.³⁷ The output energy of the lasers used was attenuated with neutral density filters. In case of TC-RFWM measurements, the third beam was replaced by the output of the second laser (probe or DUMP) and scanned in frequency as the PUMP laser remained at a fixed wavelength. The signal beam, which is coherent and collimated in nature, was separated from the stray radiation by a 6 m detection arm consisting of several irises and spatial filters to obtain nearly background-free spectra. The signal was detected with a photomultiplier. Special masks were used to position the three beam crossing angles ($\sim 1.4^\circ$) to satisfy the phase-matching condition $k_1 + k_3 = k_2 + k_4$, where the wave vectors k_1 , k_2 (PUMP), and k_3 (probe) generate the signal beam wave vector k_4 .⁹ The PUMP beams were positioned such that the optically induced fringes were directed along the flow of molecules in the supersonic expansion.⁷ The polarizations of the three beams were vertical in the laboratory frame. The signal was digitized by a fast oscilloscope and averaged for 2–3 s for every scan step of the spectrum.

III. Results and Discussion

Initial experiments were performed by applying DFWM spectroscopy on the origin band of the $\tilde{A}^2\Pi_{3/2}-\tilde{X}^2\Pi_{3/2}$ transition of HC₂S. The spectrum is reproduced in Figure 1 and shows a well resolved P-branch and a heavily congested R-branch. A least-squares fit to the resolved line positions by means of the PGOPHER program³⁸ was carried out by constraining the rotational and centrifugal distortion constants

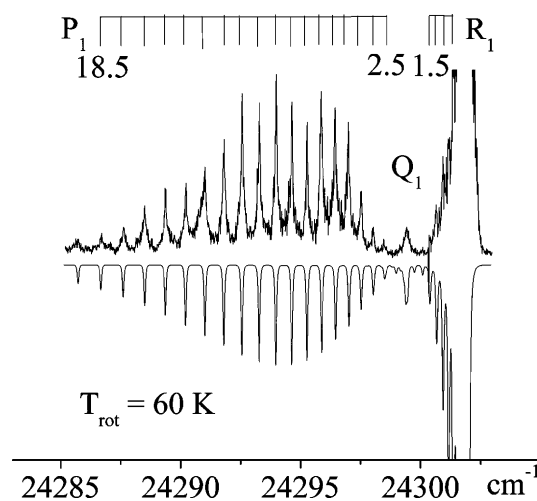


Figure 1. Rotationally resolved DFWM spectrum of the origin band of the HC₂S $\tilde{A}^2\Pi_{3/2}-\tilde{X}^2\Pi_{3/2}$ electronic system. The inverted trace is the square of the PGOPHER simulation, assuming a Lorentzian line shape (0.1 cm⁻¹ fwhm) and a rotational temperature of 60 K.

of the $\tilde{A}^2\Pi_{3/2}$ state to the values given in ref 26. The spectroscopic constants found in the previous measurement,²¹ such as the rotational constant of the lower state, $B_0'' = 0.195\,693(11)\text{ cm}^{-1}$ and the origin at $T_{00} = 24\,299.4430(20)\text{ cm}^{-1}$ were confirmed. The low J -numbers observed for the jet-cooled radicals prevent an accurate determination of the quartic centrifugal distortion constant, which therefore was fixed at $2.4 \times 10^{-8}\text{ cm}^{-1}$. A simulated DFWM spectrum at a rotational temperature of approximately 60 K is shown inverted in Figure 1. The excellent agreement with the published values validates the procedure for the evaluation of rotational constants and band origins and will be applied in the following for the rotational analysis of higher lying vibrational levels measured by TC-RFWM.

Rotationally resolved double-resonance spectra were obtained by applying the TC-RFWM technique. The pump beams were tuned to known rotational transitions in the 0_0^0 band of the $\tilde{A}^2\Pi_{3/2}-\tilde{X}^2\Pi_{3/2}$ electronic system, exciting well-defined rotational states of the upper level (intermediate level labeling). Subsequently, with the pump laser frequency fixed, the dump (or probe) beam was scanned in the range of selected vibronic bands in the ground state that share a common upper level with the pumped $v' = 0$ state. Note that the phase matching conditions⁹ are met exactly only for one combination of the pump and dump frequencies. Scanning the latter causes a phase mismatch, which reduces the signal intensity. However, in practice, the effect can be neglected and a range of $\sim 900\text{ cm}^{-1}$ is achievable without major realignment.⁷ The observed TC-RFWM spectra display excellent signal-to-noise ratios up to $\sim 10^4$ for the stronger transitions and allow an accurate determination of line positions. Furthermore, the expected simplification by the double-resonance selection rules reduces ambiguities for the assignment that occur in the one-color spectrum where overlapping transitions are frequently present.

Figure 2 exemplifies the method and the assignment procedure for rotational transitions. The frequency of the pump laser at $24\,295.21\text{ cm}^{-1}$ corresponds to the $P_1(8.5)$ transition of HC₂S in the origin band of the $\tilde{A}^2\Pi_{3/2}-\tilde{X}^2\Pi_{3/2}$ electronic transition. By scanning the probe laser over the same band, we obtain a nearly degenerate two-color four-wave mixing spectrum (upper trace). Alternatively, the probe laser is scanned around 23520 cm^{-1} , addressing the vibrational level of the ground state exhibiting one quantum excitation in ν_3 (lower trace). The resonant lines consist of the $P_1(8.5)$, $R_1(6.5)$, and $R_1(8.5)$ transitions according to the insets in the figure. A minor contribution of a neighboring transition of the pumped $P_1(8.5)$ in the origin band is observed in the lower trace. In fact, $P_1(9.5)$ is simultaneously excited due to saturation broadening and yields the “satellite” transitions $P_1(9.5)$ and $R_1(7.5)$ in the 3_1^0 band. TC-RFWM is thus able to characterize the high lying vibrational levels in the $\tilde{X}^2\Pi_{3/2}$ state of the supersonically cooled radical by SEP type approach.

As was demonstrated previously,³ a convenient way of using TC-RFWM is to tune the pump laser to the band head where numerous rotational levels are excited concomitantly due to overlapping transitions. A scan of the probe laser yields then several resonant transitions to the ground rotational level(s) in a single spectrum. Figure 3 displays an example of TC-RFWM spectra obtained by pumping the band head of the origin transition at $24\,301.9\text{ cm}^{-1}$. For these experiments it is advantageous to remove the intracavity etalon of the laser to broaden the bandwidth to approximately 0.15 cm^{-1} and to excite, therefore, a broad range of P-branch transitions simultaneously

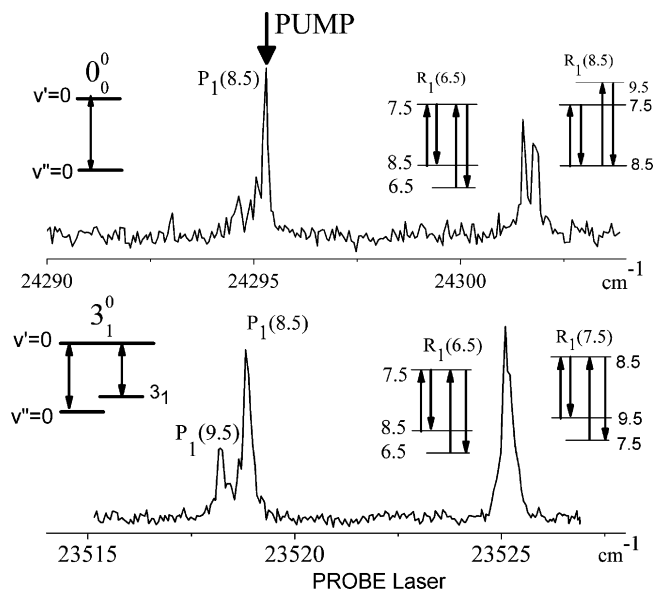


Figure 2. TC-RFWM spectrum. The pump frequency was fixed on the $P_1(8.5)$ transition of the origin band of the $\tilde{A}^2\Pi_{3/2}-\tilde{X}^2\Pi_{3/2}$ transition (PUMP). The probe was scanned through the origin (upper trace) and 3_1^0 (lower trace) bands. The nearly degenerate TC-RFWM (upper trace) displays three transitions: the degenerate transition at $P_1(8.5)$ and two R_1 transitions sharing the upper and lower level ($R_1(6.5)$ and $R_1(8.5)$, respectively). The SEP spectrum connecting the $v' = 0$ $\tilde{A}^2\Pi_{3/2}$ state to the $3_1 \tilde{X}^2\Pi_{3/2}$ level only exhibits two resonant lines that share the common upper level with $J = 7.5$ and $v' = 0$. The $P_1(9.5)$ transition, and $R_1(7.5)$ which contributes to the 23535 cm^{-1} peak, are present due to saturation effects (see text).

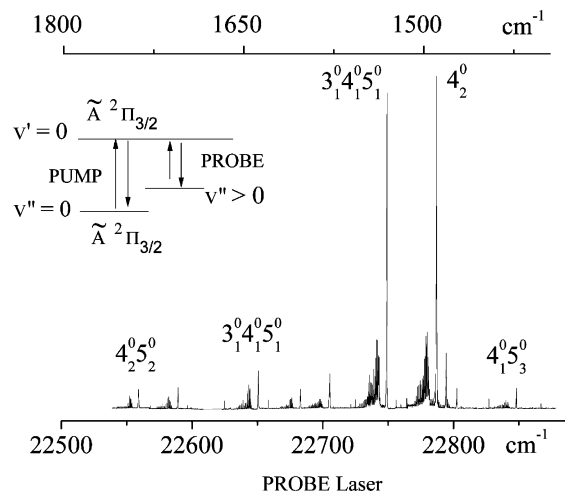


Figure 3. Rotationally resolved stimulated emission spectrum of vibrationally excited ground state levels of the $\tilde{A}^2\Pi_{3/2}-\tilde{X}^2\Pi_{3/2}$ electronic transition of HC₂S. The pump laser was set on the band-head of the $\tilde{A}^2\Pi_{3/2}-\tilde{X}^2\Pi_{3/2}$ origin and excites numerous rotational levels simultaneously. The horizontal scale (cm^{-1}) at the top shows the energy above the $v'' = 0$ $\tilde{X}^2\Pi_{3/2}$. The inset is the scheme of the double resonance approach.

($J = 9.5-21.5$). The subsequent scan of the probe laser in the vicinity of the 5_2^0 band gives rise to a large number of rotationally resolved transitions that are in resonance with the labeled states of the upper level. To avoid power broadening, the measurements have been performed at input intensities below saturation of the molecular transitions. An overview of the TC-RFWM spectrum in the range between $22\,500$ and $22\,900\text{ cm}^{-1}$ is shown in Figure 3.

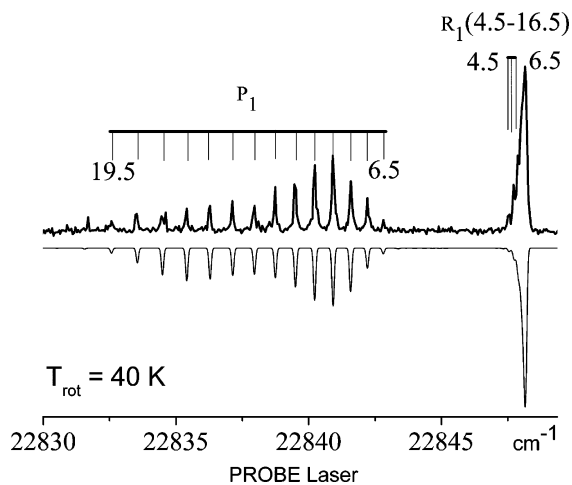


Figure 4. Vibronic structure of the transition detected by TC-RFWM. The pump was set on the bandhead of the origin band in the $\tilde{A}^2\Pi_{3/2}-\tilde{X}^2\Pi_{3/2}$ transition of HC_2S . A least-squares fit to the line positions yields the rotational constant and the vibronic origin of the band. A synthetic spectrum with the optimized molecular constants and assuming a Boltzmann distribution for a rotational population at 40 K is shown inverted (see text for details). Intensities are computed by taking into account partial saturation of the transitions.³⁹

The $4_1^0 5_3^0$ band around $22\,840\text{ cm}^{-1}$ is shown in more detail in Figure 4. The rotationally resolved band structure resembles a $^2\Pi-^2\Pi$ system with a weak Q branch. The assignment of these transitions is straightforward. Intermediate level labeling from the $\tilde{X}^2\Pi_{3/2}$ state by the pump laser yields only transitions to levels in the ground state with the same spin component $\Omega = 3/2$. If ambiguities are encountered for the assignment of specific J -levels, the method described above using a narrow bandwidth laser is applied and yields unambiguous results. The substantial signal-to-noise ratio provides accurate line positions suitable for the determination of effective rotational parameters.

A least-squares fit to the observed frequencies has been carried out using the PGOPHER program³⁸ and constraining the molecular constants in the $\tilde{A}^2\Pi_{3/2}$ state to the values of ref 26. For each recorded band, two parameters are obtained, B_{eff}'' and the band origin. Around 14 lines were used for the fit of each band. The resulting vibronic origins are determined with a 10% higher precision compared to the previous work by dispersed fluorescence.²⁹ Furthermore, rotational constants of

the ground state vibrations are determined for 14 vibrational levels of which 12 are reported for the first time. The results are summarized in Table 1. The vibrational assignment and the labeling of the bands (first column) follow the work of ref 29. As can be seen in Table 1, among the five normal modes of the linear molecule, ν_3 (CS stretch), ν_4 (CCH bend), and ν_5 (CCS bend) are obtained from the detected overtones and combination bands. The rotational constants inferred in ref 26 for the two commonly detected ground state vibrational levels (5 and 16) are in agreement with our results to within one standard deviation. However, their tentative assignment of band 16 is in disagreement with the present study. A direct linear trend in the variation of the rotational constant versus the vibrational excitation quantum number is not apparent. The finding is rationalized by considering that Renner–Teller interaction and perturbations may induce a nontrivial potential energy surface along the internal coordinates of the molecule. There are two vibronic bands (4 and 16) for which the rotational constant decrease with respect to the $v'' = 0$ state (Table 1). The energetically lowest level of them has been assigned as 3_1 and the other as the $3_1 4_1 5_1$ combination.

IV. Conclusion

Double-resonance spectroscopy by TC-RFWM offers a way to access specific vibronic levels of the ground state and to simplify the complex rotational band structure by intermediate level labeling. In the present work, TC-RFWM spectra were recorded and analyzed for the $\tilde{A}^2\Pi_{3/2}-\tilde{X}^2\Pi_{3/2}$ electronic transition of HC_2S . These are background-free, show a high dynamic range ($\sim 10^4$) and high signal-to-noise ratio for the weakest ro-vibrational bands (~ 150), enabling their accurate rotational analysis to be made. Rotational constants for selected ground state vibrations with $\tilde{X}^2\Pi_{3/2}$ symmetry were determined by taking advantage of the unambiguous assignment capability of the method. The work reports rotational constants for 14 vibronic bands. With the exception of the constants for the bands 5 and 16 in Table 1, these values are determined for the first time. An uncertainty of 0.005 cm^{-1} improves the values by a factor of 10. The present work combined with the previous results on HC_2S should be an incentive for ab initio calculations and a better understanding of the complex and overlapping ground state vibrational structure of this interesting Renner–Teller molecule.

TABLE 1: Spectroscopic Constants Determined for the Vibrationally Excited Levels in the $\tilde{X}^2\Pi_{3/2}$ Ground Electronic State of HC_2S^a

label	T_{0v}	B_{eff}''	B_{eff}'' (ref 26)	residuals ($\times 10^{-2}$)	level	$B_{\text{eff}}'' - B_0''$ ($\times 10^{-3}$)
24	1742.527(13)	0.196140(85)		2.8	$4_2 5_2$	0.45(9)
23	1712.2348(28)	0.197288(22)		0.6	$3_1 4_2$	1.59(2)
20	1650.9168(64)	0.196803(31)		1.6	$3_1 4_1 5_1$	1.11(3)
19	1618.7326(34)	0.196677(16)		0.8	$4_3 5_1$	0.98(2)
18	1596.388(11)	0.195786(53)		2.7	3_2	0.09(5)
16	1552.786(11)	0.195553(52)	0.19558(12)	2.7	$3_1 4_1 5_1$	-0.14(5)
14	1514.7266(77)	0.196683(37)		1.9	4_2	0.99(4)
13	1507.3883(81)	0.196570(55)		1.3	$3_1 5_2$	0.88(6)
12	1499.1669(78)	0.196791(43)		0.9	$4_2 5_2$	1.10(4)
11	1453.5528(37)	0.197119(22)		0.8	$4_1 5_3$	1.43(2)
6	870.334(11)	0.196899(76)		2.5	4_2	1.21(8)
5	822.228(10)	0.195820(45)	0.19595(16)	2.6	$4_1 5_1$	0.13(5)
4	776.4297(66)	0.195537(30)		1.9	3_1	-0.16(3)
2	675.9444(62)	0.19610(40)		1.2	5_2	0.41(4)

^a The labels and assignments are based on ref 13. All term values and spectroscopic constants are in cm^{-1} . Values in parentheses are one standard deviation.

Acknowledgment. This work has been supported by the Swiss National Science Foundation (Project 200020-124349/1 and 200020-115958) and the Swiss Department of Energy (BFE, Contract 100708).

References and Notes

- (1) Raghunandan, R.; Mazzotti, F. J.; Chauhan, R.; Tulej, M.; Maier, J. P. *J. Phys. Chem. A* **2009**, *113*, 13402.
- (2) Tulej, M.; Meisinger, M.; Knopp, G.; Walser, A. M.; Gerber, T.; Radi, P. P. *J. Raman Spectrosc.* **2007**, *38*, 1022.
- (3) Mazzotti, F. J.; Achkasova, E.; Chauhan, R.; Tulej, M.; Radi, P. P.; Maier, J. P. *Phys. Chem. Chem. Phys.* **2008**, *10*, 36.
- (4) Tulej, M.; Meisinger, M.; Knopp, G.; Walser, A. M.; Beaud, P.; Gerber, T.; Radi, P. P. *J. Raman Spectrosc.* **2006**, *37*, 680.
- (5) Tulej, M.; Knopp, G.; Beaud, P.; Gerber, T.; Radi, P. P. *J. Raman Spectrosc.* **2005**, *36*, 109.
- (6) Tulej, M.; Meisinger, M.; Knopp, G.; Walser, A. M.; Beaud, P.; Gerber, T.; Radi, P. P. *J. Raman Spectrosc.* **2006**, *37*, 376.
- (7) Butenhoff, T. J.; Rohlfing, E. A. *J. Chem. Phys.* **1993**, *98*, 5460.
- (8) Liu, C.-P.; Reid, S. A.; Lee, Y.-P. *J. Chem. Phys.* **2005**, *122*, 124313.
- (9) Vaccaro, P. H. In *Nonlinear Spectroscopy for Molecular Structure Determination*; Hirota, E., Field, R. W., Maier, J. P., Tsuchiya, S., Eds.; Blackwell Scientific: Oxford, U.K., 1998; p 75.
- (10) Farrow, R. L.; Rakestraw, D. J. *Science* **1992**, *257*, 1894.
- (11) Butenhoff, T. J.; Rohlfing, E. A. *J. Chem. Phys.* **1992**, *97*, 1595.
- (12) Radi, P. P.; Tulej, M.; Knopp, G.; Beaud, P.; Gerber, T. *J. Raman Spectrosc.* **2003**, *34*, 1037.
- (13) Dai, H.-L., Field, R. W., Eds. *Molecular Dynamics and Spectroscopy by Stimulated Emission Pumping*; World Scientific: Singapore, 1995.
- (14) Buntine, M. A.; Chandler, D. W.; Hayden, C. C. *J. Chem. Phys.* **1992**, *97*, 707.
- (15) Williams, S.; Tobiasson, J. D.; Dunlop, J. R.; Rohlfing, E. A. *J. Chem. Phys.* **1995**, *102*, 8342.
- (16) Williams, S.; Rohlfing, E. A.; Rahn, L. A.; Zare, R. N. *J. Chem. Phys.* **1995**, *102*, 8342.
- (17) Bracamonte, A. E.; Vaccaro, P. H. *J. Chem. Phys.* **2003**, *119*, 887.
- (18) Costen, M. L.; McKendrick, K. G. *J. Chem. Phys.* **2005**, *112*, 164309.
- (19) Hung, W.-C.; Huang, M.-L.; Lee, Y.-C.; Lee, Y.-P. *J. Chem. Phys.* **1995**, *103*, 9941.
- (20) Gordon, V. P.; McCarthy, M. C.; Apponi, A. J.; Thaddeus, P. *Astrophys. J. Suppl.* **2002**, *138*, 297, and references therein.
- (21) Minh, Y. C.; van Dishoeck, E. F. *From Molecular Clouds to Planetary Systems* **2000**, 197.
- (22) Yamada, M.; Osamura, Y.; Kaiser, R. I. *Astron. Astrophys.* **2002**, *395*, 1031.
- (23) Smith, D.; Adams, N. G.; Giles, K.; Herbst, E. *Astron. Astrophys.* **1988**, *200*, 191.
- (24) Krishnamachari, S. L. N. C.; Venkitachalam, T. V. *Chem. Phys. Lett.* **1978**, *55*, 116.
- (25) Krishnamachari, S. L. N. G.; Ramsay, D. A. *Faraday Discuss. Chem. Soc.* **1981**, *71*, 205.
- (26) Coquart, B. *Can. J. Phys.* **1985**, *63*, 1362.
- (27) Tang, J.; Saito, S. *J. Chem. Phys.* **1996**, *105*, 8020.
- (28) McCarthy, M. C.; Vrtilik, J. M.; Gottlieb, E. W.; Tao, F.-M.; Gottlieb, C. A.; Thaddeus, P. *Astrophys. J.* **1994**, *431*, L127.
- (29) He, S.-G.; Clouthier, D. J. *J. Chem. Phys.* **2005**, *123*, 014317.
- (30) Kohguchi, H.; Ohshima, Y.; Endo, Y. *Chem. Phys. Lett.* **1996**, *254*, 397.
- (31) He, S.-G.; Clouthier, D. J. *J. Chem. Phys.* **2004**, *120*, 8544.
- (32) Perić, M.; Stevanović, L.; Jerosimić, S. *J. Chem. Phys.* **2002**, *117*, 4233.
- (33) Perić, M.; Marian, C. M.; Peyerimhoff, S. D. *J. Chem. Phys.* **2001**, *114*, 6086.
- (34) He, S.-G.; Clouthier, D. J. *J. Chem. Phys.* **2005**, *123*, 014317.
- (35) He, S.-G.; Clouthier, D. J. *J. Chem. Phys.* **2005**, *123*, 014316.
- (36) Motylewski, T.; Linnartz, H. *Rev. Sci. Instrum.* **1999**, *70*, 1305.
- (37) Prior, Y. *Appl. Opt.* **1980**, *19*, 1741.
- (38) PGOPHER, a Program for Simulating Rotational Structure. Western, C.M., University of Bristol <http://pgopher.chm.bris.ac.uk>.
- (39) Bultitude, K.; Bratfalean, R.; Ewart, P. *J. Raman Spectrosc.* **2003**, *34*, 1030.

JP909738N

Chapter 5

Laser Ablation

5.1 Introduction

Clusters (micro-aggregates of atoms and molecules) possess unique properties. Cluster science can be distinguished from molecular physics and condensed matter physics. A point that is usually raised in cluster research is that the clusters bridge the gap between isolated gas phase molecules and condensed matter [1]. As an example, Figure 5.1 illustrates the types of structural isomers which exist for clusters containing between 20 and 32 atoms. The first synthesis of C_{60} and C_{70} [2] enabled the study of their structure using var-

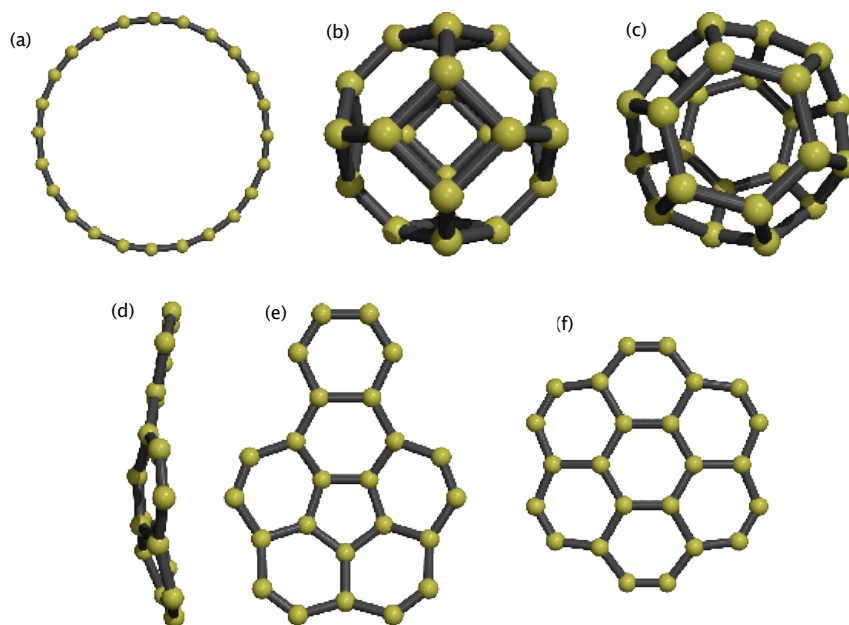


Figure 5.1: Structural isomers of (a) ring, (b) symmetry cage, (c) symmetry fullerene, (d,e) (side, front) one-pentagon bowl, (f) graphitic sheet.

ious techniques including nuclear magnetic resonance (NMR), X-ray diffraction and IR spectroscopy. The fullerene structures of these two species are now well established. Carbon clusters demonstrate some special features which set them apart from other clusters. These clusters, fullerenes and especially C_{60} , have been a testing ground for statistical theories. New experimental results concerning carbon clusters have led to the evolution of new theoretical approaches for structure calculations and the dynamics of evaporation and cooling[?]. Smaller carbon clusters have not been isolated and the structures of the corresponding ionic clusters have been indirectly determined. The spectroscopy, structure, and energetics of small carbon clusters has been reviewed recently [3, 4] (Figure 5.2). The observation of C_2 molecules is important in several research fields including astrophysics [9], monitoring of combustion processes [10, 11, 12], industry plasmas [13], for the growth of carbon nanotubes [14, 15], small carbon clusters and thin film deposition [16]. C_2 is by far the most well-characterized of all the carbon clusters [17]. The spectra of neutral pure carbon chains are of special astrophysical interest because electronic transitions of C_2 and C_3 have been observed in diffuse and translucent interstellar clouds[18]. In the

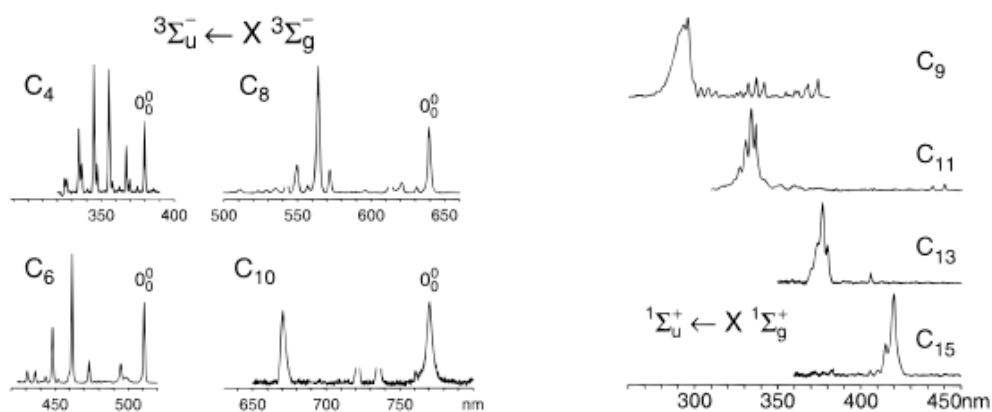


Figure 5.2: Electronic transition of the even- and odd-number carbon chains in neon matrixes [4, 5, 6, 7, 8].

infrared region, C_3 and C_5 have been detected in circumstellar shells of carbon-rich stars [19] (Figure 5.3) and rotationally resolved vibrational transitions of chains up to C_{13} have been measured in the laboratory [20, 21, 3]. In the last twenty years, a variety of fullerene carbon clusters including ball-tube-, onion- and snail-like clusters have been discovered in arc discharge [2], laser ablation [22], and hydrocarbon combustion [23]. Strong thermal evaporation of the target in laser ablation is known to produce overcooled vapour [24]. Adiabatic expansion of the vapour further increases the oversaturation degree and creates favourable conditions for cluster formation. Mass-spectroscopic studies for near-threshold nanosecond ablation in vacuum at 248 nm revealed no cluster formation in case of metallic target [25] and only two- and three-atomic molecules with traces of four- and five-atomic molecules in case of graphite target [26]. Nanosecond laser ablation of graphite in vacuum at 1064 nm gave larger carbon clusters (up to $\sim C_{22}$) at higher laser intensities [27]. Carbon clusters were not observed at 193 nm [28]. At this wavelength, the photon energy (~ 6.4 eV) exceeds the energy of CC bonds (~ 6.3 eV) and intensive photodissociation is expected. Cluster formation in nanosecond laser ablation has been theoretically studied using the droplet model of homogeneous nucleation [29]. By laser ablation of a metal target (Zn, Mg or Gd) near the stream of a supersonic expansion,

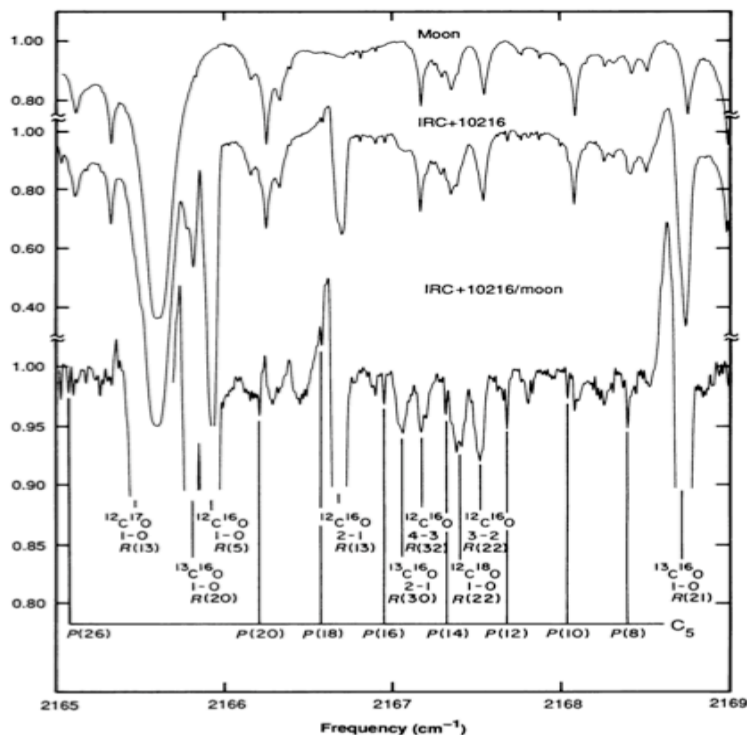


Figure 5.3: A short section of the spectrum of the moon, IRC+ 10216, and the ratio IRC+ 10216/moon showing most of the observed C_5 P branch. Also identified are CO lines of various isotopic species. The CO lines are formed throughout the circumstellar shell and have a different line shape and excitation temperature from the C_5 . The frequency scale has not been corrected for the earth's velocity. Note that the intensity scale for the ratioed spectrum has been expanded by a factor of 4 [19].

molecular oxygen cluster anions $(O_2)_n^-$ also have been efficiently produced with n in the range of 1-20 or more [30].

The plasma can be probed and its constituents can be studied by various *in situ* techniques. Measurement of the density, e.g., of C_2 radical by means of cavity ring-down spectroscopy (CRDS) [31] has been reported recently in different environments, such as, an oxyacetylene flame [32], a microwave methane / hydrogen plasma [33, 34], a thermal plasma [35], and a d.c.-arc jet CVD reactors [36]. In these cases the radical density does not change during the ringdown time. Larger carbon clusters have also been detected and analyzed by CRDS, e.g, C_3 [37], C_4 [38], C_5 [39] and C_9 [40]. The application of pulsed CRDS for the detection of carbon molecules which are present in the laser-induced plume has been reported in the presented work. The ablation source has been built with some

improvements over the previous one reported in [39], which is, therefore, expected to produce better results. C_2 , C_3 and C_5 have been detected. This has been done with the aim of obtaining high resolution spectra of the clusters in the gas phase with narrow bandwidth lasers.

5.2 Experimental set up

5.2.1 Ablation source

A target rod of 8 mm diameter and 5 cm length, rests in a hollow unit with a slit (1 mm x 12 mm) drawn on one end and a 2 mm orifice on the far end (refer to Figure 5.4). The pulsed valve, which controls the flow of gas, is connected to the unit through the orifice. The whole block is mounted on an X-Y translation stage. The rod is rotated and translated to expose a fresh surface to the ablation laser using a dc bevel gears set motor. The feedback loop of the motor driver circuit is broken to modify the servo. This modification involves introducing a magnet and its sensor. The magnet is placed on the end of a plastic tube attached to the rotating motor shaft. The sensor on a small home-made control board is positioned near the plastic tube which connects to the motor driver circuit. This magnet set comes closer after a certain time as the shaft moves. At this instant, it stops and triggers a change in direction of motion resulting in the motor to turn in the opposite sense. The rod thus translates back and forth over a distance of 15 mm. Figure 5.4 illustrates some of the important aspects of the source. Target rods of different materials like graphite, aluminium or copper can be used to produce the clusters of corresponding atoms / molecules. The second / third harmonic of a pulsed Nd:YAG laser (4 ns pulse, repetition rate 10 Hz from Quantel's Brilliant model) is used. Pulse energies of 40 mJ to 100 mJ have been used for ablation. The laser beam is focused to a point (~ 0.7 mm size) by a spherical lens or along a line (0.5 mm x 5.0 mm) through a cylindrical lens on the target surface at an incident angle of 30° . The carrier gas is expanded into a chamber through the slit with the flow controlled by the pulsed valve. The vacuum chamber is evacuated by means of a roots blower system to about 10^{-3} mbar. Normally, argon (Ar)

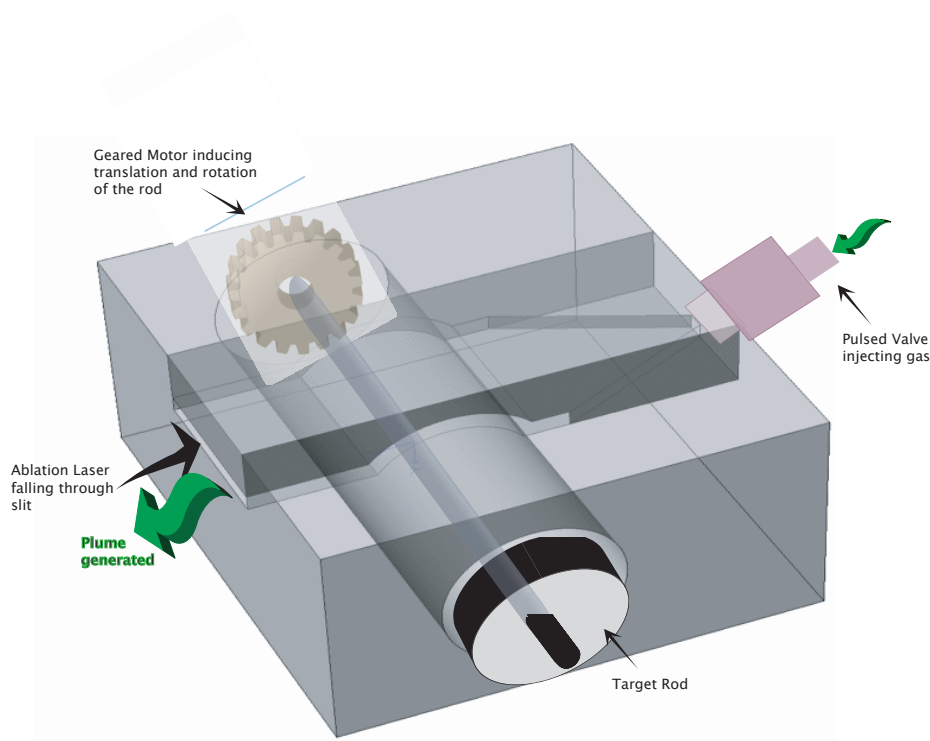


Figure 5.4: *The ablation source.*

or helium (He) has been used as the carrier gas.

5.2.2 Probe

The probe beam is generated by a dye laser pumped by the third harmonic of Nd:YAG laser operating at 20 Hz with 7 ns long pulses (Spotlight from Innolas). The pulse energy used is less than 1 mJ per pulse at a spectral linewidth of 0.10 cm^{-1} . Calibration is done by a wavemeter (HighFinesse WS7). The beam is spatially filtered in order to obtain a homogeneous Gaussian profile. A standard CRDS setup for pulsed radiation is used as described in [41]. The cavity is formed by two highly reflective plano-concave mirrors each with 1-meter radius of curvature (99.98% reflectivity) separated by a distance of 52 cm. Figure 5.5 shows the schematic of the assembly. A fraction of radiation couples into the cavity. The part leaking out from the rear mirror is collected by a photodiode with amplifier. A broadband filter has been placed in front of the detector to reject the emission

from the discharge. The ringdown curves are fitted by a home-made high-speed program, described in detail in [42]. As CRDS is not a zero-background technique, the discharge is turned off at every alternate laser pulse to make the background correction possible. The typical cavity ring down time obtained is about $20 \mu\text{s}$. The delay between the ablation pulse at the target and the arrival of the probe beam in the plasma can be varied over $\sim 1000 \mu\text{s}$. The ablation pulse and the ringdown signal can be monitored by an oscilloscope to have more control over the delays.

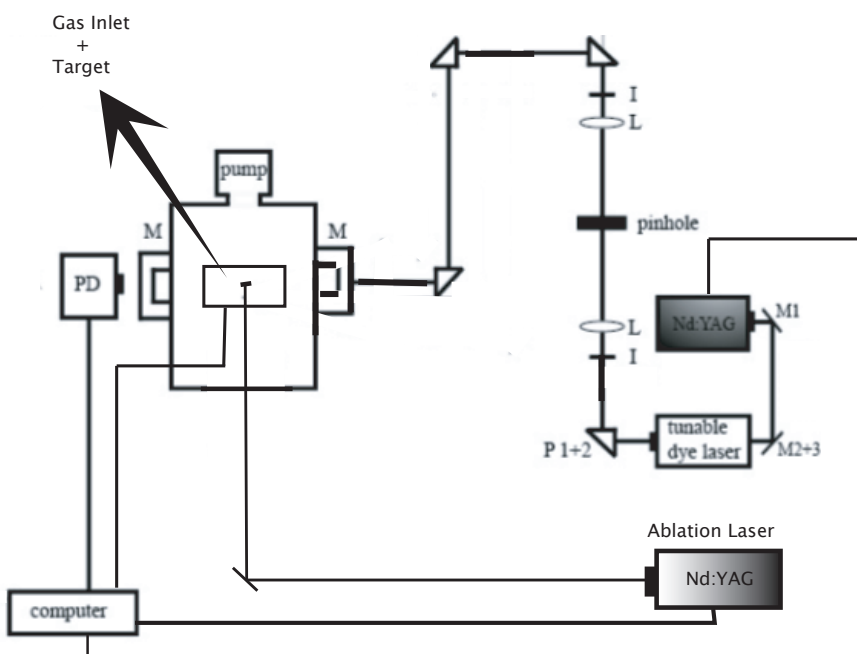


Figure 5.5: Schematic of the experimental setup. *L*: lens; *I*: iris; *M*: mirrors; *P*: prism; *PD*: photodiode.

5.3 Results and discussion

Molecules are produced by the laser ablation of a graphite target and recorded using CRDS. The plasma is probed at a distance of 5 mm above the slit. The pulse energy required to ablate is found to depend on the radical under investigation. The beam after the focus on the target, produces laser fluence of ~ 3.0 to 20.0 Jcm^{-2} with the cylindrical

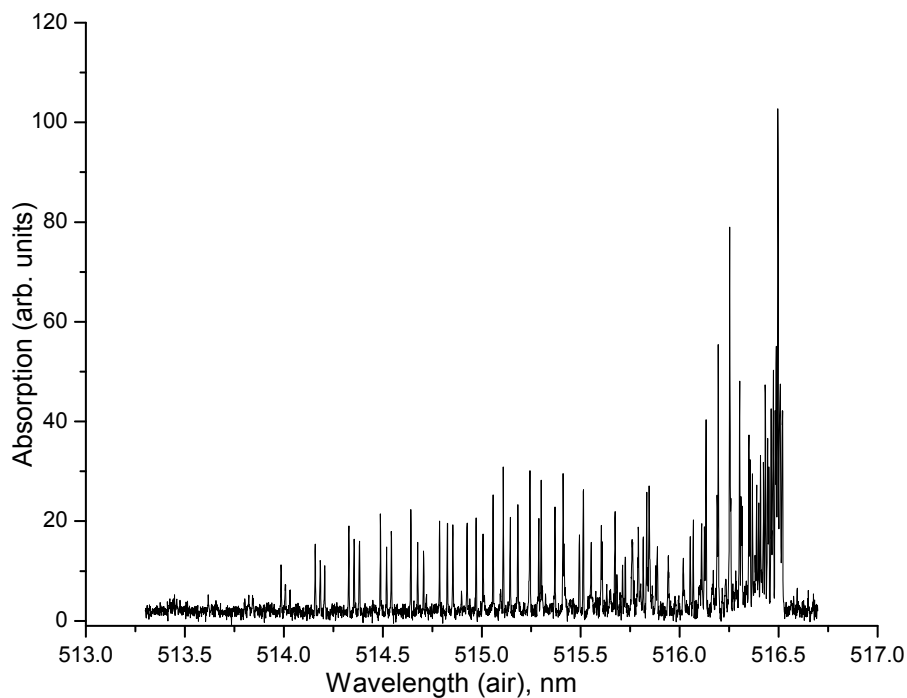


Figure 5.6: The absorption spectrum of the $(0,0) d^3\Pi_g \leftarrow a^3\Pi_u$ Swan band system of C_2 . This is obtained with ablation laser fluence of $\sim 10 \text{ Jcm}^{-2}$ at the wavelength of 532 nm.

and spherical lens, respectively. A wavelength independent loss of about 10^{-6} cm^{-1} is observed. A density of about $4 \times 10^{10} \text{ cm}^{-3}$ and rotational temperatures of about 300 K are obtained. Probe beam of 0.15 cm^{-1} bandwidth has been used in this project.

The absorption spectrum of C_2 is measured in the region of 515 nm. Almost the entire $(0,0) d^3\Pi_g \leftarrow a^3\Pi_u$ Swan band of C_2 is observed. Figure 5.6 shows the spectrum obtained. The C_3 molecule is produced. Figure 5.7 shows a part of C_3 transition (Comet Head System) of ground electronic state $X^1\Sigma_g^+$ to first excited state $A^1\Pi_u$ around 405.3 nm. C_5 clusters also have been produced and measured. The Figure 5.8 shows the origin band of the electronic $^1\Pi_u \leftarrow X^1\Sigma_g^+$ transition of C_5 in the gas phase. The delays between gas pulse, ablation laser and probe beam are critical and have to be carefully adjusted to produce a particular cluster in large concentration. This is sometimes difficult to achieve. A specific observation can be helpful in this direction. A typical discontinuity in the ring

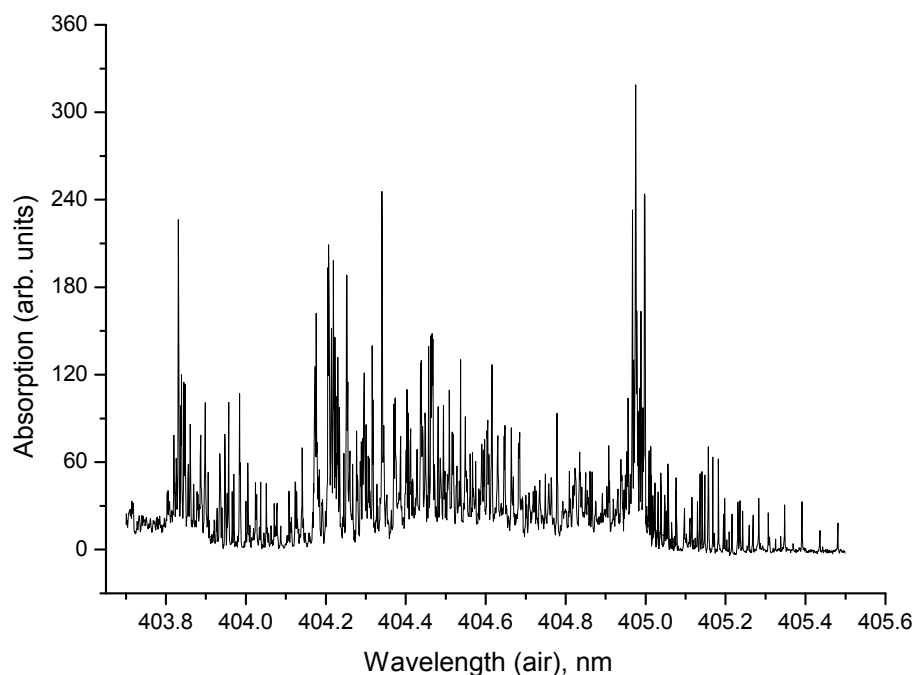


Figure 5.7: The absorption spectrum of the $A^1\Pi_u \leftarrow X^1\Sigma_g^+$ transition of C_3 . The ablation wavelength: 532 nm; Ablation laser fluence: 11 Jcm^{-2} .

down time occurs at an absorption event. This can be considered as an indication of approaching the right delays which makes the adjustment process easier. The presented ablation source is convenient to use because the photon source is outside the vacuum chamber. Furthermore, the laser ablation is localized both in time (approximately 10 ns) and in space, and therefore excessive heating of the source is avoided. The rotational temperature of the clusters remains $\sim 300 \text{ K}$ for several microseconds after the ablation pulse. CRDS with laser ablation provides a platform to study the clusters of varying size which are produced by laser ablation of a target. It adds the advantages of CRDS to the technique presented.

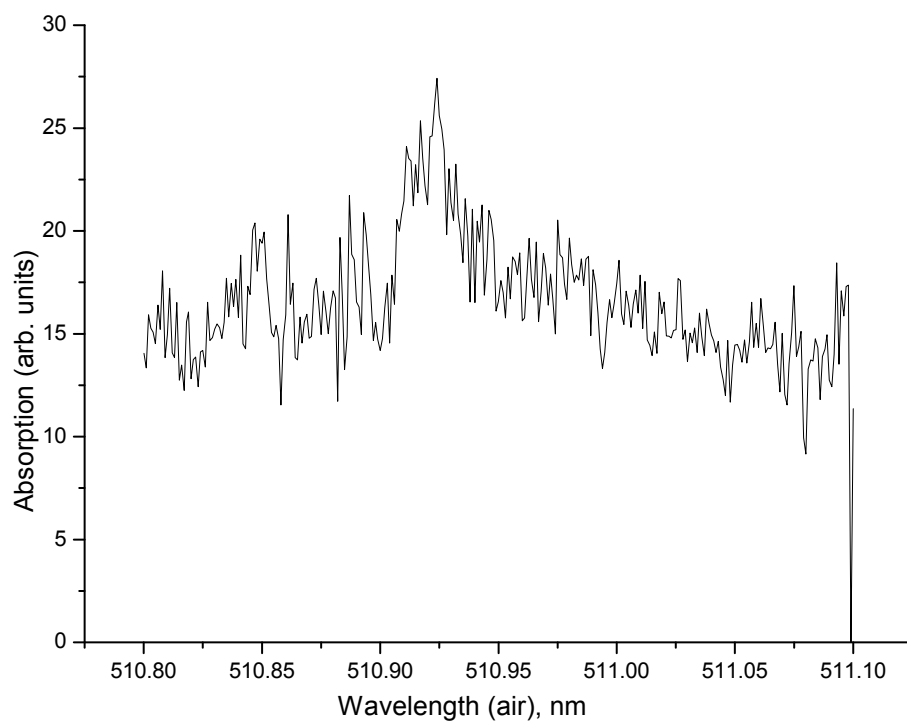


Figure 5.8: The origin band of the ${}^1\Pi_u \leftarrow X^1\Sigma_g^+$ electronic transition of C_5 . The ablation wavelength: 355 nm; Ablation laser fluence: 16 Jcm^{-2} .

Bibliography

- [1] C. Lifshitz, *Int. J. Mass Spectrom.*, 2000, **200**, 423.
- [2] W. Kraetschmer, L. Lamb, K. Fostiropoulos, and D. Huffman, *Nature*, 1990, **347**, 354.
- [3] A. van Orden and R. J. Saykally, *Chem. Rev.*, 1998, **98**, 2313.
- [4] J. Maier, *J. Phys. Chem. A*, 1998, **102**, 3462.
- [5] P. Freivogel, J. Fulara, M. Jakobi, D. D Forney, and J. P. Maier, *J. Chem. Phys.*, 1995, **103**, 54.
- [6] P. Freivogel, M. Grutter, D. Forney, and J. P. Maier, *J. Chem. Phys.*, 1997, **107**, 4468.
- [7] P. Freivogel, M. Grutter, D. Forney, and J. P. Maier, *Chem. Phys. Lett.*, 1996, **249**, 191.
- [8] D. Forney, P. Freivogel, M. Grutter, and J. P. Maier, *J. Chem. Phys.*, 1996, **104**, 4954.
- [9] A. Tanabashi and T. Amano, *J. Mol. Spectrosc.*, 2002, **215**, 285.
- [10] U. Westblom, P.-E. Bengtsson, and M. Alden, *Appl. Phys. B*, 1991, **52**, 371.
- [11] R. Bleekrode and W. C. Nieuwpoort, *J. Chem. Phys.*, 1965, **43**, 3680.
- [12] M. G. Allen, R. D. Howe, and R. K. Hanson, *Opt. Lett.*, 1986, **11**, 126.
- [13] P. Caubet and G. Dorthé, *Chem. Phys. Lett*, 1994, **218**, 529.
- [14] S. Arepalli, P. Nikolaev, W. Holmes, and C. D. Scott, *Appl. Phys. A*, 2000, **70**, 125.
- [15] S. Lebedkin, P. Schweiss, B. Renker, S. Malik, F. Hennrich, M. Neumaier, C. Stoermer, and M. M. Kappes, *Carbon*, 2002, **40**, 417.
- [16] T. Yoshitake, T. Hara, and K. Nagayama, *Diamond Relat. Mater.*, 2003, **12**, 306.
- [17] A. van Orden and R. J. Saykally, *Chem. Rev.*, 1998, **98**, 2313.
- [18] L. M. Haffner and D. M. Meyer, *Astrophys. J*, 1995, **453**, 450.

- [19] P. F. Bernath, K. H. Hinkle, and J. J. Keady, *Science*, 1989, **244**, 562.
- [20] J. R. Heath, A. L. Cooksy, M. H. W. Gruebele, C. A. Schmuttenmaer, and R. J. Saykally, *Science*, 1989, **244**, 564.
- [21] T. F. Giesen, A. van Orden, H. J. Hwang, R. S. Fellers, R. A. Provencal, and R. Saykally, *Science*, 1994, **265**, 756.
- [22] E. A. Rohlfing, D. M. Cox, and A. Kaldor, *J. Chem. Phys.*, 1984, **81**, 3322.
- [23] B. Bunsenges, *Phys. Chem.*, 1992, **96**, 841.
- [24] S. Anisimov, *Sov. Phys. JETP*, 1968, **27**, 182.
- [25] T. Bennett, C. Grigoropoulos, and D. Krajnovich, *J. Appl. Phys.*, 1995, **77**, 849.
- [26] D. Krajnovich, *J. Chem. Phys.*, 1995, **102**, 726.
- [27] T. Wakabayashi, T. Momose, and T. Shida, *J. Chem. Phys.*, 1999, **111**, 6260.
- [28] F. Claeysens, R. Lade, K. Rosser, and M. Ashfold, *J. Appl. Phys.*, 2001, **89**, 697.
- [29] T. Ohkubo, M. Kuwata, B. Luk'yanchuk, and T. Yabe, *Appl. Phys. A*, 2003, **77**, 271.
- [30] W. Lu, R. Huang, and S. Yang, *J. Photochem. and Photobiol. A*, 1995, **92**, 13.
- [31] G. Berden, R. Peeters, and G. Meijer, *Int. Rev. Phys. Chem*, 2000, **19**, 565.
- [32] A. Staicu, R. L. Stolk, and J. J. ter Meulen, *J. Appl. Phys.*, 2002, **91**, 969.
- [33] P. John, J. R. Rabeau, and J. I. B. Wilson, *Diamond Relat. Mater.*, 2002, **11**, 608.
- [34] M. Hiramatsu, K. Kato, C. H. Lau, J. S. Foord, and M. Hori, *Diamond Relat. Mater.*, 2003, **12**, 365.
- [35] J. Benedikt, R. V. Woen, S. L. M. van Mensfoort, V. Perina, J. Hong, and M. C. M. van de Sanden, *Diamond Relat. Mater.*, 2003, **12**, 90.
- [36] Y. A. Mankelevich, N. V. Suetin, M. N. R. Ashfold, W. E. Boxford, A. J. Orr-Ewing, J. A. Smith, and J. B. Wills, *Diamond Relat. Mater.*, 2003, **12**, 383.
- [37] B. J. McCall, R. N. Casaes, M. Adamkovics, and R. J. Saykally, *Chem. Phys. Lett.*, 2003, **374**, 583.
- [38] H. Linnartz, O. Vaizert, T. Motylewski, and J. P. Maier, *J. Chem. Phys.*, 2000, **112**, 9777.
- [39] T. Motylewski, O. Vaizert, T. F. Giesen, H. Linnartz, and J. P. Maier, *J. Chem. Phys.*, 1999, **111**, 6161.
- [40] R. Casaes, R. Provencal, J. Paul, and R. J. Saykally, *J. Chem. Phys.*, 2002, **116**, 6640.
- [41] T. Motylewski and H. Linnartz, *Rev. Sci. Instrum.*, 1999, **70**, 1305.
- [42] T. Motylewski *Cavity ring down spectroscopy of transient species* PhD thesis, University of Basel, 2001.

6.1 Electronic spectrum of the hydrocarbon cation $CCCCH_3^+$

6.1.1 Parallel and perpendicular structures in electronic transition of polyatomic molecules

In general for any molecule, there are three moments of inertia *viz.* I_A , I_B and I_C about three mutually orthogonal axes A, B, and C (internal molecular axes) with the origin at the center of mass of the system. The moment of inertia about an axis is defined as

$$I = \sum m_i r_i^2 \quad (6.1)$$

where r_i is the distance from the atom to the axis. The three moments of inertia determine the layout of the rotational levels of the molecule. These provide information on molecular geometry structure as well. The axes are labeled so that $I_A \leq I_B \leq I_C$. It is conventional to classify molecules into the following categories (based on the symmetry of their structure),

1. Linear molecules (or linear rotors) : I_A which is the moment of inertia for a rotation taking place along the axis of the molecule is negligible (Figure 6.1), i.e., $I_A \ll I_B = I_C$. For most of the purposes, I_A is taken to be zero. e.g. HCN, CO_2 .
2. Symmetric tops (or symmetric rotors) : A symmetric top is a molecule in which two moments of inertia are the same (Figure 6.2). As a matter of historical convenience, spectroscopists divide such molecules into two classes of symmetric tops: Oblate

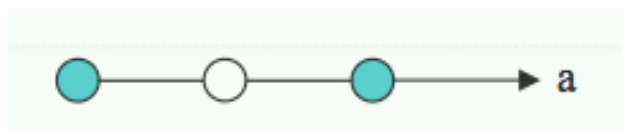


Figure 6.1: *Linear molecule.*

symmetric tops (saucer or disc shaped) with $I_A = I_B < I_C$. e.g. Benzene (C_6H_6), BF_3
 Prolate symmetric tops (rugby football, or cigar shaped) with $I_A < I_B = I_C$. The spectra look rather different and are instantly recognizable. e.g. CH_3I , CH_3Cl . If a

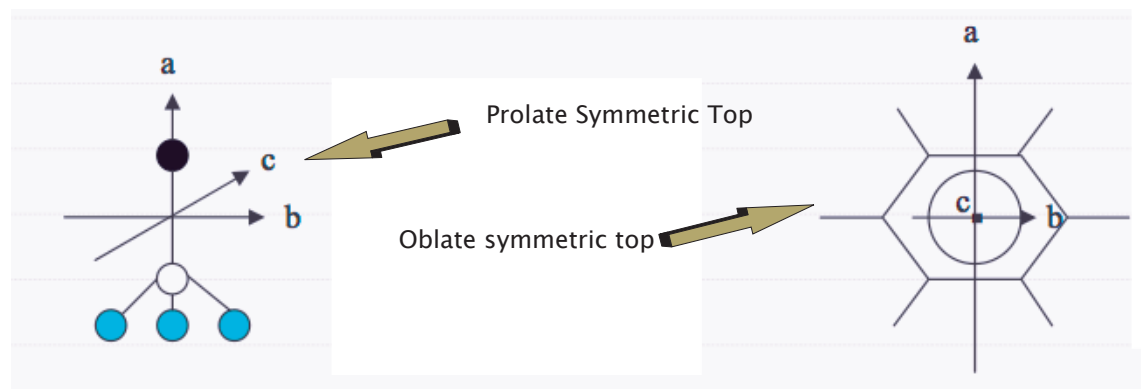


Figure 6.2: *Symmetric top molecule.*

molecule has a symmetry axis of three- or more fold symmetry, it is always a symmetric top (Figure 6.3). Molecules of lower symmetry can be near-symmetric tops, having two rotational constants of close values and with a lack of spectral resolution they can behave like symmetric tops.

3. Spherical tops (or spherical rotors) : can be considered as a special case of symmetric tops with equal moment of inertia about all three axes ($I_A = I_B = I_C$). e.g. SF_6 , CH_4 .
4. Asymmetric tops : it has all three moments of inertia different (Figure 6.4). $I_A \lesssim I_B \lesssim I_C$

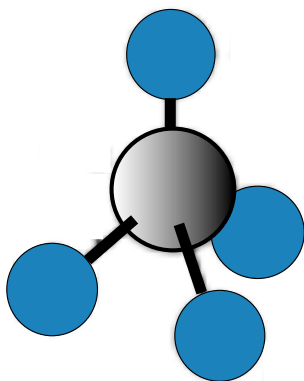


Figure 6.3: Spherical top molecule.

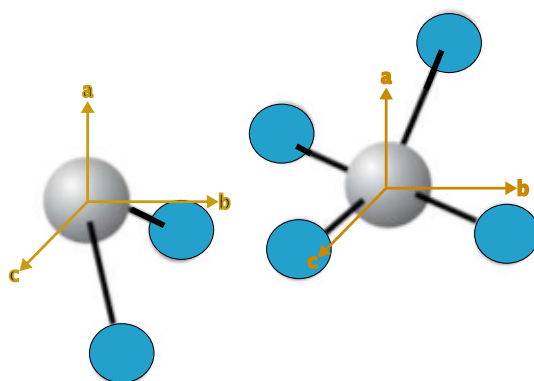


Figure 6.4: Asymmetric top molecule.

6.1.2 General features of molecular rotation

- Linear molecules

These molecules have two degenerate modes of rotation ($I_B = I_C$, $I_A = 0$). Since we cannot distinguish between the two modes, we need only one rotational quantum number (J) to describe the rotational motion of the molecule. The rotational energy levels, $F(J)$, of the molecule based on rigid rotor model can be expressed as,

$$F(J) = B_e J(J + 1) \quad (6.2)$$

where $J = 0, 1, 2, \dots$

and B_e is the rotational constant of the molecule and is related to the moment of inertia of the molecule $I_B = I_C$ by $B_e = \frac{h}{8\pi^2 c I_B}$

A real molecule is not a rigid rotor though because the bond between the atoms can stretch at the same time as the molecule rotates. As rotation increases, the centrifugal force stretches the bond, increasing r and decreasing the effective B value. The bond length also depends, in an average sense, on the vibrational state v .

The selection rules for rovibronic transitions (i.e. transitions that involve electronic excitation of molecule) are $\Delta J = 0, -1, \text{ and } +1$, giving rise to the Q-, P- and R-branches of the rotational structure, respectively.

- Symmetric Top

The rotational motion of a symmetric top molecule can be described by two independent rotational quantum number (since two axes have equal moment of inertia, the rotational motion about these axes requires only one rotational quantum number for complete description). Instead of defining the two rotational quantum number for two independent axes, we associate one of the quantum number (J) with the total angular momentum of the molecule. The other quantum number (K) is associated with the angular momentum of the axis which has different moment of inertia (i.e. axis C for oblate symmetric top and axis A for prolate symmetric tops). The rotational energy $F(J, K)$ of such a molecule, based on non-rigid rotors model with the first order centrifugal distortion correction can be expressed in terms of the two previously defined rotational quantum number as follows.

For a near prolate symmetric top molecule ($A > B \approx C$)

$$F(J, k) = BJ(J+1) + [A - (B+C)/2]k^2 - D_k k^4 - D_{Jk} J(J+1)k^2 - D_J J^2(J+1)^2 \quad (6.3)$$

where, $k = -K, K$ ($K > 0$) and $J = K, K+1, K+2, \text{ etc.}$

with $B = \frac{h}{8\pi^2 c I_B}$ and $A = \frac{h}{8\pi^2 c I_A}$.

For a near oblate molecule ($C < A \approx B$),

$$F(J, k) = BJ(J+1) + [C - (A+B)/2]k^2 - D_k k^4 - D_{Jk} J(J+1)k^2 - D_J J^2(J+1)^2 \quad (6.4)$$

where, $k = -K, K$ ($K > 0$) and $J = K, K+1, K+2$, etc.

with $A = \frac{h}{8\pi^2 c I_C}$.

The value of k must not be greater J , as it represents the component of J (Figure 6.5). Since the energy does not depend on the sign of k , all states with the exception of $K = 0$ are doubly degenerate, corresponding to opposite directions of rotation around the symmetry axis. The rotational Hamiltonian can be expressed as,

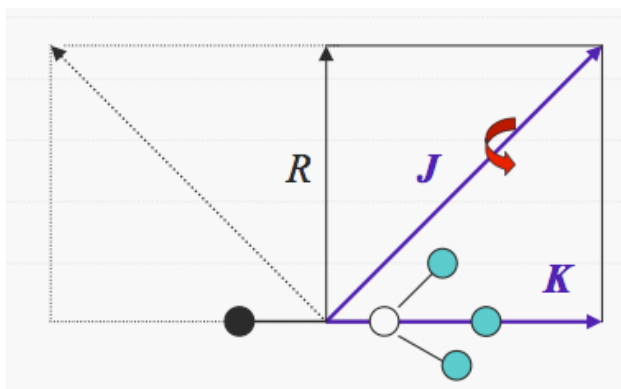


Figure 6.5: Vector diagram for a prolate symmetric top.

$$H_{rot}/h = AJ_a^2 + BJ_b^2 + CJ_c^2 \quad (6.5)$$

A, B, C are the rotational constants of the molecule.

- Asymmetric Top Molecules

Because asymmetric top molecules do not have an axis of symmetry, there is no preferred direction which carries out a simple rotation around the total angular momentum \vec{P} . The approximate energy levels are derived using the symmetric top wave functions as a basis, but derivation of the exact levels is very difficult in the general case, as they cannot be represented by an explicit formula analogous to that

for the symmetric top [?, ?, ?, ?]. Furthermore, the interactions which were neglected in deriving the levels for the symmetric top are more significant for the asymmetric top [?, ?, ?].

Although the quantum number k has no meaning for the asymmetric top, there are still $2J+1$ energy levels for each value of J . Each of these are specified by the quantum numbers K_a and K_c . The degenerate levels of the symmetric rotor ($+K$ and $-K$) are separated in the asymmetric case; each level of the asymmetric top has a different energy. For slight deviations from the symmetric top the splitting of the levels is slight, the quantum number k is approximately defined and the energy levels may be obtained by perturbation methods. In the more general case, however, there is no quantum number with any physical meaning to distinguish between the $2J+1$ levels of same J . The sublevels are labelled simply as J_τ ($\tau = -J, -J+1, -J+2, \dots +J$) in order of increasing energy, the lowest level being J_{-J} , the next J_{-J+1} , and so on up to J_J .

An expression for the energy levels has been derived by King, Hainer, and Cross [?], given as,

$$F(J, \kappa) = \frac{1}{2}(A + C)J(J + 1) + \frac{1}{2}(A - C)E_\tau \quad (6.6)$$

where A , B , and C are the rotational constants defined above. E_τ is a numeric, called the reduced energy, which is a function of J and of an asymmetry parameter κ , defined by Ray [?]. κ is given by,

$$\kappa = \frac{2B - A - C}{A - C}$$

For a prolate top, $\kappa = -1$, and for an oblate top, $\kappa = +1$

6.1.3 Rotational energy levels

Symmetric top Figure 6.6 shows the energy level diagram of symmetric top molecules. Every k ladder has the rotational levels structure same as linear molecule but offset by $(A - B)k^2$ in energy. For a prolate top A is greater than $B(= C)$ which implies the energy

increases for increasing $|k|$. For an oblate top $B(= A)$ is greater than C , so that the energy of levels with the same J decreases for increasing $|k|$.

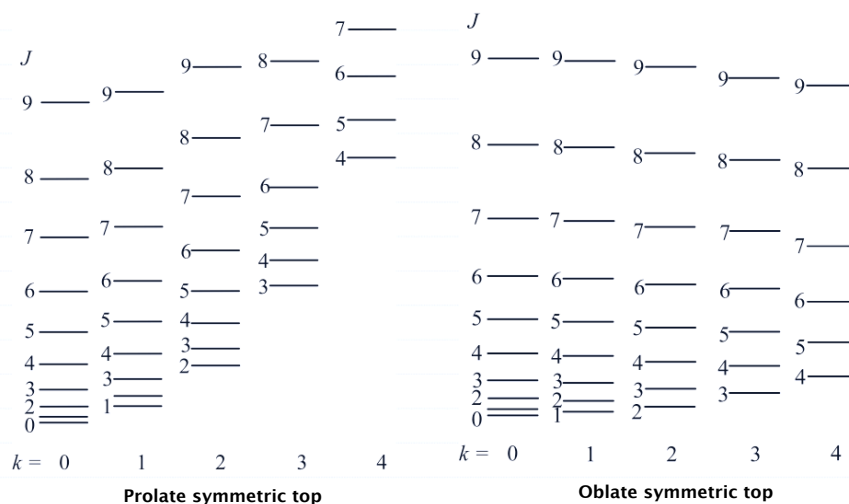


Figure 6.6: Rotational energy levels of a symmetric top.

Asymmetric top The behavior of the asymmetric top energy levels is shown in Figure 6.7. These levels lie between those of the two symmetric tops, their position depending on the relationship of the intermediate moment of inertia I_B to I_A and I_C . Specifically, a given asymmetric top level connects a K level (designated K_{-1}) of the limiting prolate top ($I_B = I_C$) with a K level (designated K_1) of the limiting oblate top ($I_B = I_A$). This leads to an alternate designation for each J_τ level as $J_{K_{-1}K_I}$ and for each reduced energy E_τ as $E_{K_{-1}K_I}$. $J_{K_a K_c}$ is also equally used in place of $J_{K_{-1}K_I}$; this is termed as King-Hainer-Cross notation. The levels for the same J and for different $E_{K_{-1}K_I}$ do not cross each other.

The electronic transitions Electronic transitions have associated vibrational and rotational structure (Figure 6.8). A particular rovibronic transition occurs at a line position ν with

$$\nu = T_e + G'(v') + F'(J') - G''(v'') - F''(J'') \quad (6.7)$$

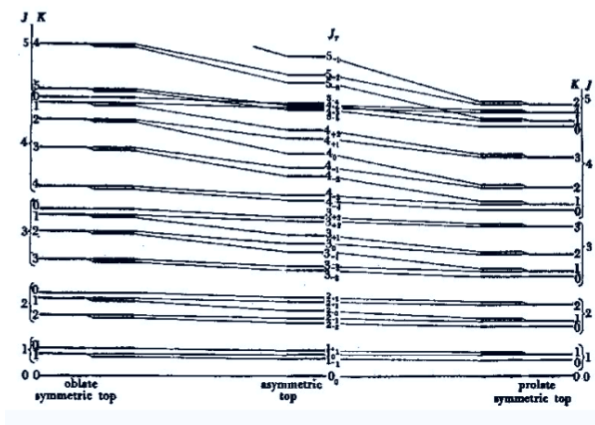


Figure 6.7: Rotational energy levels of an asymmetric top

where $G(v)$ and $F(J)$ are the vibrational and rotational energy level expressions, and T_e is the equilibrium transition energy between the states. The possibility of geometry changes

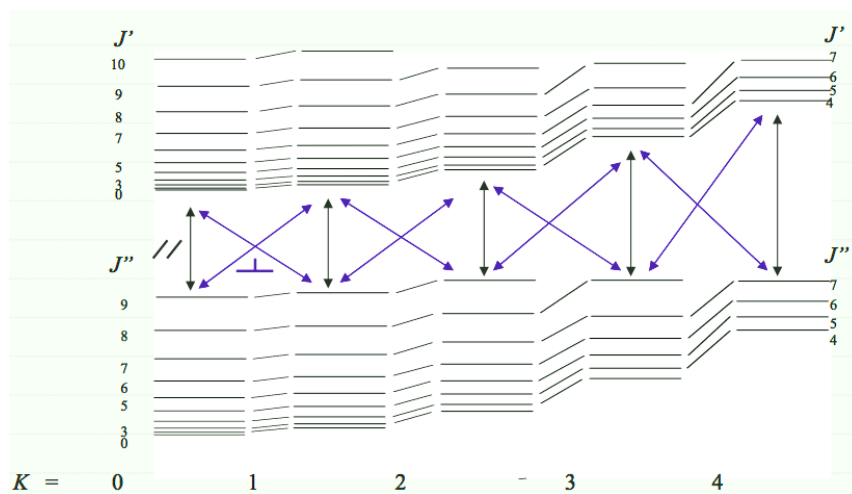


Figure 6.8: Rotational energy levels associated with an electronic transition

coupled with the large number of special effects such as vibronic coupling, Jahn-Teller effect and Renner-Teller effect, to say nothing of fine structure and hyperfine structure, make electronic spectroscopy of polyatomics a fascinating and challenging area of study [?].

6.1.4 Transition types

The spectra of linear and symmetric tops can generally be classified as parallel and perpendicular depending upon the direction of the electronic transition dipole moments.

Parallel transitions occur when a transition moment is aligned along the symmetry axis of the molecule within a given K ladder. The selection rules are,

$$\Delta K = 0 \text{ and } \Delta J = \pm 1 \text{ for } K = 0,$$

$$\Delta K = 0 \text{ and } \Delta J = 0, \pm 1 \text{ for } K \neq 0.$$

If a transition dipole moment is perpendicular to the symmetry axis, its interaction with the electromagnetic field provides torque around this axis, leading to

$$\Delta K = \pm 1 \text{ and } \Delta J = 0, \pm 1. \text{ Perpendicular modes thus always have P, Q and R branches.}$$

Because the parallel symmetric top selection rules (except for $K = 0$) are very similar to those for a perpendicular transition of a linear molecule, the bands will be similar. The bands thus have simple P, Q, R branches although for the symmetric top each rotational line will show K-structure at high resolution. As in the pure rotational case, each rotational line will split into $J+1$ K-components because $K = 0, 1, \dots, J$. The spacing between two adjacent ladders, K and $K + 1$, is $(A - B)(2K + 1)$ that gives rise to a series of rotational progressions spaced by $2(A - B)$, so called K-structure. The scheme of allowed transitions for the prolate top is shown in Figure 6.9. For asymmetric tops the rotational selection

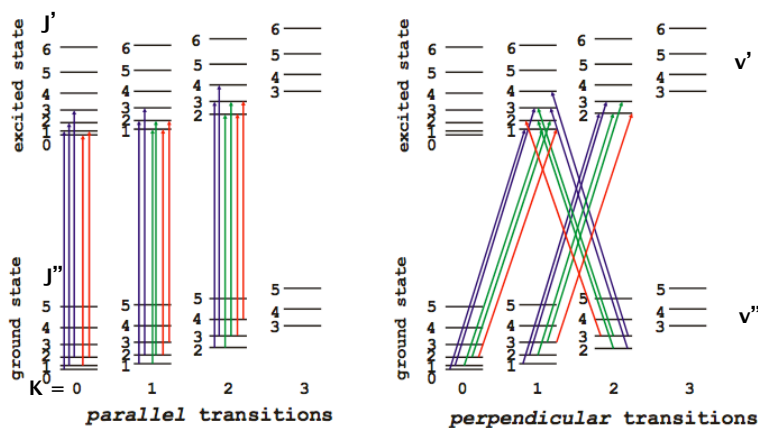


Figure 6.9: Allowed transitions for prolate rotor for the first few sub-bands. R-, Q- and P-branch transitions are marked with different colors.

rules can be classified as a-type, b-type or c-type depending on the components (μ_a, μ_b, μ_c) of the permanent electronic transition dipole moment vector $\vec{\mu}$, along the a, b or c principal molecular axes, respectively.

For an asymmetric rotor the selection rules are:

	<i>a - type</i>		<i>b - type</i>		<i>c - type</i>	
	ΔK_a	ΔK_c	ΔK_a	ΔK_c	ΔK_a	ΔK_c
<i>P</i>	0	-1	-1	-1	-1	0
<i>Q</i>	0	± 1	± 1	± 1	± 1	0
<i>R</i>	0	+1	+1	+1	+1	0

Table 6.1: Selection Rules

More generally,

for a-type transitions when $\mu_a \neq 0$,

$\Delta J = 0, \pm 1$; $\Delta K_a = 0$ ($, \pm 2, \pm 4, \text{etc.}$); $\Delta K_c = \pm 1$ ($, \pm 3, \pm 5, \text{etc.}$);

for b-type transitions when $\mu_b \neq 0$,

$\Delta J = 0, \pm 1$; $\Delta K_a = \pm 1$ ($, \pm 3, \text{etc.}$); $\Delta K_c = \pm 1$ ($, \pm 3, \text{etc.}$);

for c-type transitions when $\mu_c \neq 0$,

$\Delta J = 0, 1$; $\Delta K_a = \pm 1$ ($, \pm 3, \text{etc.}$); $\Delta K_c = 0$ ($, \pm 2, \text{etc.}$);

The transitions in brackets are weaker than the main transitions. In practice, if the molecule is a prolate near-symmetric rotor, only transitions with $\Delta K_a = 0$ or ± 1 have significant intensity. For an oblate near-symmetric rotor, transitions with $\Delta K_c = 0$ or ± 1 are strong.

6.1.5 Sub-bands of parallel bands: prolate top molecule

Symmetric rotors possess a complex energy level structure and the allowed transitions between all these levels produce a rich and complex spectrum. For transitions between nondegenerate vibronic states, we consider the case where the rotational constants A and B in the upper state are nearly the same as those of the lower state. As indicated in the Figure 6.10, such bands consist of a number of subbands corresponding to different K values. Each of these has a P, Q, and R branch. At the bottom the superposition of

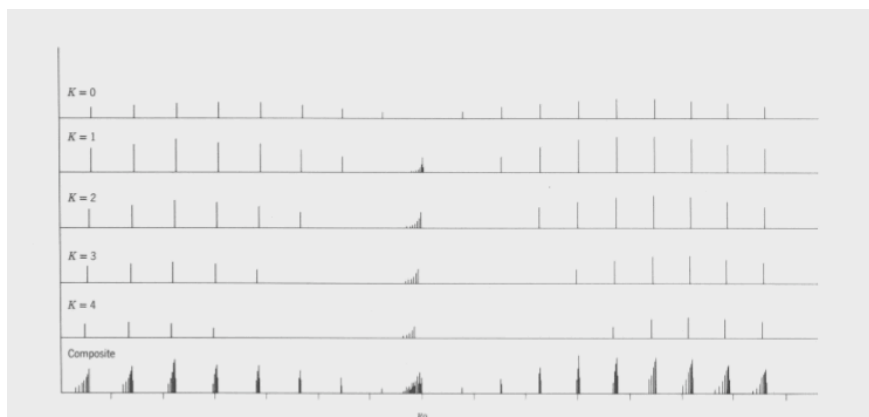


Figure 6.10: Schematic spectrum of parallel band

the subbands is shown as it would appear in the spectrum. Note that in the composite simulated spectrum, many of the lines are so close as to appear blended. This may have important consequences in the choice of appropriate spectral resolution.

For a molecule with a threefold axis of symmetry in accordance with the alternation of statistical weights, there is an intensity alternation of successive subbands: if the nuclear spin is zero, only subbands with K divisible by 3 appear; if it is $\frac{1}{2}$, these subbands are twice as strong as those with K not divisible by 3; and if $I = 1$, the intensity ratio is 11:8. For D_{3h} symmetry there is in addition a strong intensity alternation in the $K = 0$ subband: for $I = 0$ and $I = \frac{1}{2}$ alternate lines are missing, while for $I = 1$ alternate lines have one tenth the intensities of the other lines.

6.1.6 Conclusion

A rotationally resolved spectrum of an electronic transition, provides the A , B , and C rotational constants which help in deriving the structural information about the molecule. This gives insight into the excited state geometry and reveals the symmetry of the excited state by way of the direction of electronic transition moment.

6.2 Pulsed amplification system

1. The AOM introduces a delay of $\sim \mu\text{s}$ between the TTL pulse applied to the AOM driver and the first order diffraction beam output which makes the seed beam. This is due to the limited speed of the acoustic waves generated at the base of the AOM and a finite distance of the input aperture of the AOM. The speed of the acoustic waves is 3630 ms^{-1} . The distance of the input aperture from the source of the wave is 3 cm. The time required for the acoustic waves to overlap with the input fundamental beam is

$$t = \frac{3 \times 10^{-2}}{3630} = 8.2 \mu\text{sec} \quad (6.8)$$

2. Care should be taken that all modes exiting the cavity are detected with equal efficiency, since transverse modes are spatially more extended. If the effective surface of the detector is small, a lens with an appropriate diameter and a short focal length should be used to focus the light onto the detector.
3. There is a disadvantage of the continuum-mode approach. The spatial resolution of CRD spectroscopy is not optimal because of the spatial extent of the transverse modes.

7.1 Personal information

Name: Richa Chauhan

Day of birth: 04.09.1977

Place: Bulandshahr, UP, India

Nationality: Indian

Marital status: Married

7.2 Education

- 1985 - 1995 Primary and secondary central school, Bulandshahr, UP, India.
- 1995 - 1998 Ch. Charan Singh University, Bulandshahr, UP, India.
Bachelor of Science in Physics, Chemistry, Maths.
- 1998 - 2000 Indian Institute of Technology, Roorkee, Uttaranchal, India.
Master of Science in Laser Physics.
- 2000 - 2002 Indian Institute of Technology, Delhi, India.
Master of Technology in Optoelectronics and Optical Communication.
- 2002 - 2003 National Physical Laboratory, Delhi, India.
Project on Liquid Crystals.
- 2004 - 2009 University of Basel, Department of Chemistry, Switzerland.
Ph.D. in the group of Prof. John P. Maier.